Stony Brook University

OFFICIAL COPY

The official electronic file of this thesis or dissertation is maintained by the University Libraries on behalf of The Graduate School at Stony Brook University.

© All Rights Reserved by Author.

Structures, Properties and Biological Applications of Electrospun Polymer Fibers

A Dissertation Presented

by

Ying Liu

to

The Graduate School

in Partial Fulfillment of the Requirements

for the Degree of

Doctor of Philosophy

in

Materials Science and Engineering

Stony Brook University

August 2010

Stony Brook University

The Graduate School

Ying Liu

We, the dissertation committee for the above candidate for the

Doctor of Philosophy degree, hereby recommend

acceptance of this dissertation.

Miriam H. Rafailovich – Dissertation Advisor
Professor, Materials Science and Engineering

Jonathan C. Sokolov - Chairperson of Defense
Professor, Materials Science and Engineering
Stony Brook University

Dilip Gersappe
Associate Professor, Materials Science and Engineering

Richard A. F. Clark
Professor, Biomedical Engineering, Stony Brook University

This dissertation is accepted by the Graduate School

Lawrence Martin
Dean of the Graduate School

Abstract of the Dissertation

Structures, Properties and Biological Applications of Electrospun Polymer Fibers

by

Ying Liu

Doctor of Philosophy

in

Materials Science and Engineering

Stony Brook University

2010

Electrospinning is becoming an increasingly popular method for producing polymer fibers, since it can attain microscale to nanoscale control of fiber dimensions, morphology, and functionality. Hence electropun fiber technology is now prevalent in numerous applications ranging from tissue engineering, active filtration systems, and super strong materials design.

The electrospinning technique has attracted much attention in its biomedical applications in recent years, such as preparation of scaffolds for tissue engineering applications. Here we present a systematic study of the manner in which the cells interact with electrospun scaffolds and the effects of the scaffolds have on basic cell functions, such as morphology, proliferation, and migration. We obtained electrospun polymer fibers of different diameters, ranging from hundreds of nanometers to several micrometers. Furthermore, we aligned the fibers and formed multilayered structures where both the fiber spacing and pore size could be varied. We found that cells preferred to oriented along the fiber axis when the fiber diameter was above 1 micrometer. Cell measurement on the other hand,

indicated that the proliferation on the aligned fibers was more efficient than the flat surface since the oriented cells did not become confluent as quick as on the polymer thin film. The average migration velocity of the cells on the aligned fibrous scaffold, was lower than that on the planar surface, but remained constant in time.

Efficient filtration of ions and very small particles often requires small pores which restrict the liquid flow and consumes large amounts of energy. Here we show that electrospun fibers can be used to create an active filter, with nearly unrestricted flow. We addressed the use of electrospun fibers to encapsulate microbes of industrially relevant genera. Although the electrospinning typically uses harsh organic solvents and extreme conditions that generally are harmful to bacteria, we describe techniques that overcome these limitations. The encapsulated microbes were viable for up to several months, and the exchange of nutrient between the microbes and their environment was not affected by immobilization.

Since polymeric chains have multiple degrees of freedom, confinement alone can impart special properties. For example, in semicrystalline polymers, which constitute the largest group of commercially useful polymers, confinement can change the melting point while at the same time improving the mechanical properties. My last area of research therefore includes the confinement effects brought by electrospinning semicrystalline polymers into very thin fibers, and the impact of viscosity and nano-additives such as clay. In this chapter I will try to explain these effects by introducing a model based on the viscosity properties of the elelctrospinning solutions.

Dedicated To

My

Family

Table of Contents

List of Figures

List of Tables

Acknowledgements

I would like to start by sincerely thanking my advisor, Prof. Miriam H. Rafailovich, for taking me under her wing as a graduate student- not only giving me such incredible opportunities to perform research, but by sharing her knowledge with me throughout my five years in Stony Brook. Without her constant encouragement, advice, demands, and financially support, this work would not be possible.

I wish to express my warm and sincere thanks to Prof. Richard Clark, who gave me the opportunity to work with them in the Department of Biomedical Engineering. The close collaboration and invaluable discussions around my work have been of great value in this study.

I must also extend thanks to my other committee members, Dr. Jonathan Sokolov and Dr. Dilip Gersappe. Thank you for your insightful discussions and suggestions, which greatly speed up the progress of my project.

During this work, I have collaborated with many colleagues for whom I have great regard, and I wish to extend my warmest thanks to all those who have helped me with my work. I am grateful to Dr. Dev Chidambaram, Dr. Elaine DiMasi, and Steve Bennett in Brookhaven National Laboratory; Prof. Daniel Cohn and Ram Malal in The Hebrew University of Jerusalem; Prof. Eyal Zussman in Israel Institute of Technology; Dr. Fubo Lin, Dr. Kaustabh Ghosh, Dr. Shazia Rana and Lauren Macri in the Department of Biomedical Engineering (Stony Brook University). Without your support, I would not have overcome so many barriers.

Thank Dr. Jim Quinn, Ms. Susan Von Horn and Ms. Lourdes Collazo, for their help with my experiment.

Special thanks must be extended to all the Garcia MRSEC members for the informative conversations and general support this entire time: Dr. Yuan Ji, Dr.

Yantian Wang, Dr. Jaseung Koo, Dr. Zhi Pan, Dr. Xiaohua Fang, Dr. Bingquan Li, Dr. Chunhua Li, Dr. Shouren Ge, Dr. Mayu Si, Dr. Yuan Sun, Dr. Seongchann Pack, Dr. Clive Li, Dr. Jun Jiang, Xiaolan Ba, Chungchueh Chang, Divya Bhatnagar, Chien-Hsu Lin, Cheng Pan, Jennifer Segui, Tatsiana Mironava, Sisi Qin, Youyou Zhai, Liudi Zhang, and Kai Yang.

Finally, I would like to express my gratitude and share my happiness with my family for their unflagging love and support though my life.

Chapter 1. Introduction

1.1. Background

Polymer fibers have several special characteristics, such as large surface to volume ratio, high pore density, and flexibility in surface functionalities compared with any other known forms of the material [1]. These outstanding properties make them optimal candidates for many important applications, including filters, membranes, composites and biomimetic materials [2, 3].

A number of processing techniques such as drawing, template synthesis, phase separation, self-assembly, electrospinning, etc. have been used to prepare polymer fibers in recent years [4, 5]. Among them, Electrospinning is a technology that uses electric field to produce nonwoven materials from a polymer solution or a melt [6]. It has gained popularity in the last 10 years due to its simplicity, inexpensive nature of the setup, and ability to produce polymer fibers from micrometer to nanometer dimensions [7]. Further, various fibrous assemblies can be obtained by using a rotating device and auxiliary electrodes to control the electrospinning jet and the deposition [8].

The history of electrospinning can be dated back to 1934, when Anton Formhals patented a device to collect the electric filed-induced polymer threads [9]. Not many people noticed this technique in the following decades. Until 1990's, Dr. Reneker and other contemporary researchers investigated the process and its potential in nanotechnology [10]. From then on, electrospinning began to attract people's attention. Numbers of materials have been tried, including synthesis fibers and natural materials. In the electrospinning process, a solution or melt is pumped to a metal syringe where a voltage, normally on the order of 2-20 kV, is applied between the needle and collector causing a jet to emanate from the tip of a needle. The fibers are then drawn onto a grounded collector at the rate determined partly by the applied field.

Due to the many benefits of electrospinning, it has been the purpose of this investigation to successfully fabricate polymer fibers for different applications.

1.2. Outline of Chapters

In chapter 2, we used electrospinning technique to produce fibrous scaffolds of (methyl methacrylate) (PMMA). Using a rotating drum, we aligned the fibers and formed multilayered structures where both the fiber spacing and pore size could be varied. We then plated adult human dermal fibroblasts and studied the effect of fiber diameter and orientation on the cell conformation, proliferation and migration. We found that a critical diameter minimum diameter existed, D_0= 0.97 μm for cell orientation to occur. For D< D_0, no big difference in aspect ratio was observed relative to the control samples on PMMA thin film. Hence we could fabricate substrate patterned with fibers of different diameters where different cell conformations co-existed on the same scaffold. On the other hand, staining for vinculin proteins in the cells indicated that on large diameter fibers and on flat surfaces, the focal adhesion points aligned along the cell perimeter. On the very small diameter surfaces, the focal adhesion points were distributed uniformly along the cell. Cell dynamics studies indicated that the proliferation and migration were also affected by the fiber orientation.

In chapter 3, we have shown that en masse cell migration of fibroblasts on the planar surface results in a radial outward trajectory, and a spatially dependent velocity distribution that decreases exponentially in time towards the single cell value. If the cells are plated on the surface of aligned electropsun fibers above 1 μm in diameter, they become polarized along the fiber, expressing focal adhesion points that follow closely the contours of the fibers. The velocity of the cells on the fibrous scaffold is lower than that on the planar surface, and does not depend on degree of orientation. Cells on fiber smaller than 1 μm migrate more slowly than on the planar surface, since they appear to have a large concentration of focal adhesion points. True three-dimensional migration can be observed when plating the droplet on a scaffold that is comprises of at least three layers. The cells still continue to migrate on the fibers surfaces, as they diffuse into the lower layers of the fibrous scaffold.

In chapter 4, we described the use of PEO_{99}-PPO_{67}-PEO_{99} triblock polymer (PEO: Polyethylene oxide and PPO: Polypropylene oxide) fibers, created via electrospinning, to encapsulate microbes of three industrially relevant genera, namely, *Pseudomonas,*

Zymomonas, and *Escherichia*. The presence of bacteria inside the fibers was confirmed by fluorescence microscopy and scanning electron microscopy. While electrospinning process typically uses harsh organic solvents and extreme conditions that are generally harmful to bacteria, we describe techniques that overcome these limitations. Not only were the encapsulated microbes viable for several months, but also their metabolic activity was not affected by immobilization and thus they could be used in various applications. Furthermore, we have engineered, for the first time, a microbe encapsulated cross-linked fibrous polymeric material that is insoluble. Also, the microbe encapsulated active matrix permits efficient exchange of nutrients and metabolic products between the microorganism and the environment. The present results demonstrate the potential of the electrospinning technique for encapsulation and immobilization of bacteria in the form of a synthetic biofilm, while retaining their metabolic activity. This study has wide ranging implications in the engineering and use of novel bio-hybrid materials or biological thin-film catalysts.

In chapter 5, poly (ethylene-co-vinyl acetate) (PEVA)/clay nanocomposite fibers were fabricated using electrospinning. The fiber diameters were controlled by varying the polymer/chloroform concentration which resulted in fibers with diameters ranging from 1 to 15 μm. The clay concentration was varied from 0.35wt% to 6.6wt%. Scanning electron microscopy (SEM) revealed that the fiber diameter increased with increasing clay concentration, while beading decreased. Transmission electron microscopy (TEM) revealed a disruption of the spherulite structures by clay, which is consistent with heterogeneous nucleation. Shear modulus force microscopy (SMFM) indicated a reduction in melting point (T_m) with decreasing diameter for fibers thinner than 15 μm, which was confirmed by temperature dependent X-ray diffraction (XRD) data. For fibers thinner than 8 μm, the presence of clay further enhanced the reduction of T_m.

Chapter 2. Effects of Fiber Orientation and Diameter on the Behavior of Human Dermal Fibroblasts on Electrospun PMMA Scaffolds

2.1. Introduction

Tissue engineering is a new approach to reconstruct and/or regenerate lost or damaged tissue. In natural tissues, cells are arranged with a three-dimensional (3D) organization that provides an appropriate functional and spatial milieu. Therefore, *in vitro* reconstruction requires cells to be cultured in an environment that can mimic the natural geometry. 3D mesh structures made from collagen or polymer fibers are the most common type of tissue scaffolds currently used. However, in general these types of structures do not exhibit the geometric environment observed *in vivo*.

Scaffolds of specific 3D geometry may have the ability to promote and control, via topographic stimuli, cell differentiation and tissue establishment, thereby increasing the quantity and range of material suitable for grafts [11]. Central to this strategy is achievement of a patterned 3D scaffold to which mammalian cells can preferentially adhere.

The influence of two-dimensional (2D) chemical patterns on cell structure and function has been studied by numerous authors [11-22]. Although it is well known that the behavior and function of cell cultures is influenced by geometric constraints and substrate surface properties, less work has been carried out on the effects of 3D geometry on cell behavior, since it is more difficult to produce patterned 3D constructs.

Electrospinning is one of the most efficient fabrication methods that can be utilized to assemble polymer mats with different fiber diameters, from micrometer down to nanometer. During the electrospinning process, fibers are usually collected as nonwoven mats, in which the fibers are randomly oriented. However, fibers with uniaxially aligned structures can be achieved by using various collectors, such as a rotating drum, parallel electrodes and discs [23], as well as conducting, oriented patterned substrates [24, 25],

which have also been used to generate multi-layered structures. Therefore, it should be possible to apply some of these techniques to engineer constructs that can better mimic the selective extracellular matrix (ECM) geometry. Prior to using these constructs, it is essential to understand how fiber dimensionality and orientation affect cell functions.

Poly (methyl methacrylate) (PMMA) is a rigid polymer biomaterial with good degree of compatibility with human tissue. It has been used for making contact lenses, bone implants and prosthetics, and has been a successful patterned or unpatterned substrate for 2D cell cultures for many years [26-33]. Furthermore, it has been shown that PMMA was easy to be electrospun into fibers of different diameters [34, 35]. In this paper we extended this work and showed that these fibers could be oriented into 3D structures. Using these scaffolds, we studied the effects of fiber diameter and orientation on cell structure, proliferation, integrin expression, elastic modulus and cell migration. We also showed that it was possible to build a 3D construct where cell shape could be controlled in a manner analogous to selective tissue geometry (it should also be noted that PMMA is not biodegradable and hence tends to be used for permanent structures such as reinforcement of hip implants. Since we were intent on studying the effects of the substrate on cell morphology, we first chose to focus on PMMA since the mechanical properties were not affected by the prolonged exposure to water and were stable during the course of the experiments).

2.2. Experimental Section

2.2.1. Fabrication and Characterization of PMMA Thin Films

The control samples consisted of cells cultured on flat PMMA (M_w =120,000 Da, $M_w / M_n = 3$, Sigma-Aldrich Inc.) films. PMMA films, approximately 100 nm thick, were spun cast onto glass coverslips, depending on whether the samples were for cell counting and migration measurements. All other samples were prepared on Si wafers. The coated coverslips or wafers were then used as substrates for the electrospun fibers. The entire assembly was annealed at 130^{o}C for 24 hours in order to adhere the fibers to the substrate, and secondly remove residual organic materials.

2.2.2. Electrospinning PMMA Fibers with Different Diameters

Electrospinning is a complex process, and the morphology of electrospun fibers can be affected by either the intrinsic properties of the solution or the processing parameters [34-36]. In this paper, to obtain PMMA fibers with different diameters, we chose to vary the polymer solution concentration and the solvent. The concentrations used were tabulated in Table 2.1 and the scanning electron microscopy (SEM, LEO1550, LEO, Germany) of fibers obtained were shown in Figure 2.2. The distribution of fiber diameters was obtained using Image Tool (The University of Texas Health Science Center in San Antonio). The results were also summarized in Table 2.1 where we could see that the distribution of fiber diameters within one sample was much narrower than the range of fiber diameters studied. Hence the variability of fiber diameter within an individual sample was not expected to affect our cell morphology.

2.2.3. Fabrication of PMMA Aligned Scaffolds

Highly cross-aligned PMMA fibrous scaffold were obtained by electrospinning the solution of 20% PMMA dissolved in chloroform (Figure 2.1). The drum rotation speed was 6750 r/min and the approximate distance between adjacent fibers could be controlled by the collection time. Then the sample was removed, rotated 90 degrees and the

procedure was repeated for the next layer. In this manner, a layer by layer, 3D construct could be built with roughly controlled spacing and fiber diameters (Figure 2.3a and b). In Figure 2.3c we showed a histogram of the distribution of the fiber spacing with a collection time of 20 minutes on each direction. From the figure we could see that the mean spacing between fibers was approximately between 5-10 μm, or roughly the size of the cells. Rotation by 90 degrees yielded another layer with similar spacing between adjacent fibers. In Figure 2.3d we showed the distribution of diameters of the pores, as measured from the SEM micrographs. From the figure we could see that mean size is approximately, 90 μm^2, which was sufficiently large to allow for easy migration for human dermal fibroblasts (AHDFs), whose diameters were about 10-15 μm. The thickness of the entire scaffold was approximately, 30 μm, with each of the fiber layers approximately 15 μm thick, supported on a base layer covered with a flat 100 nm thick, PMMA spun cast film. Thus the scaffolds were comprised of three layers, a bottom layer which was composed of a spun cast uniform film, and upper layers that were composed of fibers electrospun in perpendicular directions. In this manner we could directly compare the morphology of the cells that diffused all the way to the bottom layer with those that were adhered to the electrospun scaffold. Again here we focused only on the effects of fiber diameter and orientation, rather than pore size. Therefore, we kept the pore size roughly constant.

2.2.4. Cell Culture and Seeding to PMMA Scaffold

AHDF strains were obtained from Clonetics (San Diego, CA). The cells were routinely cultured in Dulbecco's Modified Eagle medium (DMEM) supplemented with 10% fetal bovine serum (Hyclone, Logan, UT) and antibiotic mix of penicillin, treptomycin, and L-glutamine (GIBCO BRL/Life Technologies, Grand Island, NY) in a humidified incubator at 37^oC.

For cell seeding, all PMMA fibrous scaffolds were ultraviolet (UV) light sterilized for 20 minutes. Serum free DMEM containing 30 μg/ml intact human plasma fibronectin (Calbiochem, San Diego, CA) was added into each scaffold and incubated at 37^oC for 2 hours. The cells were then seeded on PMMA fibrous scaffold at a density of 1.25×10^4 cells/cm^2.

2.2.5. Cell Morphology, Stiffness, Proliferation and Migration Study

After incubation for 24 hours, the cells were fixed, permeabilized, then stained with alexa-flour 488 phallodium (Invirogen, Carlsbad, California) and propidium iodide (HPLC, Sigma Chemical Co., St. Louis, MO) for actin cytoskeleton and nucleus visualization, respectively. The morphology of the cells was visualized with a Leica TCS SP2 laser scanning confocal microscopy (Leica micro-system Inc., Bannockburn, IL). The confocal microscope was able to focus on different planes of the sample separately. Hence data could be acquired of cells in each plane, without physical sectioning of the sample. The aspect ratio in each of the sections was then calculated by producing images of the cells in each plane separately. For SEM observation, the cells were fixed, dehydrated in graded concentration of ethanol (30, 50, 70, 90, and 100%) and air dried in a fume hood overnight. Vinculin of the cells was also stained to investigate the distribution of focal adhesion contacts. Briefly, cells were incubated with a primary monoclonal antibody (Sigma Chemical Co., St. Louis, MO) against human vinculin and incubated with a fluorescent-conjugated goat antimouse secondary antibody (Sigma Chemical Co., St. Louis, MO) for 1 hour at room temperature before being imaged.

Relative surface modulus of the PMMA fibers as well as the cells on the difference substrates were measured by a Veeco/DI Dimension 3000 atomic force microscope (AFM). The principle of the shear modulation force microscopy (SMFM) method and the setup of the experiment were introduced in earlier papers [37, 38]. When the drive signal amplitude was varied from 7.5 mV to 125 mV, which corresponded to an x-piezo displacement of 1.5-25 nm, the cantilever response was recorded to estimate the stiffness of the cell surface [39]. At least 10 fibrils were measured from each sample. Each cell was measured at three locations: one at the center and two at a 500 nm off-set from the center. Three measurements were done at each location, totally nine measurements for each cell. Three different cells from each substrate were examined. The experiment was repeated by four times; hence the data represented an average of 36 measurements.

To determine the total number of cells on each substrate, AHDFs were seeded at a density of 1.0×10^4 cells/cm^2 on to 3 different substrates: PMMA spun cast film, random and cross-aligned PMMA scaffold. A lower seeding density was used for proliferation

studies as compared to adhesion studies, since there would be more available area for the cells to proliferate so as to avoid their reaching confluence prematurely. The cells were allowed to proliferate for 2, 4, 7, and 9 days, at which time the cells were stained with 4′, 6-diamiadino-2-phenylindole (DAPI, Sigma-Aldrich Inc., St. Louis, USA), a cell permeable fluorescent DNA binding probe. Photomicrographs of the nuclear-stained cells were obtained (using an inverted Nikon microscope with a CCD camera) on five random fields per sample. The number of cells attached was averaged over several views of the same polymer surface to provide cell attachment as a function of time. Cell counting at each time point was performed in triplicate.

Cell migration was obtained by imaging cells migrating from the agarose drop by a modification of the method described before [40-42]. This assay measured cell migration away from a high density population of cells contained in agarose drop. Cells on different substrates were fixed and stained with DAPI after 4 and 16 hours.

2.2.6. Statistical Analysis

The number of replicates for each experiment was adjusted according to the variance obtained. In graphs, all data were presented as means ± standard deviation and evaluated for difference by ANOVA followed by Tukey post-hoc analysis. Differences were considered significant when $p < 0.05$.

2.3. Results and Discussion

2.3.1. Cell Morphology on Randomly Oriented PMMA Fibers with Different Diameters

Confocal microscope images of the AHDFs cultured for 24 hours on a flat PMMA film and random PMMA fibers with different diameters were shown in Figure 2.4. On the PMMA film substrates, the cells were stretched across the surface with well formed actin fibers spanning the length of the cells (Figure 2.4a). On the smallest fibers (0.16 μm) (Figure 2.4b), most of the AHDFs had similar appearances to those on the flat film. At first glance, the cell morphology appeared to be independent of the underlying fiber structure. Upon closer examination though, the cells on the fibers appeared to have many more fine fibers, or filopodia, emanating from their edges. In Figure 2.4c we showed images of cells plated on substrates with slightly larger fibers of diameter, 0.65 μm. Here most of the cells were well spread, though the cells appeared to have become narrower. Fewer filopodia were observed on the edges of the cells.

In Figure 2.4d we showed the images of the cells plated on the somewhat larger fibers with the diameter of 0.97 μm. In this case the cells were stretched with well defined actin fibers, but they had now become completely oriented along the fibers. It was interesting to note, that there were almost no cells on the flat PMMA substrate, even though there were large exposed areas between the fibers which were covered with the chemically identical materials. Hence cells clearly preferred the fiber surfaces. Finally, in Figure 2.4d we showed the image of cells on fibers of 8.64 μm in diameter. In Figure 2.4f we also showed the SEM image of the cells on the fibers. Here too we could clearly see the narrow fibers which extended from the body of the cells and wrapped around the fiber contours.

Quantitative analysis indicated that the cell area, aspect ratio (the ratio of the long axis to the short axis of an elliptical body) and length of the long axis of AHDFs on PMMA scaffold with fiber diameter of 0.16 and 0.66 μm was not significantly different from that on the spun cast PMMA (control) surface. While the aspect ratio of cells on the PMMA scaffold with diameter of 0.97 and 8.64 μm were higher than the cells on the spun cast

PMMA surface and the PMMA scaffold with diameter of 0.16 and 0.65 μm.

Two plausible explanations for the result were related to the focal adhesion complex in mediating cell adhesion to biomaterial, and the interfiber distance. Immunohistochemical staining for vinculin had shown that focal adhesions can be larger than 1 μm [43, 44]; consequently it was plausible that the submicron fibers undermine cell spreading by limiting the size of focal adhesion [45], which we would discuss later. Another reason for the result was because of a large interfiber distance or a very low surface density of fibers on the last two samples, which did not permit cell adhesion across the neighboring fibers.

The increase of the aspect ratio with increasing fiber diameter was consistent with NIH 3T3 cultured on the poly (D, L-lactic-co-glycolic acid) (PLGA) fibers [35], while different from human umbilical vein endothelial cells (HUVECs) seeded on the poly (L-lactide-co-ε-caprolactone) (PLCL) fabrics [46]. Such differences might be a consequence of cell type and polymer type.

2.3.2. Cell Morphology on Aligned PMMA Fibrous Scaffolds

Fibrous structures are a common scaffold in living tissue, where the fiber orientation is often an important factor in cell differentiation and function. In order to mimic the natural order of the cells, the effects of orientation and dimensionality of the fibers on cell structure have been studied [45, 47, 48]. Here we extended these studies to three dimensional with a square weave, i.e. the fibers in adjacent layers were lying at 90 degrees to each other. In this manner a controlled porosity was engineered in the scaffold.

The effects of the fiber alignment on the cell morphology were shown in Figure 2.6, where we could see that on the thin film and random fibrous substrate, the cells were randomly oriented and spread over a large area. On the aligned substrate, the cells were oriented along the fibers. From the images we could also see that even though some cells span two layers, most of the cells were extended only in one layer and along one fiber direction. Occasionally, if the fiber density was high, we could also see some cells that were extended to span two adjacent fibers. Figure 2.6f was a SEM image of an oriented scaffold with cells. From this image we could clearly see that small filopodia were clearly observed which emanated from the cell and wrapped around the fibers, as the cell explored its environment.

Cells were present in all layers of the scaffold (Figure 2.6c-e), indicating that cell migration throughout the 3D structure had occurred. On the other hand, the cells stopped at the last fiber layer and very few migrated down to the flat PMMA film surface (Figure 2.6e). Here too we found that even though the surface chemistry was identical the cells preferred the fibers. We could also see from the figures that the cell morphology was also relatively insensitive to the pore diameter as long as it was larger than that of the cell.

Despite the penetration of cells all the way to the bottom layer of the scaffold, it was interesting to note that the cells in each layer were in registry with the fibers of that layer, and their long axis was parallel to the fibers in their layers. It was rare to observed cells whose long axis were perpendicular to the fiber layers and span adjacent layers; even though the space between the layers was smaller than the cell length. This was probably due to the fact that the cell preferred the substrate at the same height.

2.3.3. Vinculin Staining

Vinculin is a ubiquitously expressed actin-binding protein frequently used as a marker for both cell-cell and cell- extracellular matrix (focal adhesion) adherents-type junctions [49]. In order to determine whether the underlying structure had an affect on the spatial distribution of focal adhesion contacts, the cells were stained to visualize the vinculin by fluorescent microscopy. On the control sample (Figure 2.7a), where the cells were spread on the flat PMMA film, we found that the vinculin containing focal adhesion points, which were stained green, were clustered around the cell periphery. This was consistent with the observed actin structures, where the fibers were anchored onto the integrin receptors, as previously reported [50, 51]. In contrast, the vinculin on the cells plated on the 0.16 μm fibers (Figure 2.7b), were no longer concentrated in any area, but appeared to be scattered across the cell surface. This was intriguing since the actin fiber formations were similar to those of the cells on the flat surfaces. A similar, non-localized distribution was also observed for the cells on the thicker, 0.65 μm fibers (Figure 2.7c). In Figure 2.7d and 2.7e we now showed the images of the cells plated on the larger fibers. In this case, the focal adhesions were clearly oriented along the edge of the fiber, where we had previously observed the cell to be adherent. These results indicated that the focal adhesions could easily follow features that were on the micron scale. Features produced

by fibers whose diameters were smaller than a micron, were more complex. The cells produced small fibers on the surface, and an apparent chaotic focal adhesions organization, which might reflect the position of the fibers under the cells.

2.3.4. Bulk Mechanical Properties of Electrospun Scaffolds

The relative moduli of the fibers and the films were measured using the shear modulated force microscopy (SMFM) method. This technique was based on modulating the tip of the atomic force microscope and determining the deflection of the cantilever (ΔX). Using Herzian mechanics, it was shown that the deflection was related to the surface modulus (G) $\Delta X = KG^{-0.66}$, where K was a constant for a given polymer. In Figure 2.8a and 2.8b we showed the deflection as a function of applied voltage on the tip. From the figure we found that the deflection was linear with voltage indicating that the tip was well engaged and no slippage was occurring. ΔX, was determined by the slopes of the curves, which could be seen to be different on the different substrates. In Figure 2.8c, we plotted the relative moduli and found that the spun cast film was the hardest, as expected, since it was the closest to the Si substrate. The moduli of the aligned and random 8.64 μm diameter fibers were similar, consistent with the observations of Baker *et al* [45]. From the Figure 2.8d we could see that the moduli of the cells were distinctly harder on the thin film substrates, than on the fibrous ones. No difference was observed though between the random and aligned fibers, indicating that the local dimension of the fiber, rather than its orientation relative to other fibers was the determination factor in the cell modulus.

We could therefore see from the Figure 2.4 and Figure 2.7 that the actin fibers, which terminated on the focal adhesion points, were more extended on the flat surface, where they could be spread without restrictions. On the fibers though, the actin was seen to follow the fiber contours, and the vinculin terminus were on the edge of the fiber. As a result, the acting filaments were short and not as well extended. Previous studies had demonstrated that the mechanical response of the cell was closely associated with the shape of the internal actin structure [49, 52, 53]. The internal structures composed of the shorter fibers therefore were not as hard as those on the extended geometries on the flat surfaces.

2.3.5. Cell Proliferation Studies

Proliferation of cells seeded into scaffolds generally was required to generate a tissue-like structure. We therefore measured the proliferation of fibroblasts on the spun cast PMMA films, random and cross-aligned PMMA mesh with fiber diameter of 8.64 μm. The number of cells measured in a unit volume after 2, 4, 7, and 9 day incubations was plotted Figure 2.9. From the figure we could see that the number of cells after two days of incubation was similar for all substrates, indicating that the plating efficiency did not depend on the substrate. Differences in the cell counts became apparent at day 9, where the proliferation rate on the flat surface was greatly decreased. Confocal images of the cells at day 9 were shown in Figure 2.10. Here we could see dramatic differences in the morphology. In the case of the flat substrate, the cells had formed a monolayer of tissue, where they were clearly confluent, which was consistent with the decrease in proliferation rate. On the other hand, on the electropsun substrates the cell aspect ratio allowed for a much denser packing without the cells having physical contact. Hence even though there were more cells, they were not confluent yet. Furthermore, since the fibers formed a 3D structure, there was much more room for further growth. While the cell counts were comparable between the aligned and random structures, one could see that the aligned structures allowed for even greater penetration, since the cells were better ordered.

2.3.6. Cell Morphology on a Heterogeneous Construction Fiber Mat

A major advantage of the mat construction was the fact that fibers of different diameters or orientation could easily be produced in one scaffold. In order to test whether cells or different morphology could then coexist on one scaffold, we produced 8.64 μm cross-aligned fibers deposited on a layer of 0.16 μm random fibers, and then cultured the cells on the heterogeneous matrix (Figure 2.11a). We found that cells of two different morphologies were now formed. The aspect ratios of the cells on the lower and upper layers were plotted in Figure 2.11b, where we could see that the values obtained were similar to those shown in Figure 2.4b, where the cells were cultured separately on the two different matrixes. The cells on the nanofiber, were well spread, while those on the 8.64

μm fibers had a larger aspect ratio and were oriented along the fiber directions. Hence these fiber constructs could be engineered to allow cells with different properties to coexist in close proximity, where they could interact with each other, as well as with the substrate.

2.3.7. Cell Migration out of Agarose Droplets into Electrospun Fiber Scaffolds

In order to determine whether the presence of fibers and the changes in cell morphology affected cell mobility, we used the traditional agarose droplet spreading method to compare the cell migration out of the droplet onto flat and fibrillar surfaces. In this method the cell diffusion was determined by measuring the spreading of the corona observed at the periphery of the droplet as the cells migrated away from the denser core.

After 4 hours of incubation, not much cell migration was observed on the PMMA spun cast film and the boundary of the core was sharp (Figure 2.12a). After 16 hours of incubation, we could see a well defined corona which was less dense than the core and corresponded to the cells migrating from a high to low cell density region (Figure 2.12b). While compared with cells on PMMA aligned fibrous scaffold, there were two fundamental differences in the migration process. After 4 hours, the droplet on the oriented fibers did not have a sharp domain boundary and the density of the cell was not uniform (Figure 2.12c). After 16 hours the differences became even sharper. Three regions were visible on the oriented matrix, a low density interior, a high density ring, and a very low density corona emanating from the ring (Figure 2.12d). In order to understand these differences, we showed magnified sections of these different regions. In the control sample after 16 hours the cells in the corona were elongated, as expected for migrating cells and the directions of migration was radial away from the core (Figure 2.12f). In the case of the cells on the oriented matrix, we could see that most of the cells were already oriented in the cross hatched pattern of the matrix (Figure 2.12g), even just after 4 hours of incubation, indicating that the agarose droplet and the cells had penetrated into the matrix. After 16 hours, careful study of the droplet showed that the outer corona was clearly composed of individual cells highly oriented along fiber directions, with a nearly uniform spacing between cells, migrating away from the denser ring (Figure 2. 12h). From these images we could see that substrate morphology had a

large affect on the migration, and the detailed results will be discussed in a subsequent chapter.

2.4. Conclusion

In conclusion, we had obtained electrospun PMMA fibers of different diameters, ranging from 0.16 to 8.64 μm. Furthermore, using a rotating drum, a multi layer of cross-aligned fibrous scaffold could be formed. AHDFs were plated on the fibers and we found that cells preferred to orient along the fiber axis when the diameter was above the critical value $D_0 = 0.97$ μm. No alignment was observed below this value.

We also found that only when fiber diameters above D_0, the integrin receptors could follow the edge of the fiber contour. Mechanical measurements showed that cells on the aligned fibers were softer than those on the flat films, mostly due to the constricted position of the integrin receptors and the actin filaments.

Cell proliferation measurements on the other hand, indicated that the process on the aligned fibers was more efficient since the oriented cells did not become confluent as quick as on the spun cast film. Different cell morphologies were observed on the same sample of random PMMA fibers with diameter of 0.16 μm on the bottom and 8.64 μm on the top, indicating that scaffolds could be designed which allowed cells with different properties to coexist in close proximity. Finally, fiber orientation was also shown to affect cell migration, which might also be an important factor for consideration of these scaffolds as cell delivery mechanisms for wound repair [54].

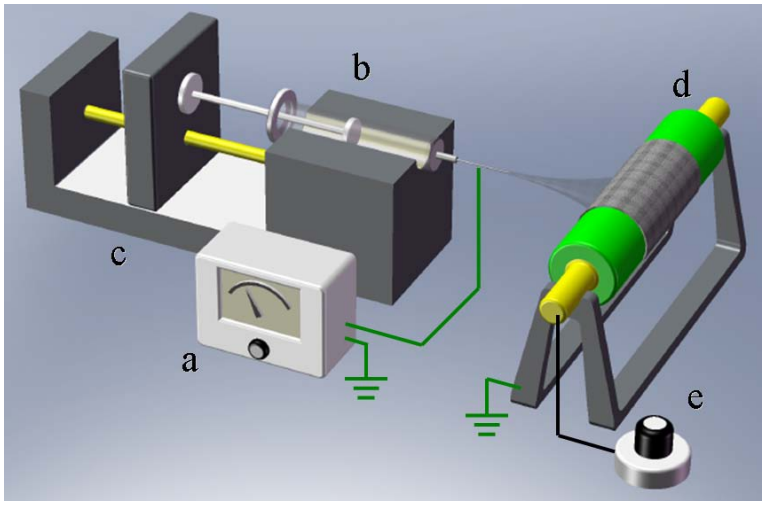

Figure 2.1. Schematic of the electrospinning apparatus.
The polymer solution was loaded in the syringe and 5-8 kV supplied by (a) a high-voltage power supply was applied between (b) the needle and the ground. The flow rate of solution, approximately 20 μl/min, was controlled by the (c) syringe pump. Two targets were used, a stationary aluminum disc or (d) a rotating drum wrapped in aluminum foil. The alignment was controlled by (e) the motor speed rotation.

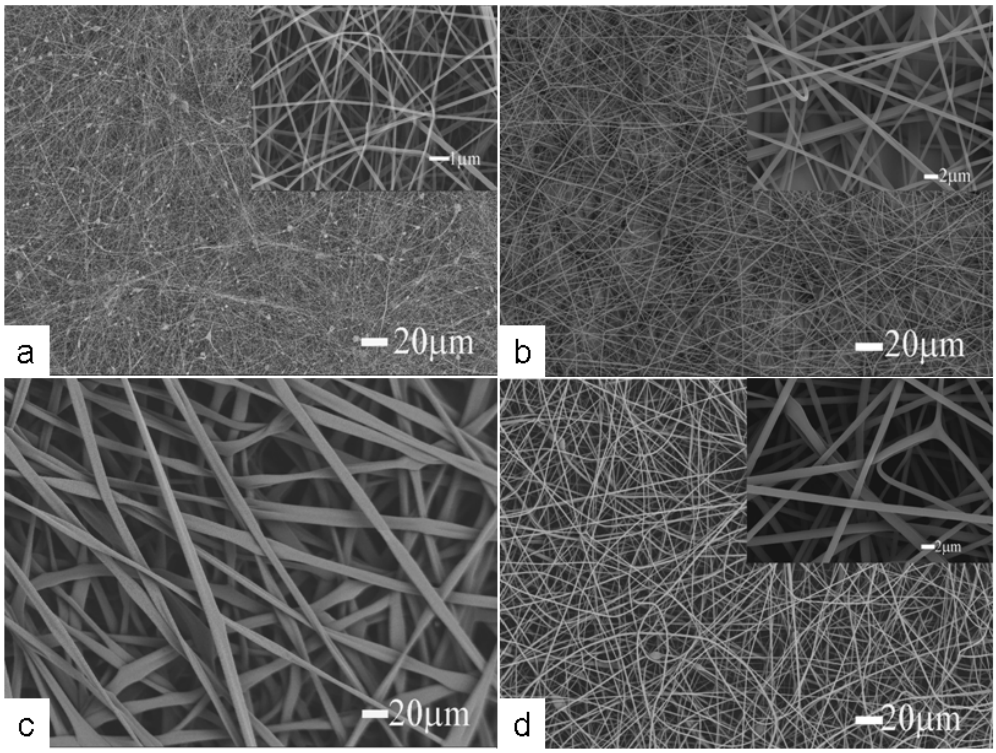

Figure 2.2. SEM micrographs of electrospun PMMA fibers from 20wt% PMMA solutions with: (a) 80wt% DMF with addition of 5wt% TBAC (with respect to PMMA), (b) 40wt% THF and 40wt% DMF and (c) 80wt% chloroform. (d) Micrograph of PMMA fibers electrospun from 30% (w/w) PMMA in mixed solvent of THF and DMF with weight ratio of 1:1.

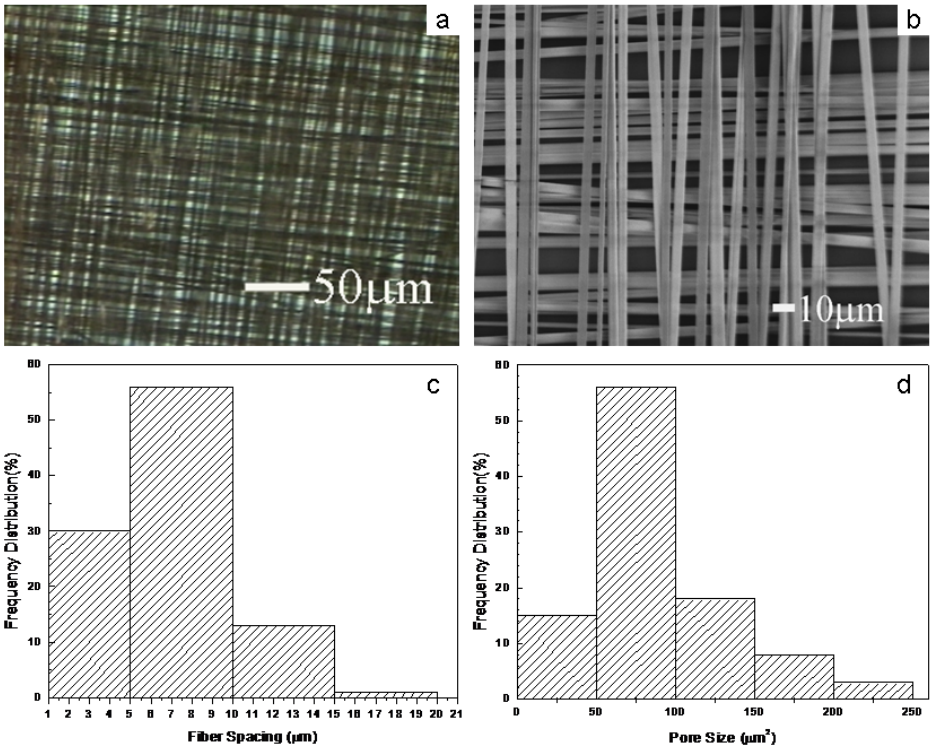

Figure 2.3. (a) Optical and (b) SEM images of aligned PMMA scaffolds electrospun from 20wt% PMMA and 80wt% chloroform with an applied voltage of 5-8 kV, flow rate of 20 μl/min, working distance of 5cm, collected with a mandrel rotation speed of 6750 r/min. (c) and (d) were frequency distribution of the spacing between adjacent fibers and pore size.
Data obtained from 5 independent samples and each sample with 50 numbers.

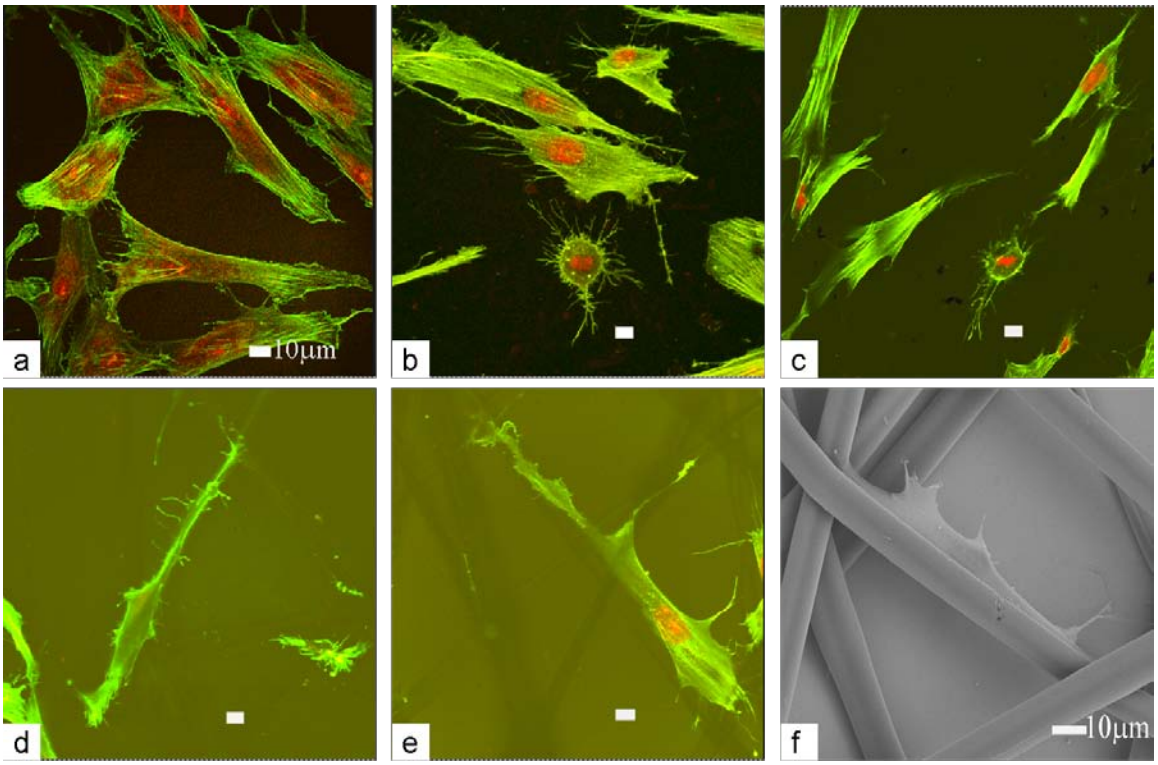

Figure 2.4. Confocal images showing the morphologies of AHDF cells plated on FN-adsorbed (a)flat spun cast film surface and unoriented scaffolds with fibers having diameters of (b) 0.16 μm, (c) 0.65 μm, (d) 0.97 μm, and (e) 8.64 μm. F-actin was visualized as green, and the nuclei were visualized as red in the Confocal images. (f)SEM Image obtained from cells cultured on fibers and dried in alcohol solution on fibers with diameter of 8.64 μm. Note that the cells (f) adhered to the narrower sides gave us better contrast than cells on the flat side of the fiber.

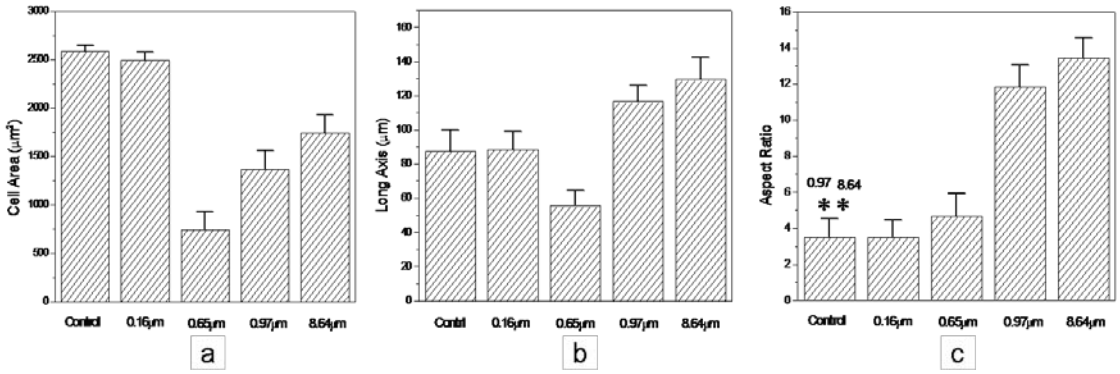

Figure 2.5. Effects of PMMA fiber diameter on (a) projected cell area, (b) length of long axis, (c) aspect ratio. Controls were spun cast PMMA films.
Error bars correspond to the standard deviation for n=50 cells. The experiments shown were representative of 4 independent experiments.* indicated $p < 0.05$.

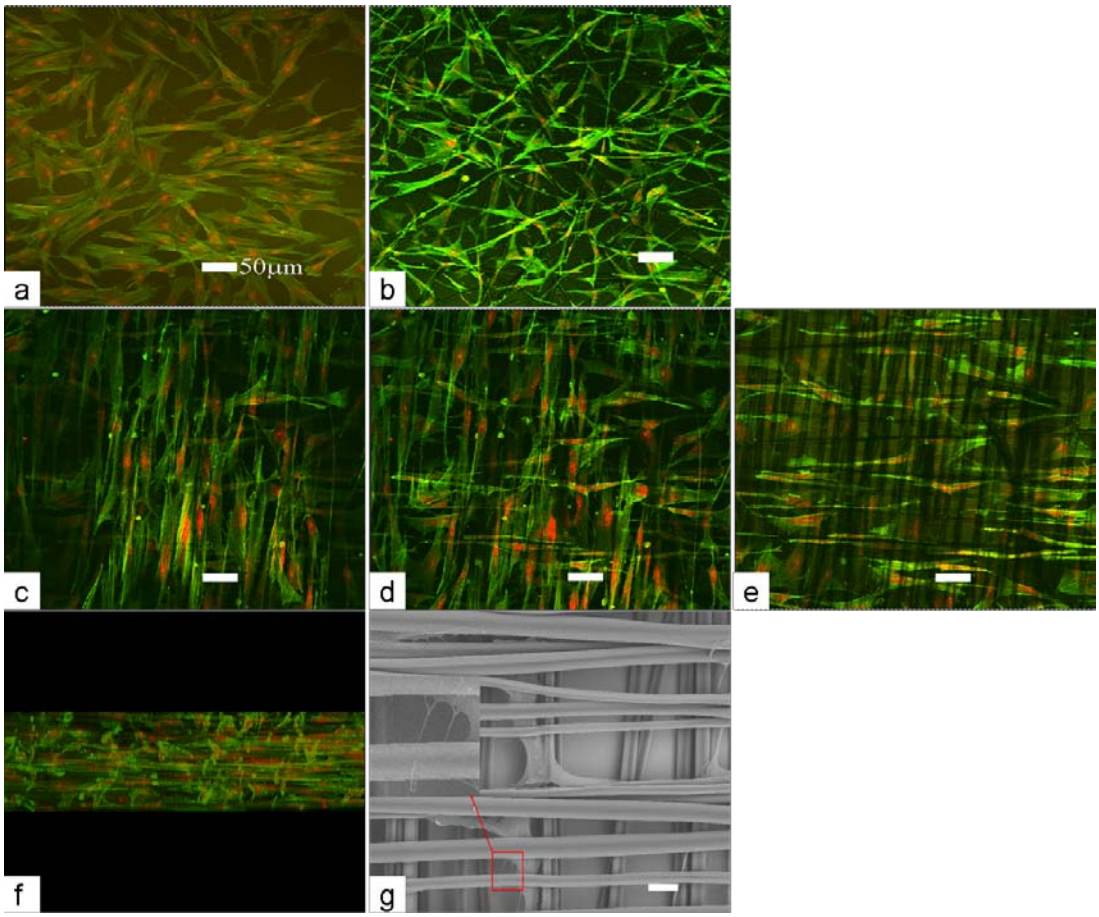

Figure 2.6. Morphologies of AHDF cells incubated for 24 hours with initial plating density of 2.5×10^4cells/cm^2 on FN-adsorbed: (a) PMMA spun cast film; (b) PMMA unoriented scaffold, with fiber diameter of 8.64 μm; (c) on the surface of cross-aligned PMMA scaffold; (d) approximately 15μm beneath the surface of PMMA scaffolds; and (e) approximately 30 μm beneath the surface of PMMA scaffolds at the plane of furthest cell invasion. (f) Cross sectional view of AHDFs on the FN-adsorbed cross-aligned PMMA scaffold. (g) SEM image of AHDF on the FN-adsorbed PMMA cross-aligned scaffold. (Inset: small filopodia were observed which emanated from the cell and wrapped around the fibers, as the cell explored its environment.)

The F-actin was visualized as green, and the nuclei were visualized as red in the Confocal images. The cells on the top layer were seen to move along the fiber orientation in that layer. The cell on the lower layer, aligned at 90 degree to the upper layer, or in the direction of the fibers in that layer.

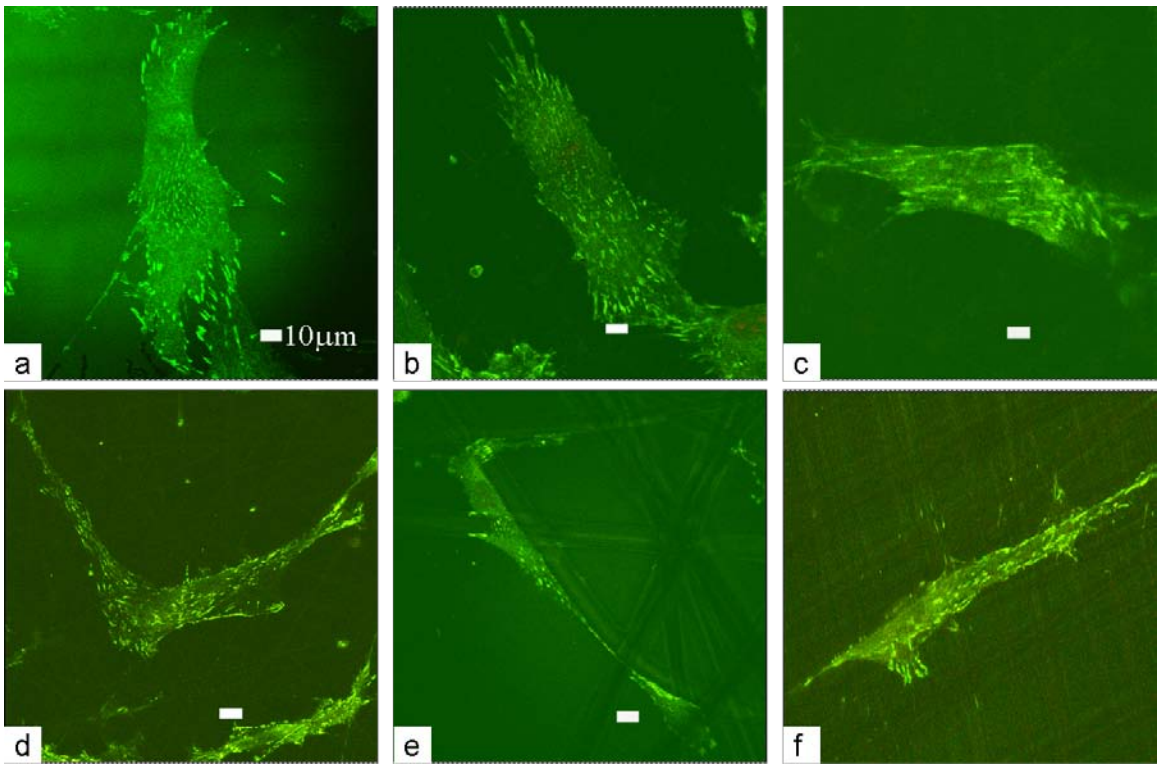

Figure 2.7. Immunofluorescent vinculin staining of the integrin receptors adherent AHDFs on FN-adsorbed (a) spun cast flat PMMA film, (b) PMMA random mesh substrates composed of fiber mats having diameters of (b) 0.16 μm, (c) 0.65 μm, (d) 0.97 μm, (e) 8.64 μm and (f) PMMA cross-aligned mesh with fiber diameter of 8.64 μm.

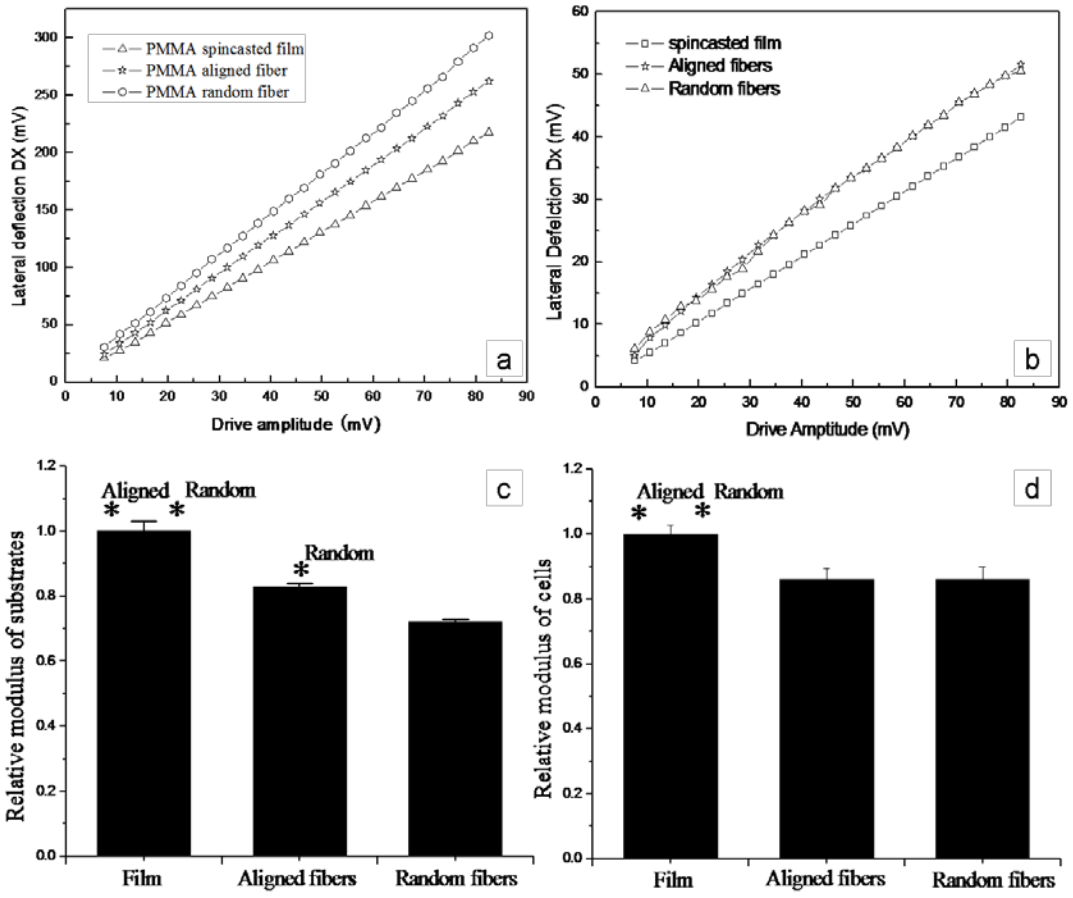

Figure 2.8. Lateral deflection Δx as a function of the drive amplitude for FN-adsorbed (a) PMMA spun cast film, random and aligned scaffold; (b) AHDFs cultured on the PMMA spun cast film, random and aligned scaffold for 24 hours. The AFM response amplitude generated from cell's resistance to cantilever indentation increased linearly with the cantilever drive amplitude, which indicated there was no slip between the AFM tip and cell surface. Relative modulus of three different substrates: (c) PMMA spun cast film, random and aligned scaffold, and (d) AHDF cells on cultured on those three substrates.

Each bar represents the mean ± standard deviation of repeated experiment. The experiments shown were average of all the 36 measurements. * indicated $p < 0.05$.

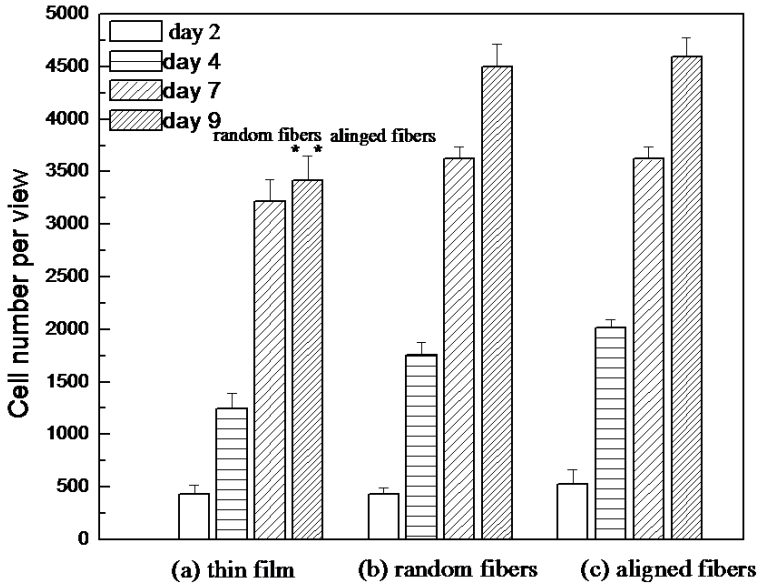

Figure 2.9. Proliferation of AHDF cells on the FN-adsorbed three different substrates with initial density of 1.0×10^4 cells/cm^2 following in vitro culture for 2, 4, 7and 9 days in complete medium: (a) PMMA spun cast film, (b) PMMA random fibers and (c) PMMA cross- aligned fibers.

Each bar represents the mean ± standard deviation of triplicates. The experiments shown were representative of 4 independent experiments. * indicated $p < 0.05$.

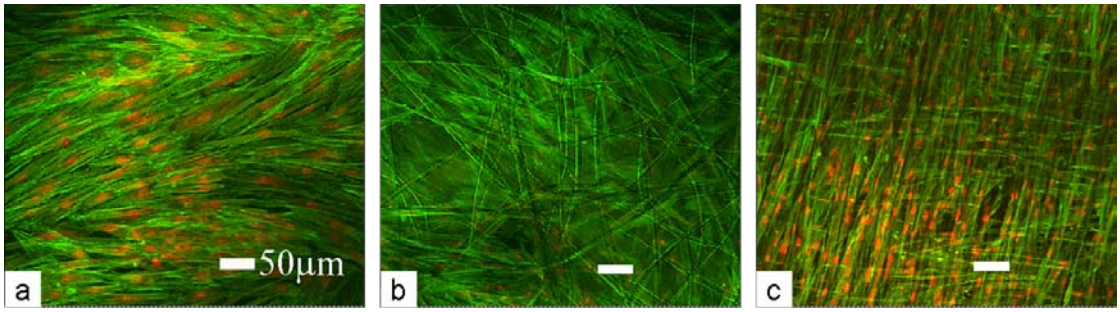

Figure 2.10. The morphologies of AHDFs plated on the FN-adsorbed different substrates with initial density of 1.0×10^4 cells/cm^2 and incubated for 9 days: (a) PMMA spun cast film, (b) PMMA random scaffold and (c) cross-aligned fibrous scaffold with fiber diameter of 8.64 μm.
F-actin was visualized as green, and the nuclei were visualized as red in the Confocal images.

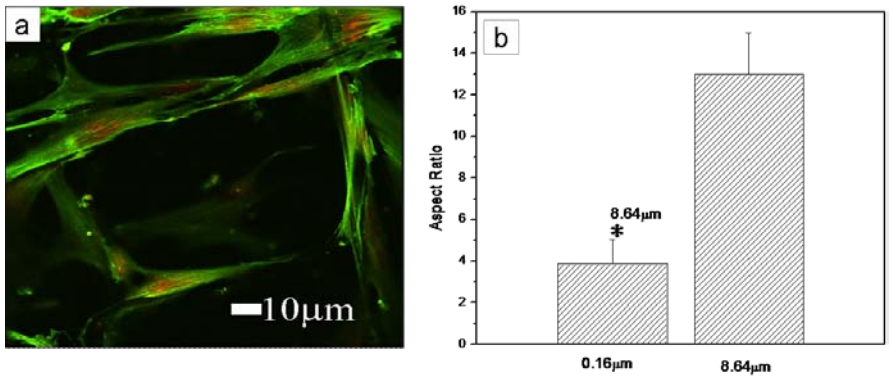

Figure 2.11. (a) Morphology of AHDFs plated on a FN-adsorbed two level mesh, where the diameters of the fibers on the lower and upper levels were 0.16 μm and 8.64 μm, respectively. The image was taken on the surface of cross-aligned PMMA scaffold. (b) The aspect ratio of the AHDFs plated on upper and lower level of the scaffold.
F-actin was visualized as green, and the nuclei were visualized as red in the confocal images. * indicated $p < 0.05$.

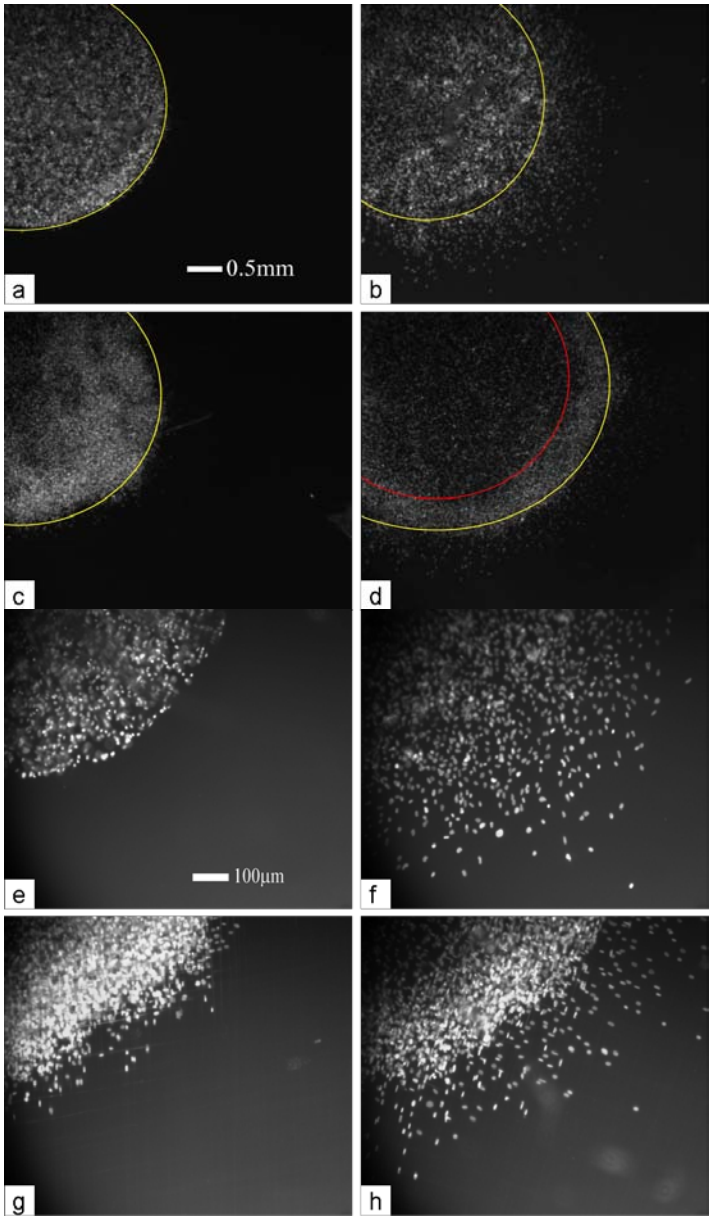

Figure 2.12. Migration of cells from an agarose drop after 4 and 16 hours respectively onto FN-adsorbed (a and b) flat spun cast films and cross aligned fibrous scaffolds (c and d). The ring surrounds the periphery of the original droplets. The cell mobility is determined by the ability of the cells to migrate outside of the specified core area. From the figure we find that standard analysis is no longer applicable. A higher magnification portion (e) (f) (g) (h) of the images (a) and (b), as well as (c) and (d) showing the position of the cells relative to that of the fibers. Cells were stained with DAPI to visualize the nuclei.

Sample	Mean diameter and distribution of the fiber (μm)
20wt%PMMA in DMF and 5% Tetrabutylammonium chloride (TBAC, with wt% respect to PMMA)	0.16±0.05
20wt% PMMA in THF/DMF(1:1, w/w)	0.65±0.18
30wt% PMMA in THF/DMF（1:1, w/w）	0.97±0.16
20wt% PMMA in Chloroform	8.64±1.28

Table 2.1. Diameters of electrospun PMMA fibers fabricated from different PMMA solutions.

Chapter 3. Control of Cell Migration in Two and Three Dimensions Using Substrate Morphology

3.1. Introduction

Dermal wound repair is a complex process requiring coordination of several biological responses, such as cell proliferation, organization of the extracellular matrix (ECM), and rapid wound coverage [56]. It is well established that cell migration is one of the critical factors in all these processes and hence the process has been the subject of much interest for many years [57, 58]. Even though the mechanisms and regulation of cell migration have been studied extensively on numerous substrates [59], the surfaces were mostly planar. The research on three dimension (3D) migration may be even more relevant to understand the processes involved in wound healing or tissue engineering, since *in vivo* cells migrate on the ECM, which is fibrillar [50-62]. Recently Grinnell *et al.* have shown that the morphology of cells on collagen fibers was different than on flat surfaces and hence the migration of cells on 3D collagen matrices was also different [63-66]. Furthermore, on fibers one was also able to observe the effects of orientation on migration which is known to be an important aspect in scar free wound healing [67-71]. However, most of these previous studies have focused on the interplay between polarization and migration for isolated cells [68, 70-72]. The wound healing process though involves en mass migration of a large number of cells [73], whose motion is highly correlated. The ability to construct fibrillar scaffolds with specific orientation allows us to control the cell-cell correlations and quantitatively compare the en masse migration patterns in two and three dimensions.

In our study, we chose to study human dermal fibroblasts migration on fibronetin-coated flat and fibrillar poly (methyl methacrylate) (PMMA) substrates. PMMA is a glassy polymer (Tg~100 ^{0}C, E~5.1 Gpa) which can be easily electrospun into fibers of different diameters and would not deform under the typical traction forces exerted by migrating cells, F~1×10^{5}dyns/cm^{2} [74].

The technique we used involves observation of outward migration from an agarose droplet. This technique is based on the principal that when cells are concentrated in a gel, they will migrate to regions of lower cell density. It has been shown previously that the morphology of human dermal fibroblasts is a function of the morphology of the underlying substrates [75]. Here we show that the rate of migration can also depend on the microstructure parameters of the underlying substrate, such that on the flat surfaces the speed decreases with increasing incubation time, whereas on the aligned fibrous scaffold cells can migrate for very long distances in a highly correlated fashion with constant velocity.

3.2. Experimental Section

3.2.1. Fabrication and Characterization of the PMMA Thin Film and Scaffold

Solutions of PMMA (M_w=120 kDa, $M_w / M_n = 3$, Sigma-Aldrich Inc., St. Louis, MO) were made in toluene (Fisher Scientific, Pittsburgh, PA) at a concentration of 30 mg/ml and spun cast onto the clean glass coverslips using a photoresist spinner with a frequency of 25000 PRM. The film thickness was determined by ellipsometry to be approximately 100 nm. The polymer-coated coverslips were then annealed at 120^0C in a vacuum of 10^{-7} Torr for 12 hours to remove the residual solvent. Similar substrates were also prepared as targets for the electrospun fibers. This served a two folds purpose: (a) the small amount of residual solvent plasticized the film and allowed the fibers to adhere; (b) placing the fibers onto a chemically identical substrate allowed for a direct comparison of the cell structure on flat and fibrillar surfaces.

The substrates used for measuring the two dimensional (2D) migration out of the droplet consisted of a single layer of random or parallel fibers support on the flat PMMA coated substrates (Figure 3.1). The substrates used for measuring 3D migrations consisted of two layers of fibers, oriented at 90º to each other and adhered to the flat film. The fabrication and characterization of the PMMA electrospun fibers has been discussed in previous paper [75]. Basically, highly aligned PMMA fibrous scaffold were obtained by electrospinning the PMMA solution and collecting the fiber with the rotating drum at a speed of 6750 r/min. The approximate distance between adjacent fibers could be controlled by the collection time. In further to fabricate the cross-aligned PMMA fibrous scaffold, the sample was removed and rotated to 90º and the procedure was repeated for the next layers. In this manner, a layer by layer, 3D construct could be built with roughly controlled spacing.

The fiber diameter distribution of PMMA scaffolds was calculated by analyzing scanning electron microscope (SEM) images with Image Tool (The University of Texas Health Science Center in San Antonio). For cell seeding, fiber-carrying coverslips were sterilized with ultraviolet (UV) light for 20 minutes. Serum free Dulbecco's Modified

Eagle medium (DMEM) containing 30 μg/ml intact human plasma fibronectin (Fn) (Calbiochem, San Diego, CA) was added into each sample and incubated at 37 ^{0}C for 2 hours.

3.2.2. Cell Culture and Membrane Staining

Human dermal fibroblast strains were obtained from Clonetics (San Diego, CA) and used between passages 11 and 12. The cells were cultured in DMEM supplemented with 10% fetal bovine serum (HyClone, Logan, UT) and an antibiotic mix of penicillin, strepmycin, and L-Glutamine (full-DEMEM), in a 37 ^{0}C, 5% CO_2, 95% humidity incubator (Napco Scientific Company, Tualatin, OR).

The standard phase-contrast microscopy limited the visualization of the cells on the fiber. To visualize the cells under fluorescent microscopy in real time, cell membranes were stained with 1,1'-dioctadecyl-3,3,3',3'-tetramethylindodicarbocyanine perchlorate (DiD, Invitrogen, Carlsbad, CA). The DiD lipid-labeling procedure was obtained by a modification of the manufacturer's instruction. Briefly, cells were washed well with phosphate buffer saline (PBS) and re-suspended at a density of 1×10^6 cells/ml in serum free DMEM containing DiD at 3.5 μg/ml, incubated for 30 minutes at 37 ^{0}C. The labeled suspension tubes were centrifuged and the supernatant was removed.

3.2.3. Cellular F-actin Cytoskeleton and Nucleus Organization

After incubation for a predetermined time, cells were fixed, permeabilized, followed by stained with Alexa Fluor 488 Phalloidin (Invitrogen, Carlsbad, CA) and propidium iodide (PI, Sigma Chemical Co., St. Louis, MO) for actin cytoskeleton and nucleus, respectively. The morphology of the cells was visualized with Nikon Diaphot-TMD inverted microscope or Leica TCS SP2 laser scanning confocal microscope (LSCM, Leica microsystem Inc., Bannock burn, IL), depending on the experiment purpose.

To determine the total number of cells on each substrate, cells were stained with 4′, 6-diamiadino-2-phenylindole (DAPI, Sigma-Aldrich Inc., St. Louis, MO), a cell permeable fluorescent DNA binding probe. The number of cells which migrated out from the agarose drop was averaged over several views of the same substrate. Cell counting at

each time point was repeated at least 4 times.

Samples had to be dried in order to prepare for SEM analyses. This was accomplished by cell dehydration procedure, which involved successive immersion in solutions of graded concentration of ethanol (30, 50, 70, 90 and 100%) for 10 minutes, followed by air drying overnight in a fume hood.

3.2.4. Immunolocalisation of Vinculin

Cells were washed with PBS, fixed, permeabilized and blocked with 2% (w/v) BSA in PBS for 30 minutes at room temperature. Then cells were incubated with a primary monoclonal antibody (Sigma Chemical Co., St. Louis, MO) against human vinculin and a fluorescent-conjugated goat antimouse secondary antibody (Sigma Chemical Co., St. Louis, MO) for 1 hour at room temperature before being imaged using LSCM. Here cells were stained with rhodamine phalloidin (Molecular Probes, Eugene, OR) to determine the F-actin structure.

3.2.5. Assessment of Cell Migration on Different PMMA Substrates

The agarose drop assay is a method that is frequently used to analyze cell mobility [76]. This method is performed by packing cells at high density in a small drop of agarose placed on the substrate to be studied. Migratory properties of cells are then evaluated by measuring the ability of the cells to migrate out of the agarose drop. Fibroblasts to be tested were stained with DiD as described above, and then re-suspended in a volume of 0.2% (w/v) agarose solution to obtain the final cell density of 1.5×10^7 cells/ml. Droplets of 1.25 μl the cell suspension were delivered with a sterile micropipette into the wells with deferent substrates. The wells were then placed at 4 ^{0}C for 15 minutes to allow the agarose to solidify. After cooling, the agarose droplets were covered with full-DMEM gently.

After incubation for a predetermined time, time-lapse images of the cells were recorded every 15 minutes for up to 60 minutes with a MetaMorph®-operated CoolSNAP^{TM} HQ camera (Universal Imaging Corporation, Downingtown, PA) attached to a Nikon Diaphot-TMD inverted microscope fitted with a 37 ^{0}C incubator stage and a

10 × objective lens. The degree of cell migration was determined by measuring the radius of the cells that migrated away from the drop boundary and into the external environment of substrates. The position of each cell within a field was defined as the position of the cell nucleus. For each sample, migration speed was determined from the time-lapse images using MetaMorph®, which tracked the distance covered by the center of a nucleus every 15 minutes over a period of 1 hour. The same measurement was done after 6, 16 and 24 hours of cell culture. The point of these data was not to examine the details of mobility within one hour, but to determine the trend over 24 hours. Each measurement represents the average and standard deviation for 20 cells, with 3 duplicates and the entire curve was repeated at least 4 times. Cells were exposed to the fluorescent light for 1 second per snapshot when snapshots of the target field were taken by the computer. Therefore, over a 1 hour period, the total exposure is limited to 5 seconds, which should have a minimal, if any effect on cell function [77-79].

The time-series movie of an area was replayed, and the sample/stage movement was corrected by manually defining the reference point in the frames. The pixel number was converted into μm by the scale calibration. The movie was threshold to identify individual cells, and each cell was traced throughout the frames automatically. The path of each cell was generated from the positions of the nucleus at different points. Dividing cells and cells not in contact with each other during migration were excluded. The cells that went out of the focus plane were also excluded. The migration speed and persistence were calculated for each time interval and each cell.

The tracked distances of the center of the nucleus within 1 hour were summed to give the length of the cell path (S). The methodology for measuring parameters of the behavior of cells has been described earlier [72, 80]. Briefly: 1) The mean speed of cell movement (V) was calculated using the equation: $V = S/t$, where S is the length of the total cell path (μm) within 1 hour at different time point (after 6 hours, 16 hours and 24 hours cell culture), t is the duration of the recording (1 hour). 2) The total cell translocation, which is defined as the linear distance between the first and the last point of the cell path within 1 hour at different time point (after 6 hours, 16 hours and 24 hours cell culture. 3) Persistence parameter (Pr): Pr = total cell translocation/ total length of cell path (S) for cells migration within 1 hour. Pr would be equal to 1 for the cell

moving persistently along one straight line in one direction.

The migration distance of cells on each sample was also measured after 24 hours. Cell migration distance was assessed by measuring the distance from the edge of the agarose drop to the population of cells most distant from the agarose drop.

3.2.6. Statistical Analysis

The number of replicates for each experiment was adjusted according to the variance obtained. In graphs, all data are presented as means $\pm$ standard deviation (s.d.) and evaluated for difference by ANOVA followed by Tukey post-hoc analysis. Differences were considered significant when $p < 0.05$.

3.3. Results and Discussion

3.3.1. Fibroblasts Migrating on PMMA Spun Cast Film, Random and Aligned PMMA Fibrous Scaffold

In Figure 3.2a we show a fluorescence microscopy image of the droplet after 4 hours of incubation. In this case the live stain was used on the cells before encapsulation in agarose drop. Hence the image shows mainly the extent of the droplet before spreading. The sample was then incubated for another 20 hours. The fluorescence microscopy image, obtained with the same magnification is shown in Figure 3.2b. From this image it was difficult to determine the distance that the cells had migrated from the droplet. We therefore tried another method. After the 20 hours incubation, we then fixed and stained the F-actin of the cells using Alexa Fluor. In Figure 3.2c we overlapped the image obtained from the fixed sample with the image obtained after 4 hours. Here we can now clearly see the cells that had migrated out of the original droplet and the stain also allows us to determine the cytoskeleton structure of the cells.

In order to determine the effect of substrata morphology on the cell migration, we analyzed these images more closely. If we followed the cells along different radial direction of the migration, we could measure their aspect ratio as a function of distance from the droplet rim. The result is plotted in Figure 3.2d, where we found a decay curve, indicating that as the density of the cells decreased, the cell elongation decreased. In the high density regions their aspect ratios were large as they try to minimize cell-cell contacts. In the perimeter of the drop we observed cells had spread and triangulated, now that the local cell density had decreased.

Previously we showed that the appearance of cells on an electrospun fiber mat, whose diameter was smaller than one micron, was similar to that of cells cultured on a flat film [75]. Here we want to probe the effects of this substrate on the migration properties. We therefore deposited an agarose droplet with cells onto a randomly oriented layer of electrospun fibers 200 nm in diameter. The living stained cells after 24 hours of incubation are shown in Figure 3.3a. The superimposed image of the live stain and the fixed cells after 24 hours of incubation is shown in Figure 3.3b. From the figure we can

see that here too, the cells appeared to migrate radially. Closer inspection though, revealed that the center droplet had formed a ring (Figure 3.3a) and that the aspect ratio (Figure 3.3c) of cells outside of the droplet came out in a manner similar to that of the cells on the flat film.

In Figure 3.4a and 3.4b we show the images that were obtained when the agarose droplets were placed on randomly oriented scaffolds where the fibers were 1 and 8 μm in diameter. Here we see that a much more pronounced ring had formed after 24 hours. Examination of the images shows that, in contrast to cells on the 200 nm scaffold, the cells were oriented along the scaffold fibers and closely followed the fiber contours (Figure 3.4c and 3.4d). No significant differences in morphology were observed for cells plated on randomly oriented fibers between the 1 and 8 μm in diameter. From the figure we can also see that nearly all the cells were oriented along the fibers for the 1 and 8 μm scaffolds, despite the fact that the fibers were lying on a spun cast film produced from the same polymer, PMMA, as the electrospun fibers. This indicates that morphology may be a more important consideration in cell migration than chemistry.

In addition to fiber diameter, orientation is another crucial parameter which can determine cell migration [67, 81, 82]. To detect the effect of fiber orientation, the agarose droplet was placed on a PMMA scaffold composed of aligned fibers 8 μm in diameter. After 24 hours incubation, three regions were visible; a low density interior region inside the droplet, a high density ring at the edge of the droplet, and a lower, but uniform density stream of cells emanating from the ring (Figure 3.5a). Another image of this cell is shown in Figure 3.5b where we stained the cells for F-actin and superimposed the image on the original live stained image taken after 4 hours. We then analyzed this image and plotted the aspect ratio (Figure 3.5c) for a drop that was incubated on the aligned substrate for 24 hours. From the figure we can see that the aspect ratio was constant, since the cell orientation was assumed immediately after the cells exited from the droplet. In Figure 3.5d we plotted the density as a function of distance from the edge (red) of the agarose gel. Not surprisingly, form the figure we can see that the cell density was nearly constant after the first few hundred micrometers on the aligned scaffold (Figure 3.5d, blue line), while the cell density decreased exponentially for the flat surface and the radial migration patterns (Figure 3.5d, black line).

3.3.2. Quantitative Analysis of Cell Migration on Different PMMA Fibrous Scaffolds

The total cell migration distance traveled within 24 hours was averaged for each scaffold and plotted in Figure 3.6. Since the cells migrated radial out on PMMA thin film and random fibrous scaffold, the net migration distance of a cell from the starting point after 24 hours was measured vertically to the tangent of each point. While on the aligned PMMA scaffold, the net migration distance was measured parallel to the direction of the fibers. The total cell migration distance traveled within 24 hours was averaged for all the measured cells on the same kind of substrate and plotted as the average migration distance.

After 24 hour incubation, cells migrating on the flat substrate had covered about the same distance as those traveling on the aligned 8 μm diameter fibers. On the other hand, those traveling on the randomly oriented fibers had covered significantly less distance. In particular, the shortest distance, was traveled by the cells on the randomly oriented 8 μm fibers, followed by cells on the random fibers with fiber diameter of 200 nm. The migration distance of cells on aligned fibrous scaffold with fiber diameter of 8 μm was approximately 1.5 times larger than the distance traveled by cells on the random PMMA fibrous scaffold with the same fiber diameter. This can possibly be explained in terms of the orientation that is imposed on cells once they become attached to fibers greater than 1 μm. On the random matrix (Figure 3.4d), we can see that each cell trajectory has a different number of junctions (the number of junctions will also be a function of fiber density), which may result in a smaller cell translocation, since the cells are constrained to follow the direction of the fibers and therefore they may change directions in a typical trajectory. As can be seen from Figure 3.3, cells on the 200 nm fibers can not orient themselves along the fiber direction. Hence they are not affected by the continual change in direction.

Average speed of en masse cell migration was measured using time-lapse imaging and MetaMorph® software. Two types of measurements were performed: separate samples were incubated for 6, 16, and 24 hours and the en masse migration was measured in each sample; we also observed the same sample after 6, 16 and 24 hours. The velocity and

migration distances measured in both manners were comparable, indicating that the cells were not adversely affected by the measurement conditions.

In order to measure this velocity reproducibly, we chose to focus on cells at the leading edge of the corona, since it was easier to determine their position. The average cell migration speed, of the fibroblasts at the leading edge of the corona formed on different substrates, is plotted as a function of incubation time in Figure 3.7a and 3.7b. From the figures we can see that on the flat film surface (Figure 3.7a, black line), the migration velocity decreased exponentially with incubation time. In Figure 3.7c (black line) we plotted the cell density in the region where the migration velocity was monitored, and we can see a similar exponential decease. Since observation times chosen here were less than the cell doubling times, the decrease in cell density could simply be modeled by assuming a radial migration profile. We also compared the result with the single cell velocity measured on a flat Fn-coated tissue culture plate (TCP) surface (M.H. Rafailovich, unpublished), where we can see that the en masse velocity reached the single cell value asymptotically. Hence on the flat surface the cells migrate rapidly along radii emanating from the center, as they try to move away from each other. Once they have separated sufficiently far away from each other, their migration is determined by other properties, such as cell substrate interactions.

In order to measure the effect of the fibers more precisely, we also measured the migration velocity on oriented fibers of the same diameter and spacing of 10 μm between fibers (Figure 3.7a, blue line). From the figure we can see that the eventhough the migration velocity could now be measured with higher precision, we found that it remained constant in time and of the same magnitude as that of the single cell, or the asymptotic value reached by the cells on the Fn-coated flat surface. In Figure 3.7c (blue line) we plotted the density of the cells in the leading edge as a function of migration time, and here we can clearly see that the density remained unchanged. Hence the cells emanating from the agarose droplet on the aligned fibers follow flow patterns similar to fluid streamlines where the current though a fixed area is conserved, as opposed to the cells migrating in an expanding radial pattern with exponentially decreasing flux.

Cells plated on the 200 nm substrate (Figure 3.7b, red line), however, had a qualitatively similar behavior to cells on the flat thin film, except that the initial velocity

when they came out of the drop was much smaller, and the decrease with cell density was also much lower (Figure 3.7d, red line). In contrast to the published results [65], here the morphology is not altered with the fibril substrate, but the migration velocity is decreased in agreement with decreased migration distance.

Despite the relatively large error bars, we can see that the migration velocity of the cells on the 8 μm thick random fibers (Figure 3.7b, green line) was also much lower than that on the flat surface. Furthermore, the average velocity remained constant in time. In Figure 3.7d (green line) we plotted the cell density at the leading edge of the corona as a function of incubation time, as we did for the flat surface. The density was constant in time within the precision of the measurement. On this substrate the cells were highly polarized, but the configuration, as well as the trajectory of individual cells was only determined by the position of the fibers. Hence their density was a function of that of the fiber mat, which was uniform and unchanged in time. The statistical errors on this sample were rather large, since the actual trajectory traveled by an individual cell was difficult to determine. Rather than moved radically outward, as on the flat surface, these cells followed the curved paths determined by the underlying fiber morphologies.

Following this analogy we could attempt to quantify the degree of streamlining with which the cells migrated on the different surfaces by measuring the mean persistence. In this case, the analogy to turbulence would result in a large s.d. on the measurements, which would indicate cells moving in many disparate directions. The results are plotted in Figure 3.7e where we show the persistence of fibroblasts migrating on different substrates. From the figure we can see that on the flat surface (Figure 3.7e, black line) the average persistence increases with incubation time. Hence when the cells migrate out from the agarose droplet there was much disorder till the radial migration pattern was established and the persistence was seen to increase. A better indicator of the disorder is the large s.d., which is indicative of the many paths the cells initially follow. In the case of the fibrous substrates with fiber diameter of 8 μm (Figure 3.7e, blue and green line), we have shown previously, the cell migrated out from the droplet along the fibers. In this case the number of pathways available was determined by time independent factors, such as the fiber density, and their persistence was determined by the number of random orientations. Hence the persistence and s.d. reflect the variation in pathways of the random fibers,

rather than a dynamic process, self correcting process determined by the cells. The intermediate situation occurred when the cells were migrating out outward from the nanofiber substrate. In this case, we have previously shown that the fiber diameters are too small to affect the cell morphology and the cells do not follow any particular path. From Figure 3.7e (red line) we can see that the persistence slightly increased.

3.3.3. Localization of F-actin and Vinculin

Cell-substratum adhesion is an important parameter in the determination of cell speed. Stationary cells tend to form focal contacts that prevent movement, whereas mobile cells usually do not form a highly adhesive bond with a substrate [83-85]. During migration, cells must establish dynamic and highly regulated adhesive interactions with the ECM. In order to determine whether the differences in migration speed for the dermal fibroblasts is related to differences in the distribution of focal adhesion points, we stained the cells for vinculin (green), and F-actin (red).

After 6 hours of incubation (Figure 3.8a), for cells on the Fn-coated PMMA flat thin film, most of the cells were still inside the agarose droplet. On the periphery of the droplet, the cells that had emerged (Figure 3.8b) showed very clearly stained focal adhesion points which were localized towards the edge of the cells and upon which the actin fibrils were anchored. In Figure 3.8c we show the image 18 hours later, after which most cells had migrated out from the agrose droplet. In this image, the focal adhesion points had formed much more distinctly at the edge of the cells. It is interesting to note that in this image the focal adhesions were clustered into small cylinders, approximately, 3.5 μm long and 1 μm in diameter. For most cells the focal adhesion points were clustered at the front and rear edges of the cells. Within a given cell (Figure 3.8d), the focal adhesion and actin fibers seemed to be oriented in the same direction as migration pathway of the cell, or in this case, radically outwards.

In Figure 3.9 we show the stained cell incubated for 6 and 24 hours on the randomly oriented 200 nm fiber scaffolds. Eventhough the morphology of the cells appeared the same as on the flat surface, the pattern of vinculin and actin was very different. At 6 hours (Figure 3.9a, b), thin focal adhesion sites were visible at the tips of individual actin fiber bundles. In Figure 3.9c we see the cells after incubating for 24 hours. In contrast to the

cells on the flat surface, which had well defined cytoplasm boundaries, these cells appeared to have many very thin filopodia emanating from the edge. The most striking difference though was the appearance of the individual cells (Figure 3.9d). The cells had very well formed F-actin fibrils which could clearly be seen together with the underlying fiber scaffold. Instead of forming the usual cylindrical focal adhesion points at the terminus of the actin fibers, the vinculin was now clustered in a diffuse and rather large region towards the front sections of the cells. Small filopodia were seen emanating from underneath the cloud. The cells were clearly trying, but obviously not successfully, to follow the nanoscale underlying patterns.

In Figure 3.10 we show the cells plated on the oriented 8 μm diameter fibers. Even after 6 hours (Figure 3.10a), well formed focal adhesion cylinders were observed along the edges of the cells, and following the contour of the underlying fibers. The individual focal adhesion cylinder (Figure 3.10b) were also seen to be aligned all along a given cell in the direction of its motion and completely oriented along the underlying fiber. In Figure 3.10c we show the cells after 24 hours of incubation. Here too the pattern and distribution of the focal adhesion sites was unchanged. The unchanged focal adhesion patterns were consistent with the constant migration speed observed on these scaffolds.

3.3.4. Tightly and Loosely Aligned PMMA Fibrous Scaffold

It is known that the spacing of mechanical obstacles can affect the cell motile speed [86-88]. We therefore also varied the fiber density in the substrates. In this experiment, the chemistry, adhesiveness, and mechanical strength were purposely maintained constant so that the change in cell motility would be caused only by differences in the spacing between fibers. Substrates with an average fiber spacing of 2 (tight packing) and 25 μm (loose packing) were produced.

On the tightly packed fibrous scaffold, we found that nearly all the cells migrated out of the droplet onto the fibers. This was expected, since the flat film surface was almost entirely covered by fibers (Figure 3.11a). In Figure 3.11b we show the image obtained from cells emerging from a loosely packed fiber scaffold. In the inset we show high magnification images of the same region, where arrows point to cells that were on the fibers versus cells that were on the substrate. Eventhough on this scaffold, there was

ample exposed area of the flat substrate, 85% of the cells still emerged from the droplet directly onto the fibers, clearly indicating that the cells preferred the fibrillar surface. No obvious difference of the cell morphology was found between these two substrates. Clearly fewer cells were migrating out of the droplet on the lower density surface. The ratio of the total number cells migrating outward from the tight packed substrate and the loose packed substrate was about 1.6:1. Comparing the migration velocity and distance migrated between the substrates showed only insignificant diffidence (data not shown).

In Figure 3.11c and Figure 3.11d we show the same images where the nucleus of the cells in Figure 3.11a and Figure 3.11b were stained, and where we can see the patterns emerged in the direction perpendicular to the fibers. From the marked patterns we can see that the cells arranged themselves such that there was also minimal overlap between adjacent cells. In Figure 3.12 we show a SEM image of the cells that were fixed and dried on the fibers. From Figure 3.12a we can see that eventhough most of the cytoplasm of the cell was centered on one fiber, a large number of filopodia extend out to the neighboring fiber. In this manner the cells could sense the cell density in their environment. In contrast to the flat surface, the cells here were constrained to move on the fibers and could not choose a radial pathway which would decrease the local density. The only mechanism for decreasing overlap on this substrate was to occupy alternating positions on the fiber. This then produces patterns such as the ones shown in Figure 3.11c that has a "wavy" appearance. Much less patterned arrangement was found in the loosely packed fibers, which was shown in Figure 3.11d.

3.3.5. Cell Migration from the Film Surface onto the Fibers

When the agarose droplet is placed on the fiber surface, the flat film surface may not be in direct contact with the cells, and hence the fact that more cells migrate on the fiber is not complete confirmation of cell preference. In order to directly probe whether the cells prefer the fibrillar to the flat surface, we also placed the droplet directly on the spun cast film and placed an electrospun scaffold besides the droplet edge. The sample was then imaged after 48 hours incubation (Figure 3.13a). Comparing the corona of cells emanating from the droplet at the front and rear edges, we can approximately see that the migration distances were similar, between the flat and fibrous surfaces. In Figure 3.13b

we show a magnified view of the area designated in blue box. Some cells began to migrate on the flat surface when the fibers were far apart, but eventually “climbed” onto the fibers, such that at further distances all the cells were collected onto the fibers.

Cell migration on the cross-aligned scaffolds

A true 3D scaffold consists of alternating layers of fibers. In an oriented scaffold, each layer is rotated by a fixed angle relative to the adjacent layers. The cell migration results on cross-aligned scaffold (inset) are shown in the sequence of images in Figure 3.14 (a-e) which were obtained from a video made of the migration cells. From the images it is easy to see on which layer the cells are migrating simply from their orientation. We were therefore able to measure the migration velocity of cells which moved from one fiber onto another within the hour of observation. In all cases observed here, cells only changed onto fibers where a 90º rotation was presented. Hence cells moved from one layer to the next only through following the fiber contours. From the images we were able to determine that when cells changed directions, their velocities decreased roughly by approximately 33% (±3.84%) in the process (Figure 3.14f).

Since the droplet penetrated all layers in the cross-aligned scaffold, it was difficult to determine the fraction of the cells migrated between layers. In order to determine this rate, we produced the construct shown in the illustration in Figure 3.15a. Here the agarose droplet loaded with cells was placed on a layer of parallel fibers (bottom layers, defined as “perpendicular direction”). Another layer of fibers was spun at 90º (upper layer, defined as “parallel direction”) to the first a distance of 600 μm away, as shown. The system was then incubated for 72 hours (to make sure there were enough cells on the upper layer), stained with PI and imaged as shown in Figure 3.15b. The number of cells on each layer in the region 1 was then counted. In this region, cells with the “perpendicular orientation” could only migrate onto that layer from the upper layer, which was not in contact with the droplet. From the figure we find that the ratio of cells on the bottom to upper layers is no larger than 10%. Therefore the migration of cells in three dimensions is a combination of motions following surfaces, where at each junction a change in direction has a lower probability than following a straight path, and may be associated with reduced migration speed.

3.4. Conclusion

Based on the results obtained thus far, cells can send filopodia to sense their environment within a region of several tens of microns both in 2D (Figure 3.12a) and 3D (Figure 3.12b) scaffold. When the cells migrated on the 2D aligned scaffold, long ranged correlations are established between cells on adjacent cells, leading to the formation of sinusoidal pattern, as the cells readjust to minimize the local cell density. When the cells migrated on the 3D cross-aligned fibers, cells will not "flow" and migrate through the spaces between the fibers. Rather, cells will adhere to the fibers; either remain on a straight course or follow the fiber on the layer above or below. The decision on which pathway to take may depend on the ability of the cell to distort, the presence of other cells near the junction, and the interactions of cells on the same fiber. Hence migration becomes predominantly a function of the morphology of the fibers, cell/fiber affinity, and local cell density. The size of the pores becomes a negligible factor if minimal size (cell diameter) is obtained.

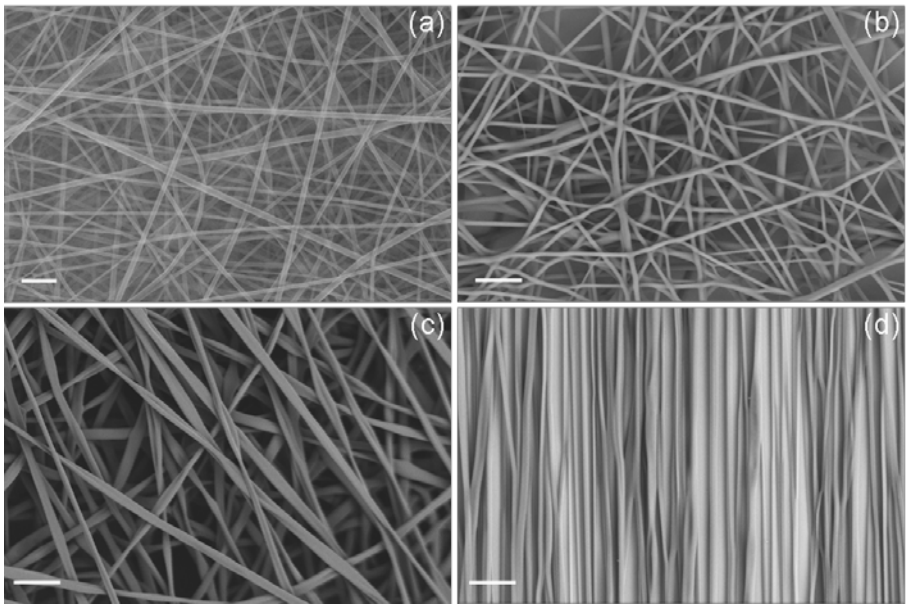

Figure 3.1. SEM images of random PMMA fibers with fiber diameter of (a) 200 nm, (b) 1 μm, (c) 8 μm, and (d) aligned PMMA fibers with fiber diameter of 8 μm.
Bars, 1 μm (a), 40 μm (b, c, d)

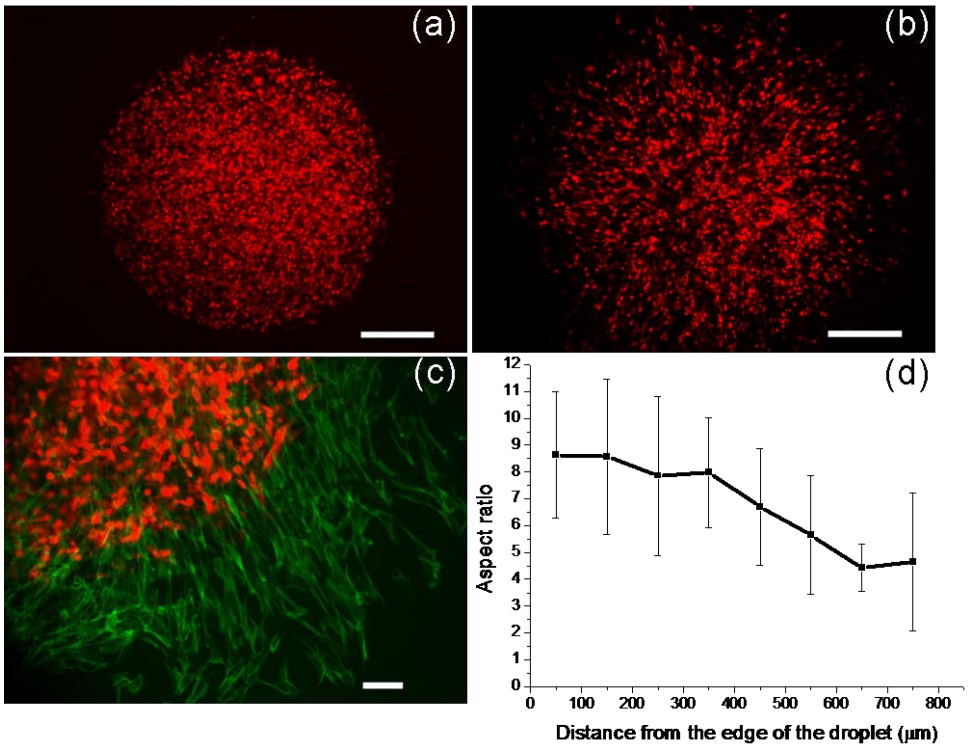

Figure 3.2. Fluorescence microscope images of live cells, stained with DiD (red), migrating out of agarose droplets deposited on a Fn-coated PMMA film and incubated for: (a) 4 hours and (b) 24 hours. (c) The overlapped image of the live cells shown in (a) onto the image of the cells incubated for 24 hours, fixed and stained for F-actin with Alexa Fluor (green), where the edge of the droplet is clearly marked. (d) Aspect ratio of the cells incubated for 24 hours plotted as a function of the distance from the edge of the agarose droplet.

Each date represents Mean±s.d. of the results from 30 cells and the data was repeated 4 times. Bars, 0.5 mm (a, b), 100 μm (c).

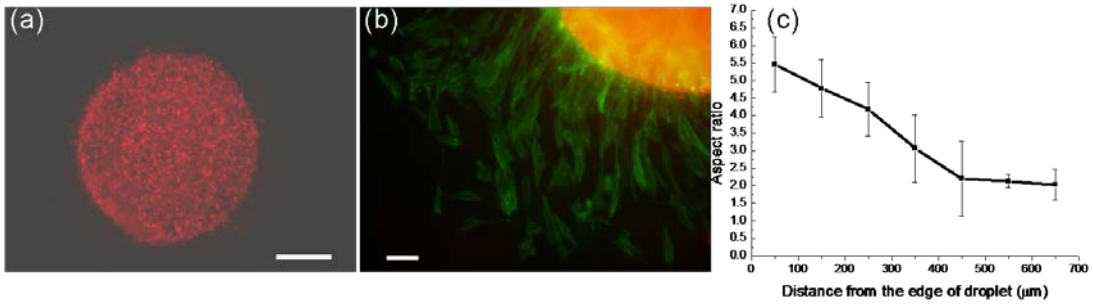

Figure 3.3. (a) The fluorescence microscope image of live cells stained with DiD (red) migrating out of agarose droplet deposited on Fn-coated random PMMA 200 nm fibers for 24 hours. (b) The image was obtained by overlapping the image of live cells incubated for 4 hours and the image of the cells incubated for 24 hours, fixed and stained for F-actin with Alexa Fluor in order to visualize the edge of the droplet. (c) Mean values (±s.d.) of the aspect ratio as a function of the distance from the edge of the agarose droplet shown in (b).
Each data represent the average of 30 cells and the data was repeated 4 times. Bars, 0.5 mm (a), 100 μm (b)

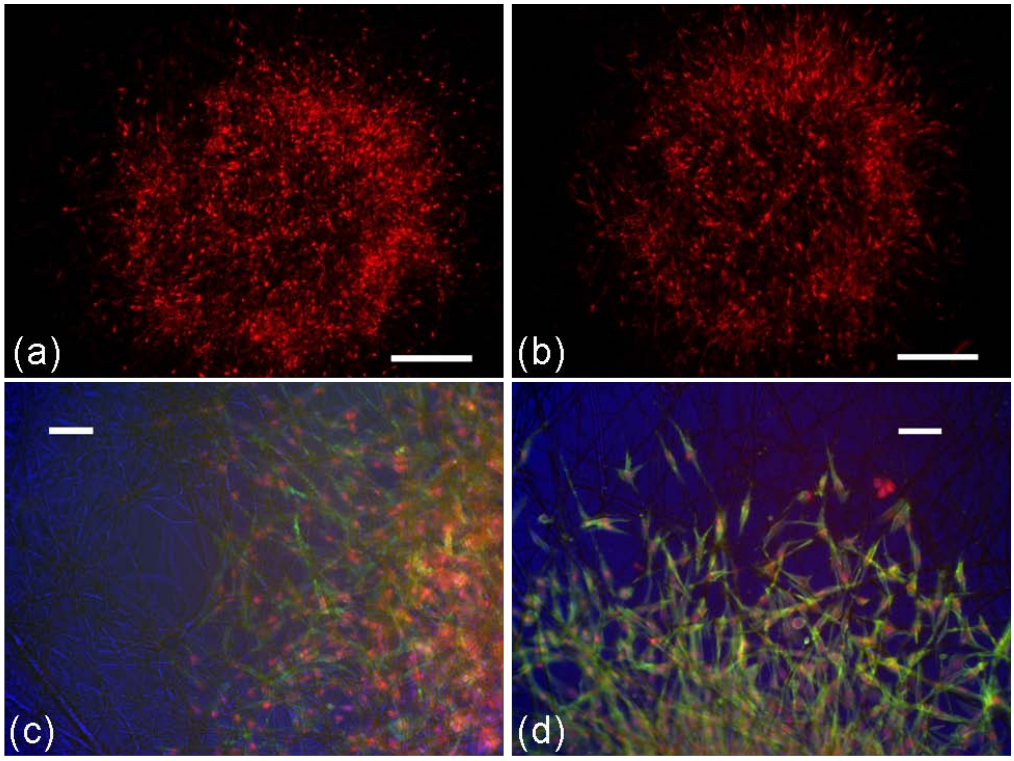

Figure 3.4. Fluorescence microscope images of live cells stained with DiD (red) migrating out of agarose droplets, deposited on random PMMA fibrous scaffolds in diameter of (a) 1 μm and (b) 8 μm after 24 hours of incubation. Images of cells fixed and stained with DAPI and Alexa Fluor after migrating for 24 hours on PMMA random fibers (c) 8 and (d) 1 μm in diameter.
Bars, 0.5 mm (a, b), 100 μm (c, d).

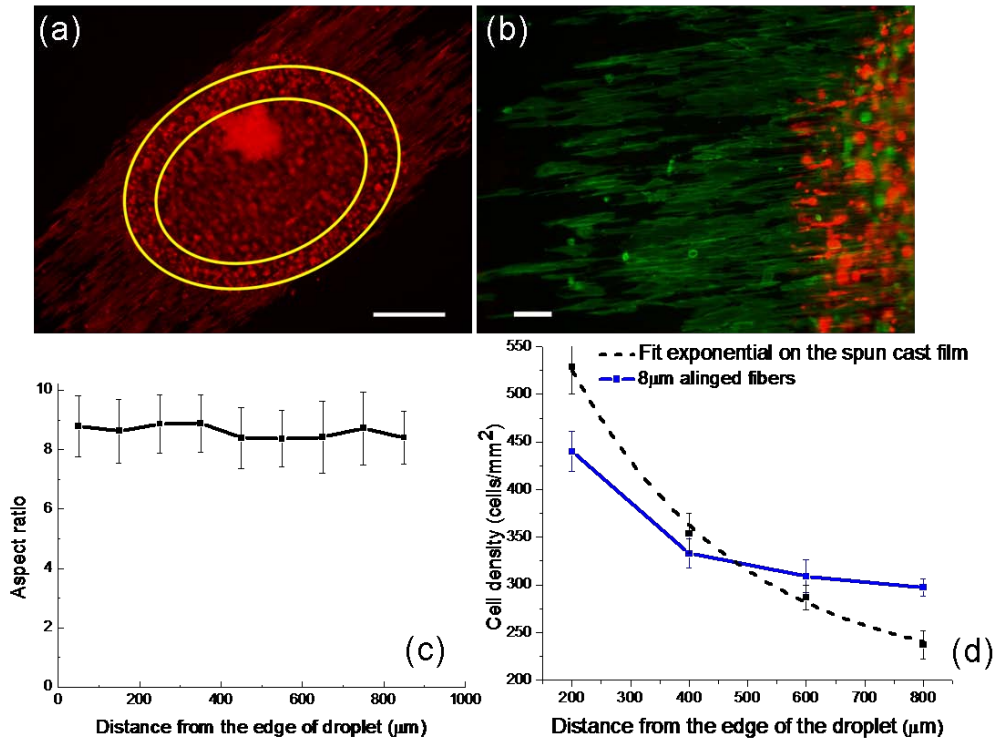

Figure 3.5. (a) The fluorescence microscope image of live cells, stained with DiD (red), migrating out of agarose droplets deposited on aligned PMMA fibers in diameter of 8 μm and incubated for 24 hours. (b) The overlapped image of the live cells incubated for 4 hours onto the image of the cells incubated for 24 hours, fixed and stained with Alexa Fluor (green). (c) Cell aspect ratio and (d) cell density were measured after 24 hours incubation and plotted against the distance from the edge of the agarose droplet.
Bars, 0.5 mm (a), 100 μm (b).

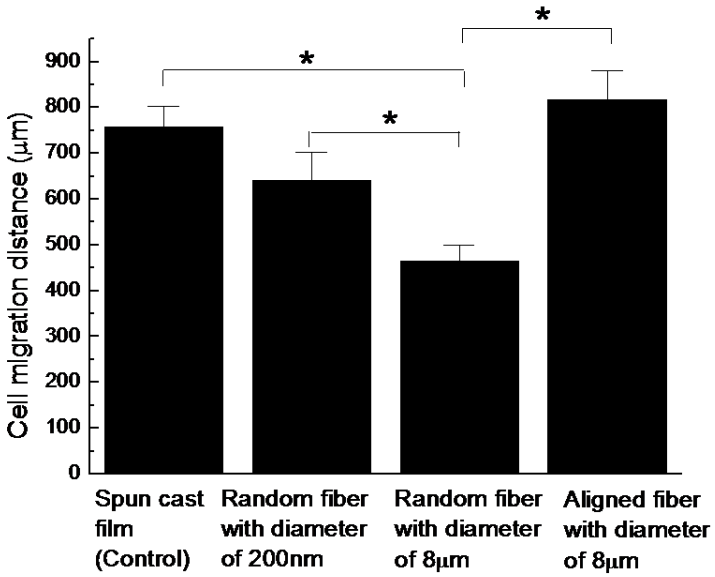

Figure 3.6. The migration distance, as measured from the leading edge of the agarose droplet, for cells which were incubated for 24 hours on different substrates.
The error bars represents the s.d. of the mean of 10 measurements per sample, with 3 duplicates and repeated 4 times. *$p<0.05$.

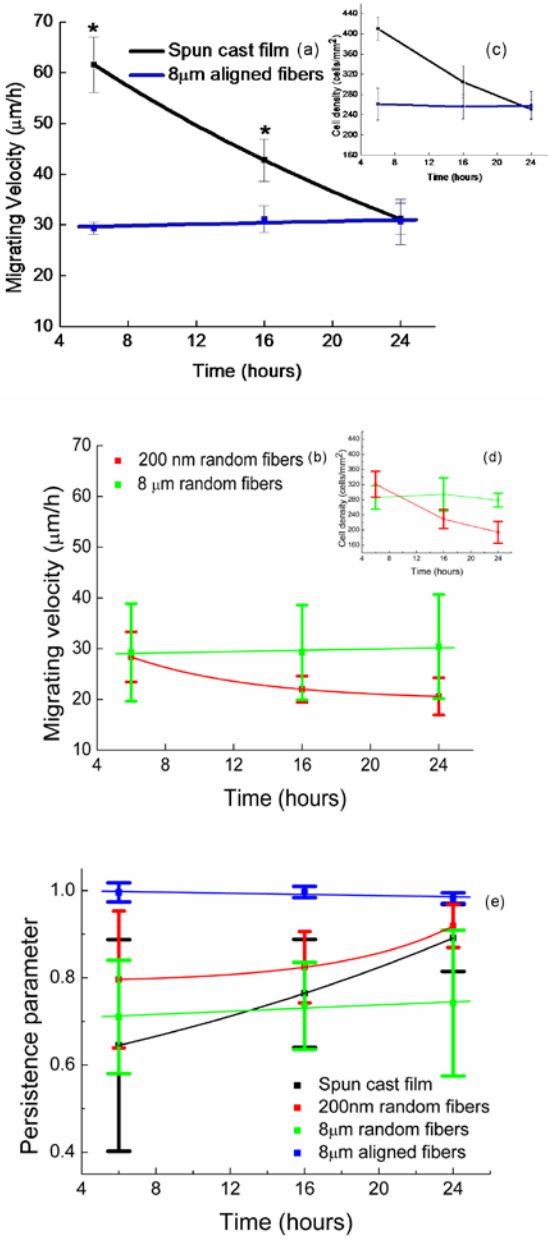

Figure 3.7. (a, b) Migration velocity and (c, d) cell density plotted as a function of incubation time. (e) Persistence parameter defined as the total cell translocation/ total length of cell path the substrates studies.
Each measurement represents the average and standard deviation for 20 cells, with 3 duplicates and the entire curve was repeated at least 4 times. *$p<0.05$.

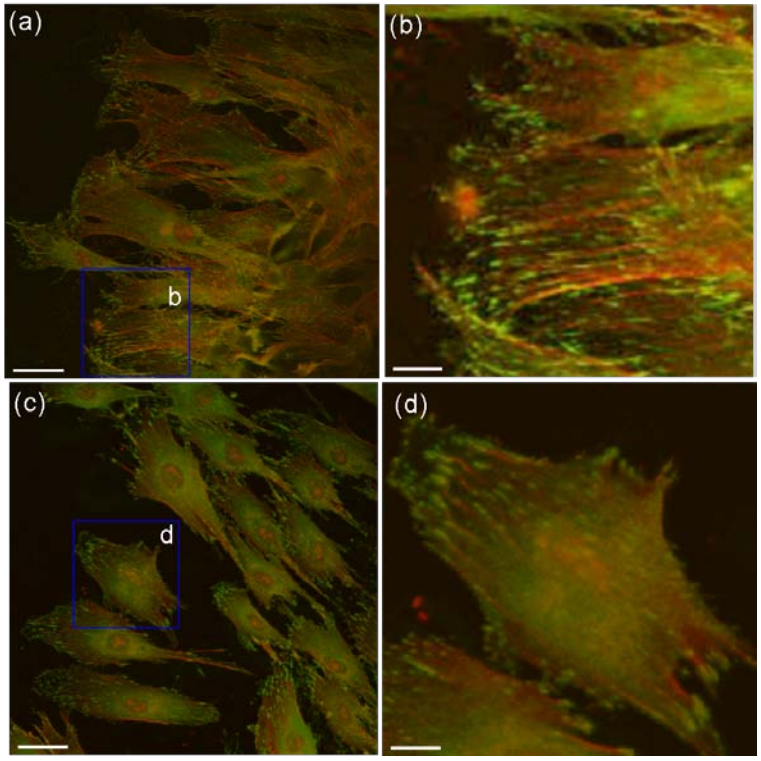

Figure 3.8. Double immunostaining of F-actin (red) and vinculin (green spots) distribution in human dermal fibroblasts plated on Fn-coated PMMA spun cast film after (a, b) 6 hours and (c, d) 24 hours in culture.
Higher magnification images where the vinculin stained loci are more visible corresponding to the area marked in the square. Bars, 20 μm (a, c), 6 μm (b, d).

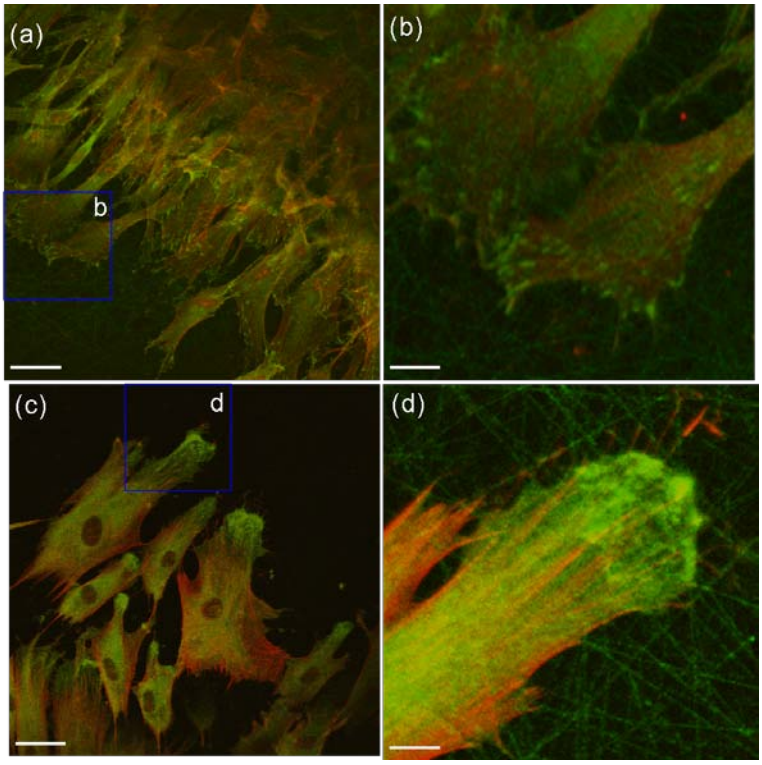

Figure 3.9. Double immunostaining of F-actin (red) and vinculin (green spots) distribution in human dermal fibroblasts plated on Fn-coated PMMA random fibers, 200 nm in diameter (a, b) 6 hours and (c, d) 24 hours in culture.
Bars, 20 μm (a, c), 6 μm (b, d).

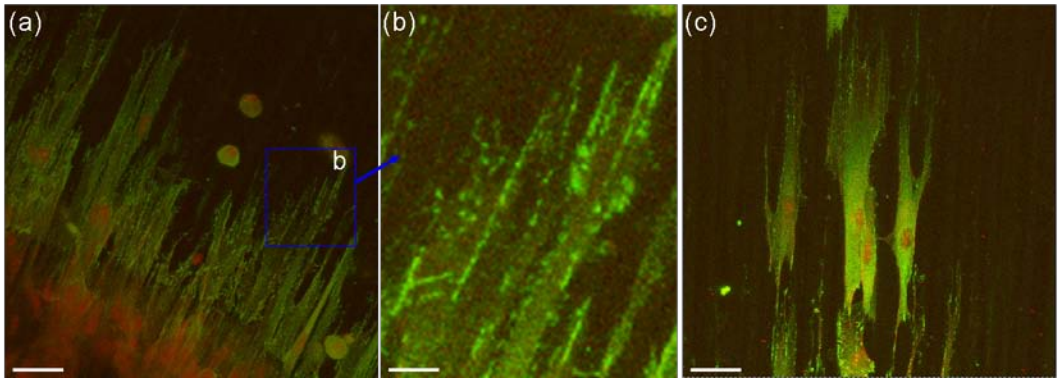

Figure 3.10. Double immunostaining of F-actin (red) and vinculin (green spots) distribution in human dermal fibroblasts plated on Fn-coated PMMA aligned fibers with diameter of 8 μm (a, b) 6 hours and (c) 24 hours in culture.
Bars, 20 μm (a), 6 μm b), 20 μm (c).

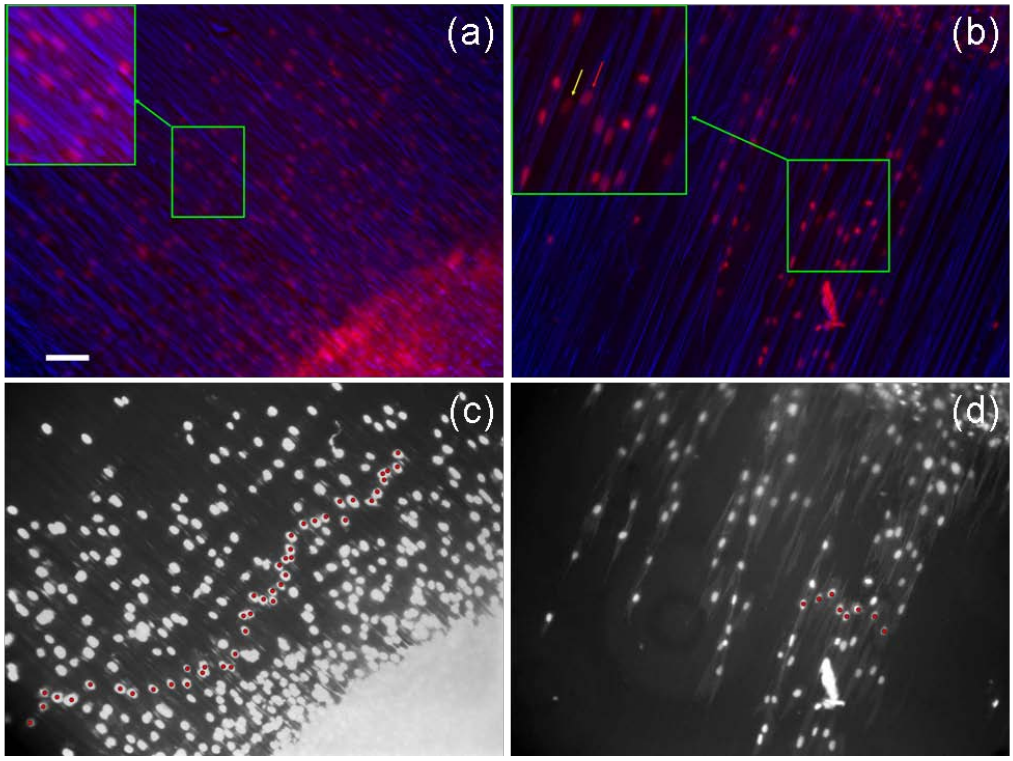

Figure 3.11. Fluorescence microscope images of cells, stained with DAPI, overlapped onto phase contrast images of the fibrous scaffolds, upon which the cells have migrated for 24 hours: (a) tightly packed scaffold and (b) loosely packed scaffold. High contrast fluorescence microscope images of cells (stained with DAPI) migrating in regions where the correlations between adjacent cells is more visible and the patterns are highlighted on (c) high density scaffolds and (d) low density scaffolds.
Tightly packed PMMA fibrous scaffolds were prepared by electrospinning for 60 minutes, while the loosely packed PMMA fibrous scaffolds were prepared by electrospinning for 10 minutes. All the images were taken under the same magnification and the bar in (a) represents 100 μm.

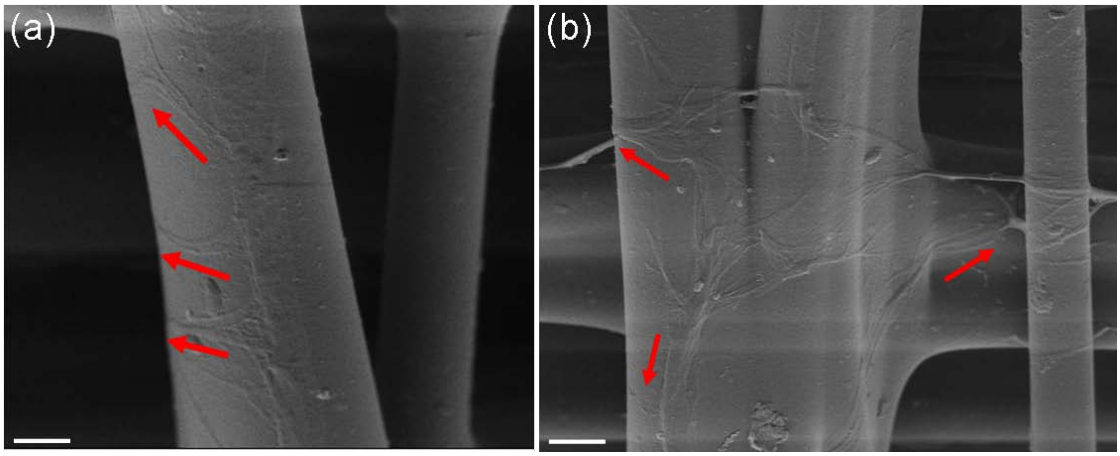

Figure 3.12. Cells migrating on different types of scaffolds which were prepared according to the text for SEM imaging. Note the filopodia (arrows) which can not be seen in the confocal images, but which clearly extend between adjacent fibers of (a) tight packed single layer scaffold and (b) tightly packed double layer scaffold.
Bars, 20 μm (a, b).

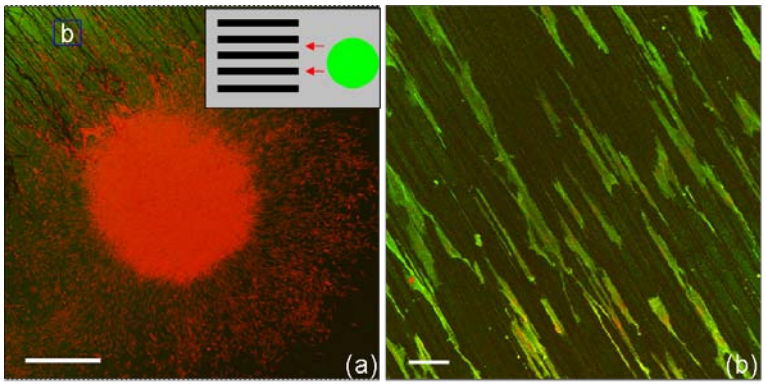

Figure 3.13. Cells migrating radically outward from a droplet placed on a flat film adjacent to an oriented scaffold composed of fibers 8 μm in diameter. The F-actin was visualized as green, and the nuclei were visualized as red in the images. The inserted image in (a) shows the model of the substrate.
Bars, 1.5mm (a), 130 μm (b).

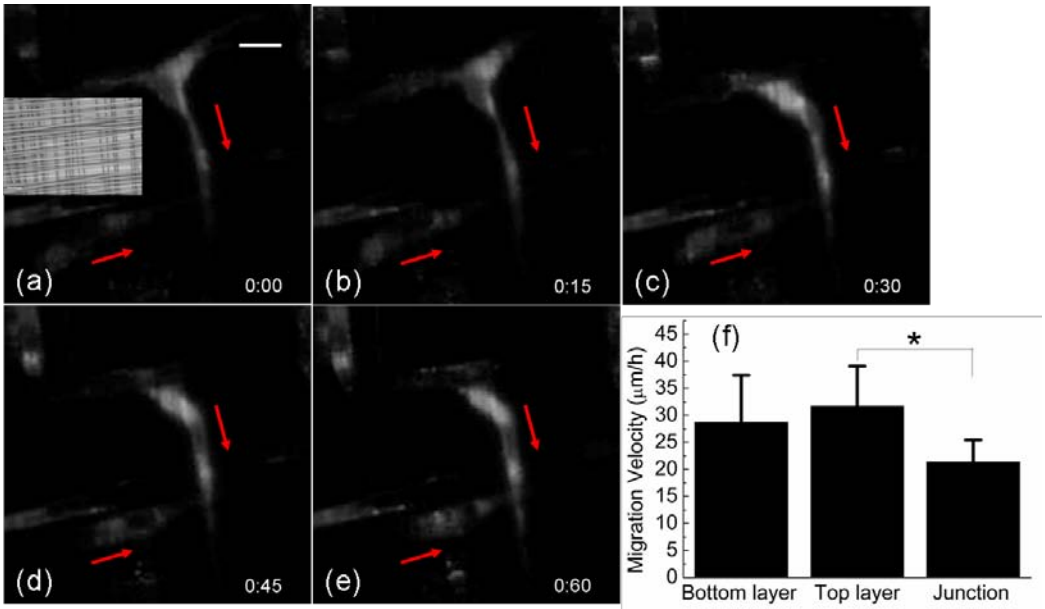

Figure 3.14. Fluorescent, time-lapse pictures of the motion of two typical fibroblast cells on the cross-aligned PMMA fibers (inset). Membrane stained cells were encapsulated in the agarose drop, plated on the PMMA cross-aligned fibers and incubated for 24 hours first. Images were taken when the cells were (a) just or after (b) 15 minutes; (c) 30 minutes; (d) 45 minutes and (e) 60 minutes out from the incubator. (f) Migration velocity of cells moving on the cross-aligned scaffold after cell culture for 24 hours.
The recorded time point was indicated the on bottom right corner. The arrowheads indicate the cell migration direction and the scale bar represents 50 μm. For (f) each measurement represents the average and standard deviation for 20 cells, with 3 duplicates and the entire curve was repeated at least 4 times.*$p<0.05$.

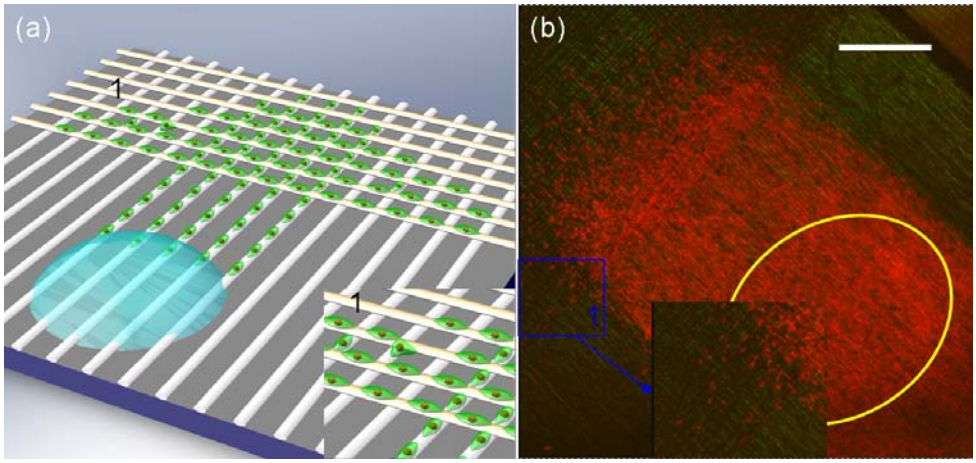

Figure 3.15. Illustration shows the structure of the scaffold designed to test cell migration between upper and bottom layers. (b) Confocal fluorescent microscope image of the cells (stained with PI) on the patterned scaffold.
Cells were encapsulated in the agarose drop, plated on the PMMA cross-aligned fibers and incubated for 72 hours before stained. The yellow circle shows the original position of the agarose droplet. Bars, 40 μm in the inserted SEM image and 500 μm in (b).

Chapter 4. Engineering of Bio-hybrid Materials by Electrospinning Polymer-Microbe Fibers

4.1. Introduction

Microorganisms most often exist in nature as biofilms; a complex and dynamic community formed via self-encapsulation in a self-developed extracellular polymeric matrix [89]. Biofilm formation is known to afford protection to microorganisms from various environmental challenges such as pH, salinity and metal toxicity [90], and resistance to antibiotics and microbicides [91]. Biofilms can be viewed as stable and efficient thin film catalytic systems [92]. Researchers are presently attempting to understand the complexity and the above-mentioned unique characteristics of biofilms, in order to create synthetic ones and exploit them for biotechnological applications in areas such as environmental remediation [93, 94], microbial fuel cells [95], particle biofilm reactors [96], and fermentation reactors [92]. The shortcomings of a traditional batch reactor, such as fermentors, include low cell density, and frequent inoculation and start-up. These drawbacks are overcome in a biofilm reactor by virtue of its high cell density and stability. An ideal biofilm would be continuously used or reused, just as a thin-film catalyst. Further, the development and use of a synthetic biofilm is desired as it allows for industrial-scale production and reproducibility. This study represents a significant step towards achieving that goal, as we report the generation of a very thin polymeric fibrous material in which microbes act as functionally active sites.

The formation of composite microbiological material or biohybrid material containing entire microbial cells as catalytic centers has been pursued for several decades [97]. In almost all these studies, microorganisms were entrapped in polymeric (typically polyacrylamide or silica), inorganic spheres that were orders of magnitude larger than thin films [98, 99]. Thus, they suffered from shortcomings such as low viability of

microbes, low diffusion through the material, and subsequent loss of biological activity [100]. We have overcome these shortcomings via the development of thin fibrous materials using the process of electrospinning. These materials, while immobilizing microorganisms, are also shown to act as functional materials and thus form a hybrid between immobilization and biofilms.

Previous studies have reported the encapsulation of biological molecules, such as enzymes, proteins or animal cells in polymer fibers by co-electrospinning [101-105]. In this process, two different solutions are spun simultaneously using a spinneret with two coaxial capillaries, to produce core/shell fibers. For the application of encapsulated live microbes, however, there are at least two problems to be solved: (i) the organic solvent of the outer layer of the fibers has to be completely evaporated to decrease the toxicity to the microbes inside the polymer fibers, and (ii) the porosity of the outer layers of the fiber has to be increased to facilitate the transfer of material between the microbe and its environment. The above problems can be addressed by using polyethylene oxide (PEO)-blend hydrogels, as explained below.

Hydrogels are mechanically soft and flexible in aqueous solution that are capable of hosting enzymes without deteriorating their biological function [106, 107]. The capability of making nano- and microfibers from water-soluble polymers by electrospinning offers one way to create hydrogels with nano- and micro-structures. If these mechanical and biocompatible properties are combined with the advantages of high surface-to-volume ratios of fibers, the hydrogel can be used as an efficient support material not only for enzymes but also for immobilization of microorganisms [108]. Seung-Wuk Lee [109], Salalha [110], and Gensheimer [111] had investigated electrospinning as a possible method of encapsulation both bacteria and bacterial viruses. While these studies are of great value and showed the promise of this emerging field, the electrospun poly (vinyl alcohol) (PVA), poly (ethylene oxide) (PEO) and polyvinyl pyrrolidone (PVP) materials were water soluble and thus significantly limited in their use. Furthermore, the microorganisms that were used in those studies with the exception of *Escherichia coli (E. coli)* are of minor relevance to the industry. For example *Micrococcus luteus* was specifically selected to survive the dry conditions of their electrospinning process.

We have created, for the first time, an insoluble fibrous polymeric material, the fibers

of which encapsulate industrially relevant bacteria via electrospinning of Pluronic F127 dimethacrylate (FDMA or PEO_{99}-PPO_{67}-PEO_{99} DMA). FDMA was selected as a model membrane material due to its non biodegradability, and non-toxicity, albeit non adhesion to cells. Moreover, it has already demonstrated significant ability to preserve polypeptide bioactivity, enzyme stability, and protein drug delivery [112]. During electrospinning, the fibers overlap with each other in a completely random manner, giving rise to the open pore structure ideal for use as electrodes, membranes and in filtration. Our aim was to elucidate the conditions of the electrospinning and cross-linking process that allow the encapsulation of intact bacteria while still maintaining their viability. The microorganisms utilized in this work were *Pseudomonas fluorescens* (*P. fluorescens*), *Zymomonas mobilis* (*Z. mobilis*) and *E. coli*. All of them are rod shaped bacteria. These species were chosen as examples of industrially relevant genera. For example, *Z. mobilis* is one of the most efficient fermentors known to produce ethanol from glucose [113-115]. This work opens up an avenue for exploring the use of electrospun fibers for more mainstream application in the separation technology as well as in biofilm reactors.

4.2. Experimental Section

4.2.1. Synthesis of FDMA

The synthesis and characterization of FDMA was described in an early article and the chemical reaction is shown in Figure 4.1 [116]. The weight average (M_w) and number average molecular weight (M_n) of FDMA was determined using calibrated gel-permeation chromatography (GPC) to be $M_w = 21{,}900\ Da$ and $M_n = 12{,}600\ Da$ ($M_w/M_n = 1.3$).

4.2.2. Bacterial Cultures

P. fluorescens (ATCC 55241) were cultured in a medium, containing citric acid, 2.0 g/L; $MgSO_4.7H_2O$, 0.2 g/L; NH_4Cl, 1.0 g/L; KH_2PO_4, 1.0 g/L; K_2HPO_4, 1.0 g/L; NaCl, 5.0 g/L; pH 6.1 adjusted using NaOH. *Z. mobilis* (ATCC 31821) were cultured in a medium containing glucose, 20 g/L; yeast extract, 10 g/L; KH_2PO_4, 2 g/L, pH adjusted to 6.0 using NaOH. Functionality was assessed by growing immobilized *Z. mobilis* and pure culture (control) in a fermentation medium containing 20 g glucose, 10 g yeast extract, and 2 g KH_2PO_4 per L H_2O; pH 6.0. Recombinant *E. coli* bacteria expressing green fluorescent protein (GFP) was grown in Luria-Bertani (LB) medium. The cultures were grown in Erlenmeyer flasks in an incubator at 27 ± 1°C. Typically, cultures at the end of the log phase of growth were used for electrospinning.

4.2.3. Fabrication of FDMA/PEO Blend Fiber

An aqueous solution of FDMA is not optimal for electrospinning into fibers, even at high concentrations. Therefore, PEO ($M_w = 900\ kDa$, Sigma-Aldrich Inc.) was blended with FDMA to facilitate the fiber formation during the electrospinning process. To prepare the electrospinning solution, PEO powder was dissolved in deionized water at the following concentrations: 1 wt%, 2 wt% and 3 wt%. FDMA powder was then added into the PEO solution at a concentration of 13 wt% and allowed to dissolve for several hours at 4°C until the solution became clear. For encapsulation experiment, pre-determined

amount of the bacteria, as required, were dispersed homogenously in the FDMA/PEO solution before electrospinning.

The experimental set-up of the electrospinning stage was described elsewhere [117]. The fibers were electrospun and collected on a sterile Si wafer for about 30 minutes to form a three-dimensional (3D) structure.

4.2.4. Cross-linking of the Electrospun FDMA Matrix

The catalytic system consists of ascorbic acid (AsA, Aldrich), ferrous sulfate (Aldrich), and ammonium persulfate, (APS, Aldrich). The principle of this reaction is similar to Fenton reaction, as reported earlier [118]. APS is the free radical initiator, ferrous sulfate and AsA are used to catalyze the breakdown of the APS and, therefore, to accelerate the cross-linking reaction. This catalytic system is effective at room temperature even if the concentration of the initiator is very low. However, for the system to be highly efficient, the ratio of the APS, AsA and ferrous sulfate had to be fine tuned.

AsA, APS and ferrous sulfate solution were prepared freshly in deionized water and pre-determined amounts of those solutions were then added to the glycerol/deionized water solvent at differing glycerol: water ratios The electrospun fibers (along with the Si wafer support) were placed into a glass vial containing 2 ml of the cross-linking solution and allowed stand overnight at room temperature. The cross-linked membrane was then washed three times with deionized water to remove unreacted monomers, and catalyst. Finally, the membrane was soaked in deionized water for 24 hours to ensure complete extraction of the PEO and fully swell the scaffold.

4.2.5. Characterization of Electrospun FDMA Fiber Mats

The surface morphology of the electrospun FDMA/PEO blend fibers and FDMA fibers (with and without bacteria) were characterized using scanning electron microscopy (SEM) (LEO 1550, LEO, Germany). The swollen FDMA fibers were freeze dried (Consol 1.5, Virtis Inc. NY) at -40°C, followed by lyophilization. Samples were sputter-coated with gold for 15 seconds twice prior to SEM imaging. The fiber diameter distributions of the FDMA/PEO blend scaffolds and cross-linked FDMA scaffolds were calculated by

analyzing the SEM images using Image Tool (The University of Texas Health Science Center in San Antonio) in a manner similar to that described by Boland ED *et al*. did [119].

Thermogravimetric (TG) measurements were conducted to analyze the thermal behavior of the electrospun FDMA/PEO blend fibers, prior to and following cross-linking. TG measurements were conducted in nitrogen gas at a heating rate of 5°C/min in the temperature range between 50°C and 500°C using a Mettler Toledo TGA/SDTA 851 thermal analyzer. Samples with a weight of approximately 15 mg were loaded in a SiO_2 crucible under dry conditions.

4.2.6. Characterization of Microbes

The viability of the microbes was assessed using the LIVE/DEAD® BacLight™ bacterial viability kits (Molecular Probes, OR). Live microbes (intact cell membranes) stain fluorescent green, while dead microbes (damaged cell membranes) stain fluorescent red. Live and dead bacteria were later viewed simultaneously by Leica TCS SP2 laser scanning confocal microscopy (LSCM) (Leica Microsystem Inc., Bannockburn, IL).

The morphologies of the bacteria inside the FDMA/PEO fibers were characterized both by LSCM and SEM. For LSCM, bacteria were spun down from culture media, stained with bacterial viability kits, and then mixed with the FDMA/PEO solution, prior to electrospinning. While for GFP *E. coli*, GFP was excited at 488 nm with an argon ion laser source without any staining. For SEM studies, the bacteria were rinsed with deionized water twice, stained with 2% (w/v) uranyl acetate for 2 minutes at room temperature, spun down and mixed with the FDMA/PEO electrospinning solution. To image the bacteria inside the cross-linked FDMA fiber by SEM, the swollen fibers were freeze dried and coated with gold as described above.

4.2.7. Cytotoxicity and Storage Evaluation

The viability of the bacteria, before and after electrospinning, was evaluated after various times of electrospinning. Bacteria containing fibers were stored under the exclusion of light at 4°C for up to 7 days and at -70°C for up to 2 months. Two methods

were used to analyze the bacterial survival rate. The encapsulated microbes were stained with LIVE/DEAD® BacLight bacterial viability kits immediately after they were liberated from the FDMA/PEO blend fibers and then observed under LSCM. Photomicrographs of the stained bacteria were obtained. The number of bacteria alive was averaged over several views of the same condition. Bacterium counting at each time point was performed in triplicates. In the case of *Z. mobilis*, the uncross-linked fibers were dissolved in sterile bacteria culture media and/or fermentation media described earlier, whereby the immobilized microorganisms were released from the fibers. As controls, free culture and microorganisms mixed with polymeric material (prior to electrospinning) were used as inoculums. After incubation, the metabolic activity of the *Z. mobilis* was tested by analyzing the spent media for residual glucose and ethanol concentration using high performance liquid chromatography (HPLC). The cytotoxicity of the chemicals and the cross-linking process to the bacteria were also evaluated using the LIVE/DEAD® BacLight ^{TM} bacterial viability kits as explained above.

4.2.8. Swelling Ratio and Nutrient Exchange Rate

To determine the swelling ratio, electrospun FDMA fibers and 13wt% FDMA polymer solutions were cross-linked, rinsed with deionized water, and dried until their weights stabilized (W_d). The dried samples were then placed in glass vial containing 10 mL of deionized water at room temperature. The wet samples were weighed (W_s) at predetermined time intervals. The swelling degree (%) was calculated from equation (1):

$$Swelling(\%) = \frac{W_s - W_d}{W_d} \times 100 \qquad (1)$$

The rate of exchange of nutrients and metabolic products from within the fiber to its environment was estimated using glucose as a sample nutrient. In these tests, 40 mg glucose was mixed homogeneously with 13wt% FDMA solutions. The polymer containing glucose was cross-linked, rinsed 3 times using deionized water and placed into a glass vial containing 10 mL of deionized water. The vial was placed in a shaker incubator at 26^{o}C, to simulate the conditions under which the organisms used in this study were cultured. Aliquots were taken at predetermined time intervals And the

concentrations of glucose was determined using HPLC.

4.3. Results and Discussion

A schematic describing the different stages of the process that were undertaken in this study to generate the biohybrid material is presented in Figure 4.2. Furthermore, the various stages at which the fibers were characterized and analyzed are also indicated on the schematic.

4.3.1. Optimization of FDMA/PEO Weight Ratio

The FDMA/PEO blend solutions with different weight ratios, increasing from 13:1 to 13:3, were electrospun to fabricate fibrous membrane scaffolds. At an FDMA/PEO weight ratio of 13:1, very few electrospun fibers were generated and they showed a beads-on-string morphology with a high beads density (Figure 4.3A). As the FDMA/PEO weight ratio increased from 13:1 to 13:3, the density of beads decreased and a uniform fibrous scaffold was obtained at an optimized weight ratio of 13:3 (Figure 4.3B, C and D), that was used in all further experiments.

4.3.2. Preparation of the Cross-linked FDMA Hydrogel Fibers

The water soluble nature of FDMA presents a great challenge as any contact with water can immediately destroy the fibrous structure and therefore highly limits the application of this polymer. Cross-linking the fibers after electrospinning will create hydrogel fibers with improved resistance to water. Such cross-linked fibers with encapsulated microorganisms can be used in various applications. However, FDMA cannot be cross-linked using conventional cross-linking approaches such as exposing the fibers to a water-based cross-linking solution [120]. Also, the non-volatile nature of the cross-linking agent prevents the use of vapor-phase cross-linking method [121-123]. Several studies have described various other methods of creating cross-linked fibers; such as heat [124-128] or ultraviolet (UV) radiation (108, 129-131) to initiate the cross-linking reaction during or after the synthesis of the fibers. Heat and UV light, however, have known microbicidal properties and thus are not suitable for use in this study.

It is preferable to cross-link FDMA fibers in an organic solvent to prevent its

dissolution. Glycerol was chosen as the organic solvent due to its low toxicity to microorganisms. In fact, glycerol is used to preserve microorganisms at -70°C. While pure glycerol can be used, it does not lead to free-radical polymerization. In order to initiate free-radical polymerization, the fibers were exposed to a solution of glycerol and water containing a redox system consisting of ammonium persulfate (APS), ascorbic acid (AsA) and ferrous sulfate. As anticipated, the water/glycerol solution did not dissolve the electrospun fibers and allowed the subsequent cross-linking reaction to proceed. Furthermore, the low toxicity of the chosen redox system allowed the microbes to survive.

The as-spun FDMA/PEO blend scaffold with or without bacteria was cross-linked and subsequently soaked in deionized water to remove PEO and obtain an FDMA fibrous scaffold. The morphological change of FDMA fibrous scaffold (without bacteria) after PEO extraction is shown in Figure 4.4. SEM images showed that the cross-linked FDMA scaffold still maintained the three-dimensional (3D) porous structure after PEO extraction. This structure is in agreement with the morphology of freeze-dried cross-linked fibers that were obtained via electrospinning of other polymeric materials [120]. The porous structure was not only seen on the surface of the electrospun samples (Figure 4.4A and 4.4C), but through the whole thickness of the sample, as apparent from Figure 4.4B (inset), which shows the cross-section (edge) of the scaffold. However, the presence of significant amount of water during cross-linking treatment had affected the fiber morphology to some extent. This was reflected by the fact that fibers at junctions were fused together forming bindings. The change in the distribution of fiber sizes before and after PEO extraction, analyzed using UTHSCSA Image Tool, are shown in Figure 4.5A and 4.5B, respectively. Before PEO extraction, more than 85% of fibers were within the diameter range between 500 and 900 nm. After PEO extraction, the distribution of fiber diameter became much wider and more than 74% of fibers were within the diameter range between 1 and 2 μm.

4.3.3. Thermal Analysis of Electrospun FDMA Fibrous Scaffolds

The TG thermograms of raw FDMA powder, the raw PEO powder, the electrospun FDMA/PEO blend scaffolds and cross-linked FDMA fibers are shown in Figure 4.6. TG

analysis showed that the thermal degradation temperature of FDMA/PEO scaffolds was approximately 350°C, indicating its thermal stability in the temperature range where microorganisms are used (usually lower than 45°C). Also, it should be noted that the thermal degradation temperature of the FDMA/PEO blend was between the thermal degradation temperature of pure PEO powder and FDMA powder, suggesting the mixture of PEO and FDMA in the electrospun blend scaffold. On the other hand, TG analysis showed that the thermal degradation temperature of cross-linked FDMA scaffolds increased from 200°C to 350°C. The increase of the degradation temperature can be readily attributed to the presence of inter-chain molecular cross-links.

4.3.4. Bacteria Immobilized in Dry FDMA/PEO Fibrous Membrane

We then used the above method to encapsulate rod-shaped bacteria in a polymer matrix, which forms a composite fiber during electrospinning. The bacteria were initially suspended in the FDMA/PEO aqueous solution, in which they were found to be randomly oriented (Figure 4.7A). After electrospinning, the rod-like bacteria were found to be oriented, mainly along the direction of the fibers (Figure 4.7B and C). Lower magnification image (Figure 4.7C) showed that the microbes were distributed over the entire area of the electrospun fibers. With higher magnification using confocal microscopy, the individual bacterium could be discerned within these fibers. Figure 4.7D shows a representative cell of the *P. fluorescens* bacterium inside the electrospun FDMA/PEO fibers. The microorganisms were found to be fully encapsulated by the fibers and oriented in the longitudinal direction of the fiber. Similar morphology was also observed when *Z. mobilis* was encapsulated in the electrospun fiber as shown in Figure 4.7E. In all these circumstances, the fiber diameter were found to be only slightly larger than the average size of the microbes used, thereby encapsulating the bacterium with only a thin layer of the polymeric material.

To obtain higher magnification images and to confirm the cellular integrity of bacteria within the single fiber, SEM microscopy was required. To this extent, uranyl acetate was used as a contrast agent to differentiate the microbe from the polymer. Figure 4.7E presents SEM images of uranyl acetate stained *P. fluorescens* prior to and after electrospinning. Figure 4.7E clearly shows that the polymeric matrix has fully

encapsulated the bacterial cell causing a local widening of the fiber. In all these circumstances, the fiber diameters were found to be only slightly larger than the average size of the microbes used, thereby encapsulating the bacterium with only a thin layer of the polymeric material.

We had found that exposure to FDMA and PEO had little or no effect on the viability of the bacteria, even when the bacteria were maintained in this solution for up to a week before assaying them. As described above, electrospinning is an efficient method to encapsulate bacteria in the polymer fiber. However, in the electrospinning process, the removal of water by rapid evaporation is anticipated to cause drastic changes in the osmotic environment of the organism [111]. Furthermore, an electric field, which maybe harmful to the bacteria, is generated by applying a high voltage between the metal capillary and the collector. To asses this effect, non-crosslinked fibers containing *P. fluorescens* were dissolved in culture medium, thereby releasing the bacteria from the fibers. The growth of the bacteria was then monitored by measuring the absorbance at 600 nm (Figure 4.8 and 4.9). It was seen that while the electrospun microorganisms had a slightly longer lag-phase of growth, their growth was barely affected by electrospinning.

In our studies, *Z. mobilis* suspended in a polymeric solution were electrospun, stained with bacterial viability kits, and examined immediately after electrospinning. The images obtained before and after electrospinning are shown in Figures 4.10A-E. Figure 4.10B showed that most (about 93%) of the bacteria were viable immediately after the electrospinning process (viewed as green in the images), before conducting the cross-linking and PEO extraction steps. The effect of storage on the viability of encapsulated bacteria is an important issue for their potential deployment in industrial-scale processes, since the application of these novel bioactive materials requires the bio-hybrid system to be intact and functional (microorganism to be viable) at the time of use at a desired site [110]. To test the viability of the microbes in the fiber over time, the bacteria-containing scaffolds were maintained under saturated humidity conditions and under exclusion of light at 4°C, for up to 7 days. After 1, 3 and 7 days, bacteria encapsulated FDMA/PEO fiber were dissolved in the deionized water to liberate the bacteria. It was determined that although the viability of bacteria decreased over time, significant amount of the bacteria remained viable: ~ 62%, 47% and 23% were found to

be viable after 1 day (Figure 4.10C), 3 days (Figure 4.10D), and 7 days (Figure 4.10E), respectively. Further, to test whether the functionality (metabolic pathway) of the microbe was affected, the uncross-linked fibers containing encapsulated microbes were suspended in growth media and the metabolic products were assessed. *Z. mobilis* is well known for its ethanologenic activity and thus the amount ethanol produced (vol %) was assessed. The results showed that the metabolic activity of the microorganism was not affected by the electrospinning process, and the amount of ethanol produced by the encapsulated microbes was found to be in good agreement with the amount produced by un-encapsulated (free culture) control (Table 1). This was found to be the case after one week of storage at -4^{o}C and up to two months of storage at -70^{o}C. It is thus apparent that the electrospinning process does not adversely affect the metabolic pathway of the microbes.

4.3.5. Bacteria Embedded in Wet Cross-linked FDMA Fibers

Although the cross-linking treatment improved the water-resistance and thermal properties of the electrospun FDMA fibrous membranes, an eventual adverse effect is that such treatment could be cytotoxic to bacteria encapsulated in the fiber. The cytocompatibility of the cross-linking step is critical to the ultimate success of this study. Although polymerization of monomers with carbon-carbon double bonds has been extensively investigated in the past using photopolymerization/photo-crosslinking [132-134], this method cannot be used for the preparation of cross-linked FDMA fibers encapsulated with bacteria. This is not only because the UV light has known microbicidal properties, but also because photopolymerization cannot be carried out uniformly in a large or thick system. Furthermore, the light penetration depth is quite limited and light distribution is inhomogeneous [135]. Chemical cross-linking seems to be a more suitable method for the purpose of this study, although it could be potentially toxic when the bacteria encapsulated in the electrospun fibers are exposed to the cross-linking agent. The most commonly used free radical initiator consists of N,N,N ′ ,N ′ -tetramethylethylenediamine (TEMED) and peroxodisulfate (potassium or ammonium salt) [103, 135-139] and works by polymerization of the methacrylate groups [140]. However, TEMED is toxic to microbes and was not considered in this work [141].

Previous literature has also reported that FDMA could be cross-linked by free radical polymerization at 37°C using a redox system which included APS and sodium metabisulfite [72, 142]. However, sodium metabisulfite releases sulfur dioxide (SO_2) when exposed to water. To prevent any interference from gas evolution and possible changes in the pH due to SO_2 on the cross-linking reaction, the system comprising of ferrous sulfate and AsA was used instead of sodium metabisulfite. Ferrous sulfate is a component of several bacterial growth media and unlike metabisulfate does not degrade in water. The concentration of the APS, ferrous sulfate and AsA was adjusted to as low as possible, by iterative experimentation, to minimize the oxidation of microbes by APS.

The *Z. mobilis* encapsulated FDMA cross-linked fibers were washed with deionized water three times and stained with LIVE/DEAD® BacLight™ bacterial viability kits to visualize the bacteria under the confocal microscope. The confocal microscopy image shown in Figure 4.11A revealed that about 40% of the bacteria were still alive after the electrospinning and cross-linking process. To verify encapsulation of *Z. mobilis* cells by the FDMA fiber, freeze-dried cross-linked FDMA fibers encapsulating the bacteria were examined. Normally, the cross-linked FDMA fibers are multi-layered. Mono-layer of *Z. mobilis* cells encapsulated FDMA fibers is shown here, because it provides better contrast between the microorganism and fiber. Figure 4.11B shows a homogeneous distribution of bacteria in the cross-linked material. Microbes were found to be encapsulated both at the junctions where fibers fused together (Figure 4.11C) as well as in single fiber (Figure 4.11D), with the cellular integrity of the microorganism appearing to be well preserved, regardless of the location.

In order to determine whether the bacteria proliferate within the fibers, we monitored the total number of live and dead *Z. mobilis* cells in cross-linked FDMA fibers for 2 days (Figure 4.12A). The results indicate that the total number of live and dead cells of *Z. mobilis* remained almost constant and there was no proliferation. Similar results were also obtained when we monitored the bacteria encapsulated in the cross-linked bulk hydrogel (Figure 4.12B), without undergoing electrospinning, indicating that some aspect other than the confinement in the fibers is responsible for hindering their proliferation.

The sketch, shown as inset in Figure 4.11D, illustrates the conditions around a

bacterium cell inside a cross-linked FDMA fiber. It should be noted that in contrast to the fibers reported before [101-105], which are composed of a water insoluble polymer shell around a hollow core, formed by dissolution of a hydrophilic component, the fibers discussed here are formed around the bacterium from a uniform hydrophilic polymer solution. When immersed in water, the cross-links prevent the fibers from dissolution, and lead to the formation of a mesh-like network of the swollen polymer within a short time (Figure 4.13). When the gel fibers are fully cross-linked we can estimate that the distance between cross-links is at most the stretched end to end distance of the polymer which is less than 100nm. This distance is large enough to allow the exchange of nutrients and microbial metabolic products between the microbe and the environment, but it is much smaller than the size of the bacteria, thereby immobilizing the microbes inside the open mesh-like enclosure. As an example for the rate of nutrient exchange, it was observed that complete exchange of glucose at a concentration of 80 g/l occurred in ~ 2hours (Figure 4.14).

Furthermore, GFP *E. coli* were also encapsulated using this process and examined using confocal microscopy. The innate fluorescence of GFP *E. coli* was used to easily image the bacteria under confocal microscopy images (Figure 4.15). With higher magnification, single bacterium within the cross-linked fibers could be observed to be oriented in the longitudinal direction of the fiber, with no morphological changes being observed due to the cross-linking reaction. Encapsulation of *E. coli* shows the broad applicability of this process.

4.4. Conclusion

[1] This study describes the development and formation, via electrospinning, of a novel FDMA fibrous hydrogel material with encapsulated microbes. To our knowledge, this is the first insoluble fibrous material containing viable microorganisms that has been reported. The microbes in the material were found to be viable for over a week in the dry FDMA/PEO blend scaffold at 4°C and for over two months at -70°C. The FDMA fibers were cross-linked using a water/glycerol solvent mixture, and the APS, ferrous sulfate and AsA catalytic system. The occurrence of the crosslinking reaction was demonstrated by TG analysis. The integrity and the viability of the bacteria were maintained through the cross-linking process. The mesh-like network of the polymer effectively immobilized the microbe, while allowing the exchange of nutrients and metabolic products between the microorganism and the environment. This study has significant implications for application of immobilized microorganisms and/or synthetic biofilm based bioreactors.

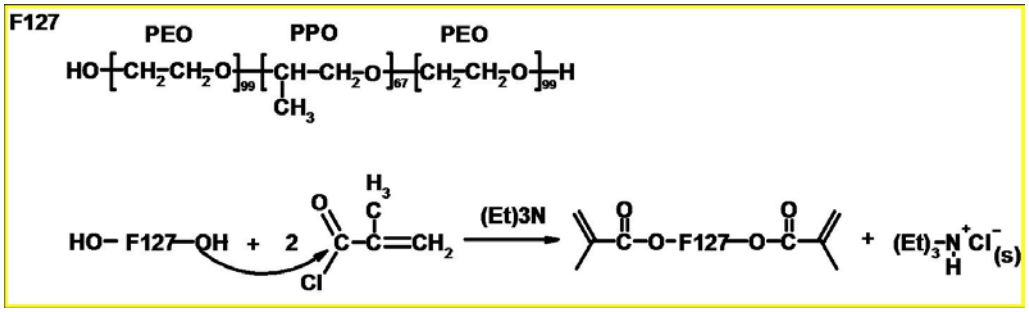

Figure 4.1. Schematic showing the synthesis of F127-DMA.

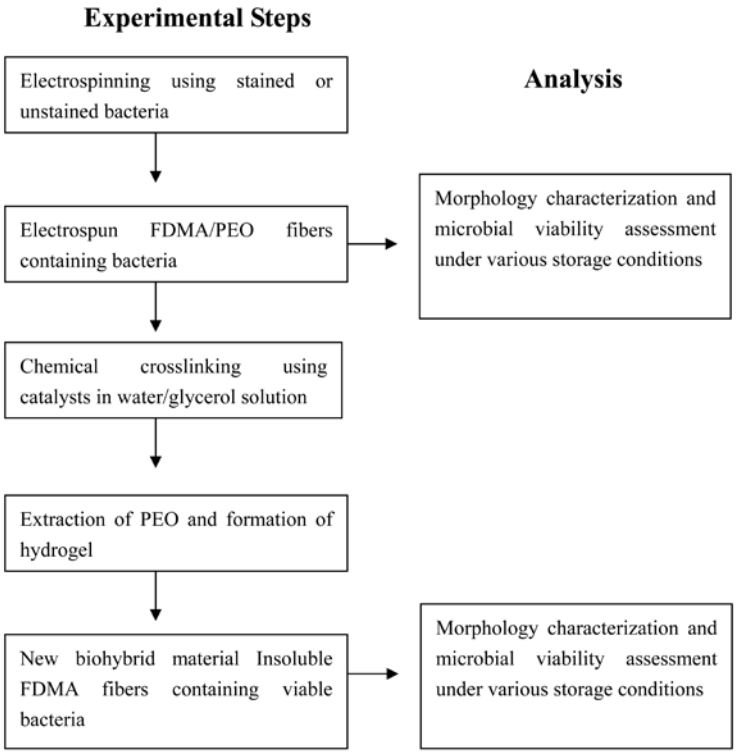

Figure 4.2. A schematic describing the different stages of the process that were undertaken to generate the biohybrid material. The chart shows the various stages at which the fibers were characterized and analyzed.

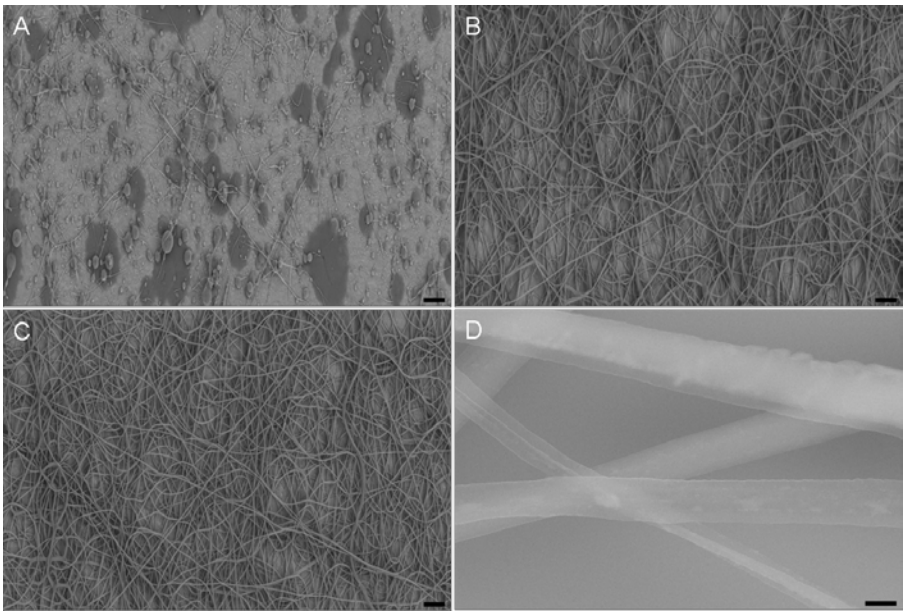

Figure 4.3. SEM images of the electrospun F127-DMA/PEO blend scaffolds with different weight ratio: (A) F-DMA 13wt%, PEO 1wt% (13:1); (B) F-DMA 13wt%: PEO 2wt% (13:2); (C) and (d) F-DMA 13wt%: PEO 3wt% (13:3). Note (D) A higher magnification image of the image in C. Bars, 20 μm (A, B, C), 1 μm(D)

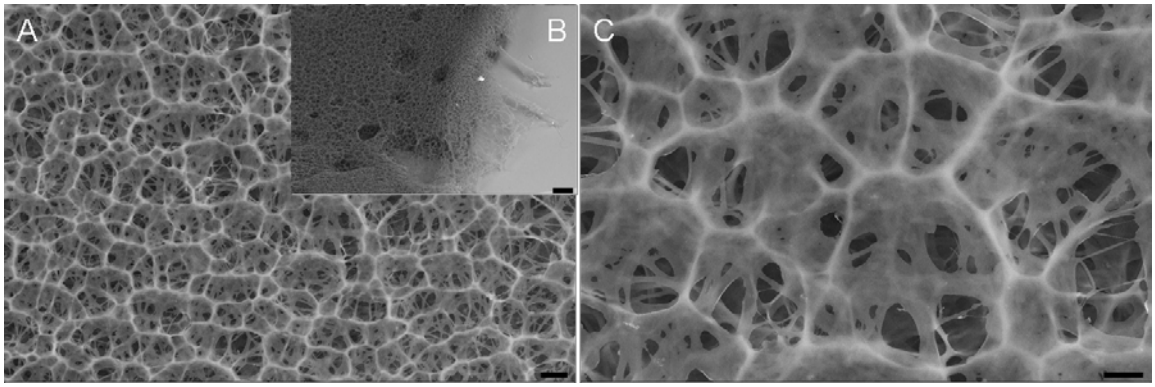

Figure 4.4. Surface (A and C) and edge (B) edge images of the FDMA fibrous scaffold obtained by lyophilization after PEO extraction. (Scale bars, 20 μm in A, 100 μm in B, 10 μm in C).

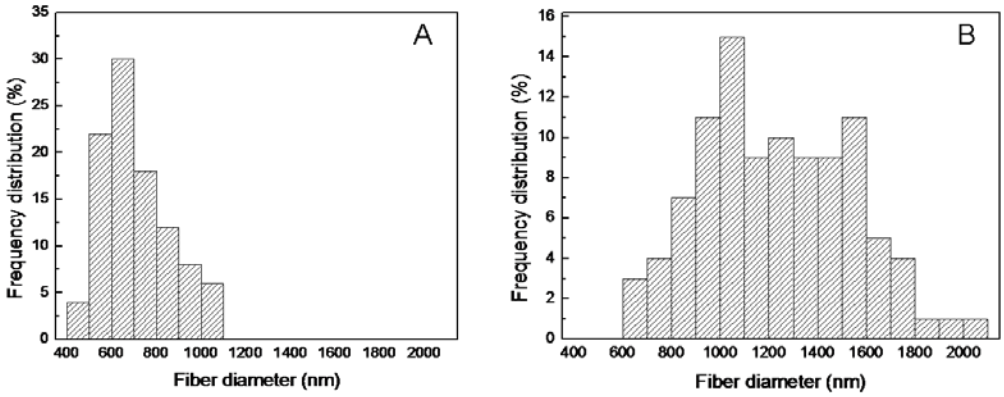

Figure 4.5. Distribution of fiber diameters in FDMA/PEO blend fibrous scaffold electrospun from 13wt% FDMA/PEO aqueous solution with FDMA/PEO weight ratio of 13:3 (A) and cross-linked FDMA fibrous scaffold after PEO extraction (B).

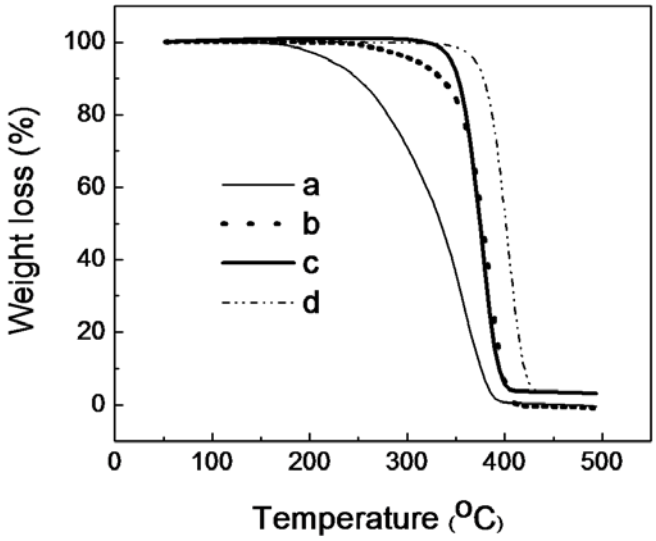

Figure 4.6. TG analyses of different samples: (a) F-DMA powder, (b) F-DMA/PEO blend scaffold, (c) FDMA cross-linked scaffold, and (d) PEO powder.

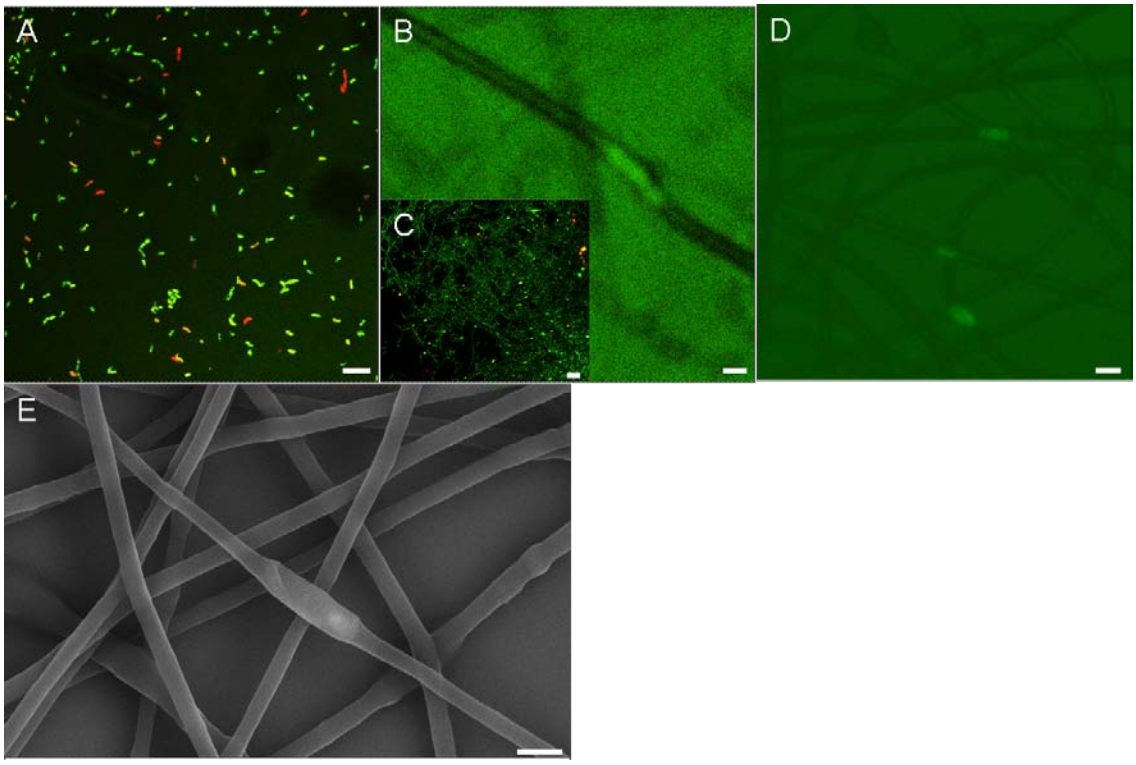

Figure 4.7. Confocal images of stained and fluorescent (red, dead cells; green, live cells) cells of (A) *P. fluorescens* before electrospinning, (B and C) *P. fluorescens* inside the dry electrospun FDMA/PEO blend fibers and, (D) *Z. mobilis* in dry electrospun FDMA/PEO blend fibers. (E) SEM image of uranyl acetate stained *P. fluorescens* cells after electrospinning.
(Scale bars, 10 μm in A, 1 μm in B, 20 μm in C, 2 μm in D, and 1 μm E).

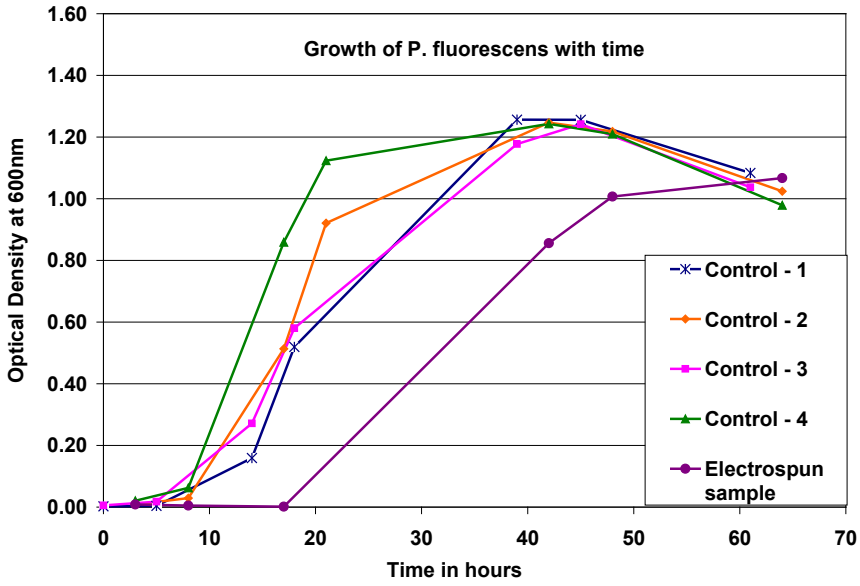

Figure 4.8. The growth of electrospun-immobilized and free *P. fluorescens* in an Erlenmeyer flask containing 50 ml of sterile growth media as monitored by absorption at 600 nm against a culture medium blank. Controls 1, 2 and 3 are from inoculation of 50, 100 and 250 μL of a fresh culture. Control 4 and Electrospun sample denote the growth observed when inoculated with 100 μL of polymer solution containing the bacteria just prior to and immediately after electrospinning.

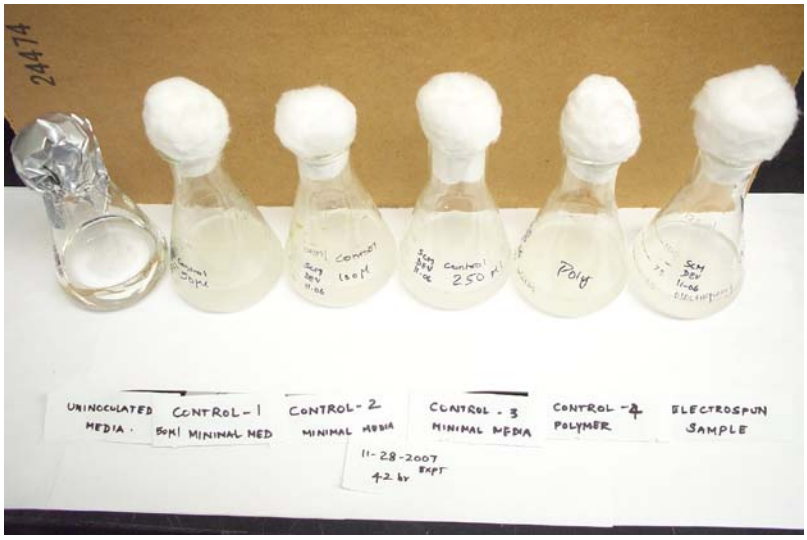

Figure 4.9. A photo of the un-inoculated culture medium and the five inoculated flasks showing the growth of *P. fluorescens* after 42 hours of growth (data shown in previous Figure 4.7). Controls 1, 2 and 3 are from inoculation of 50, 100 and 250 µL of a fresh culture. Control 4 and Electrospun sample denote flasks inoculated with 100 µL of polymer solution containing the bacteria just prior to and immediately after electrospinning.

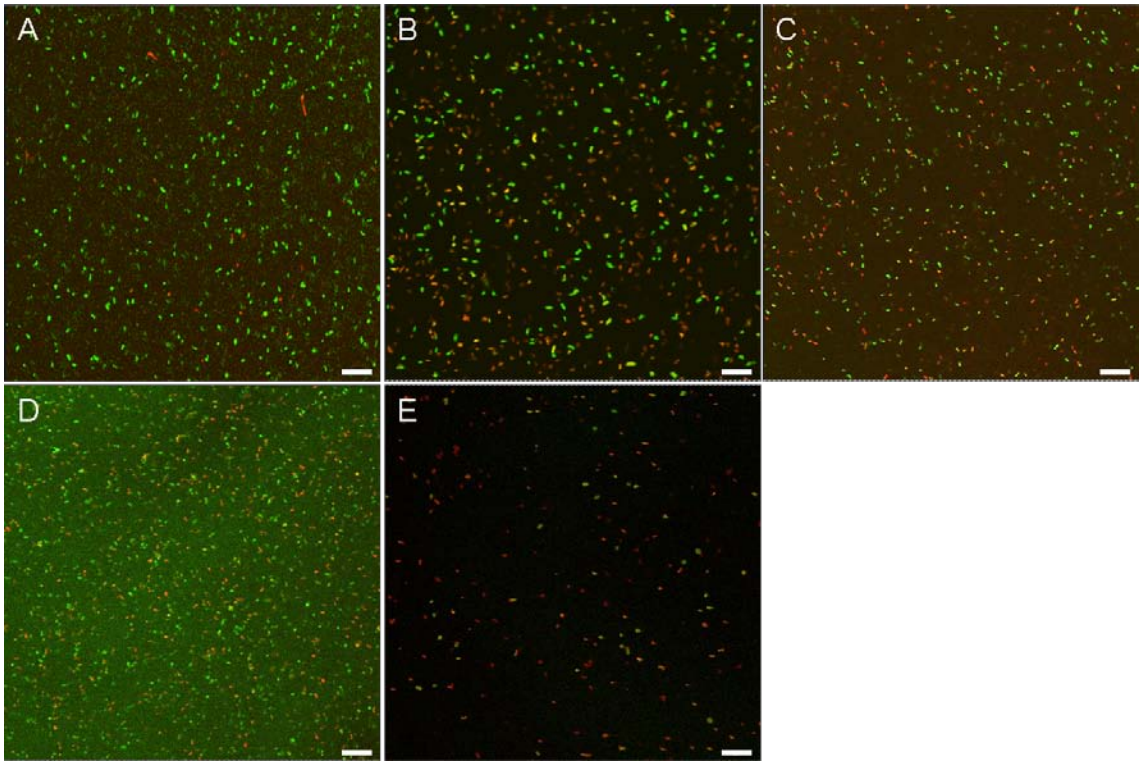

Figure 4.10. Confocal images of *Z. mobilis* cells (A) before electrospinning; (B) immediately after electrospinning; and after storage at 4^{o}C under saturated humidity, with the exclusion of light for (C) 1 day; (D) 3 days; and (E) 7 days. (Scale bars, 20 μm).

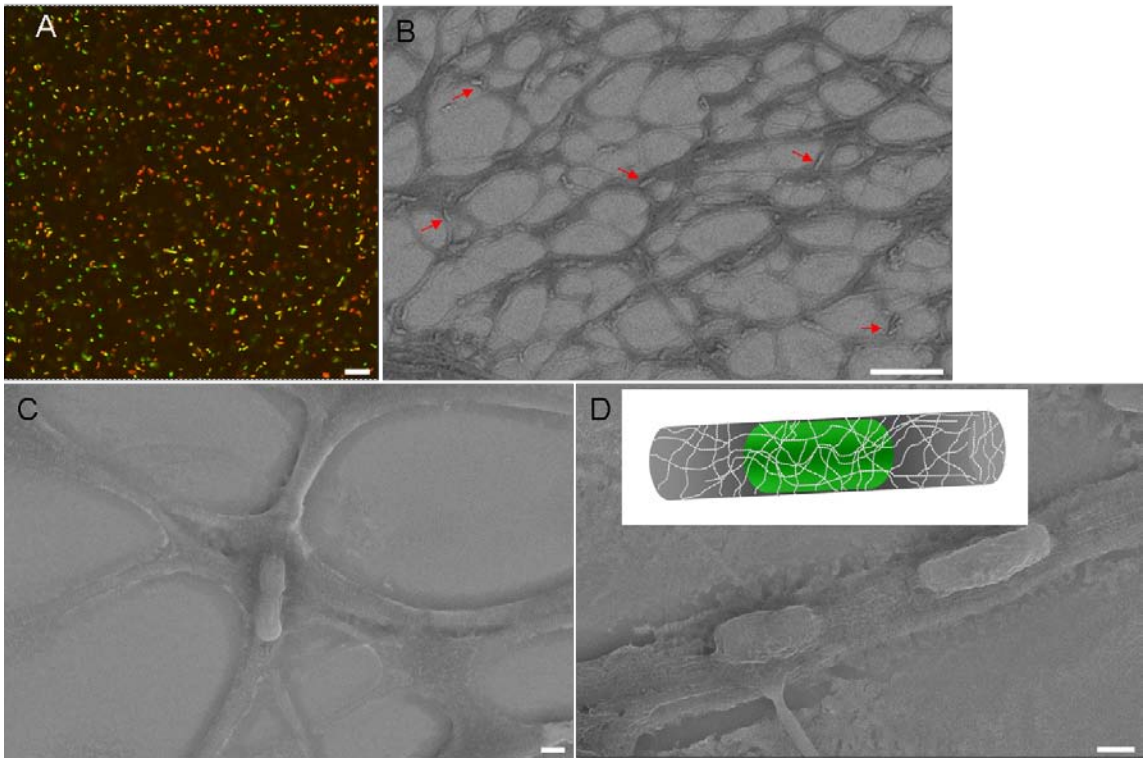

Figure 4.11. Images of *Z. mobilis* within the cross-linked FDMA fibers. (A) Confocal microscopic image of *Z. mobilis* within the cross-linked FDMA fibers shows that about 40% of the bacteria were still alive after the electrospinning and cross-linking process. (Scale bar, 10 μm). (B-D) SEM images of *Z. mobilis* in the cross-linked FDMA fibers. Arrows in image B indicate the locations of a few bacterial cells. Microbes were found to be encapsulated both at the junctions where fibers (C) fused together as well as in (D) single fiber. (Scale bars, 20 μm in B, and 1 μm in C and D). Sketch (inset, D) illustrates a bacterium encapsulated in the cross-linked FDMA fibers.

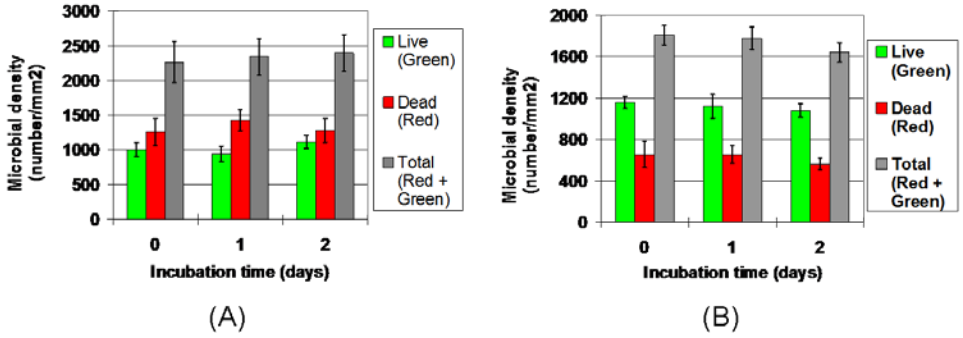

Figure 4.12. Microbial cell counts in cross-linked FDMA (A) fibers and (B) bulk hydrogels, performed using LIVE/DEAD® BacLight™ bacterial viability kits, at different times-day 0: just after cross-linking; day 1: after cross-linking and culturing in the growth media for 24 hours; day 2: after cross-linking and culturing in the growth media for 36 hours. Microbes with intact cell membrane stain fluorescent green and microbes with damaged cell membrane stain fluorescent red.

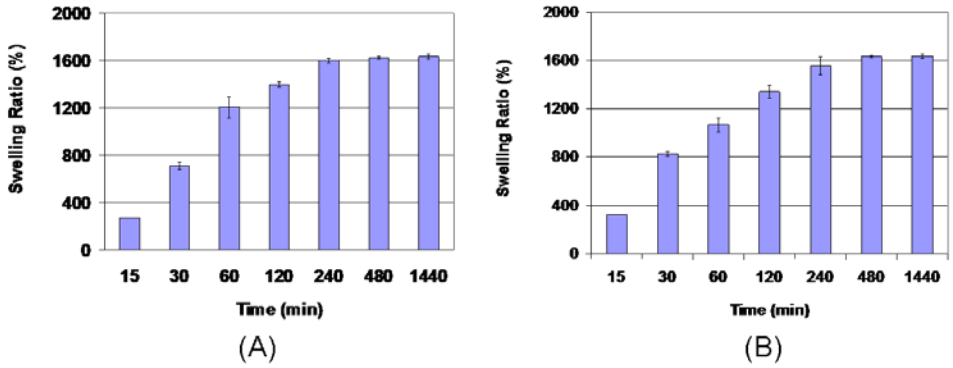

Figure 4.13. Swelling ratio of cross-linked FDMA (A) fibers and (B) bulk hydrogel in deionized water at room temperature.

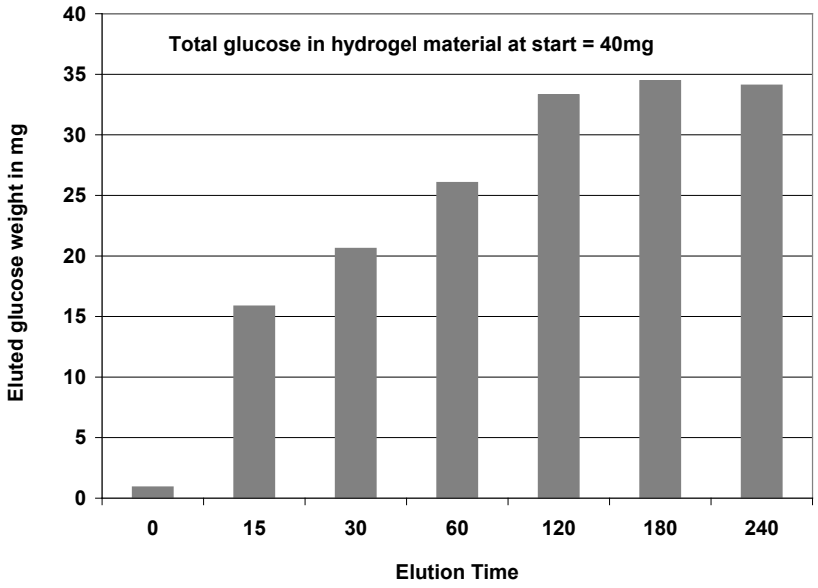

Figure 4.14. 8wt% Glucose release from the cross-linked FDMA hydrogel to 10 mL deionized water at room temperature.

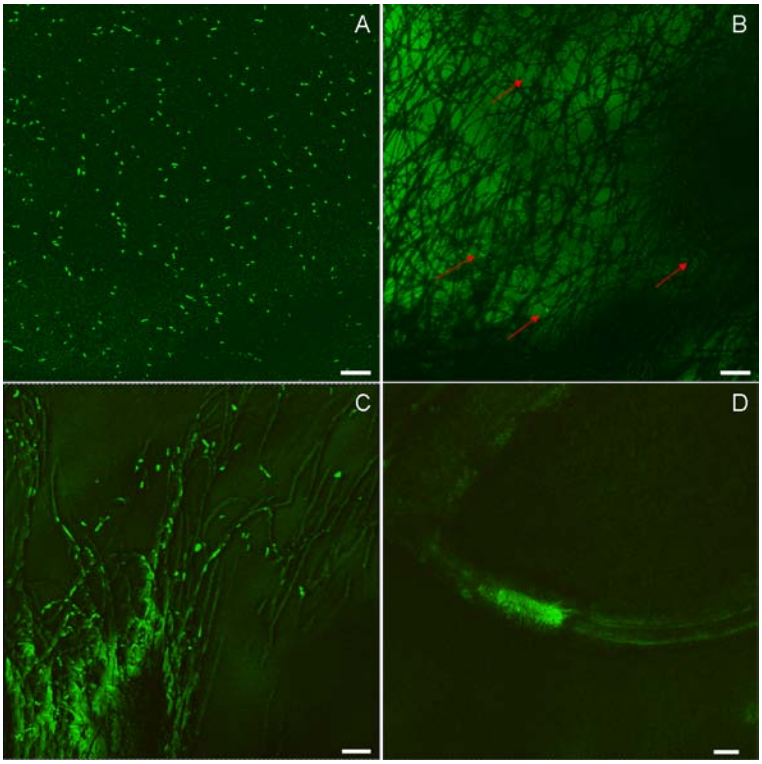

Figure 4.15. Confocal images of GFP-*E. coli* (A) before electrospinning, (B) after electrospinning, and (C, D) confocal microscopic images of GFP-*E. coli* in wet FDMA fibers after electrospinning and cross-linking. The fluorescence property of GFP- *E. coli* makes cells encapsulated in the electrospun F127 DMA/PEO fibers visible.
Bars, 20 μm (A, B), 10 μm (C), 1 μm (D).

Sample ID	Storage temperature in Celsius	Days in storage	Ethanol concentration (vol %)
Sterile Media			0.00
Control - ZM			0.92
Electrospun Samples			
Electrospun ZM	Added to media immediately		0.69
Electrospun ZM	4	1	0.58
Electrospun ZM	4	3	0.62
Electrospun ZM	4	7	0.79
Electrospun ZM	-70	31	0.82
Electrospun ZM	-70	60	0.52

Table 4.1. Amount of ethanol produced by *Z.mobilis* after inoculation of the sterile medium (composition provided in methods section) with various pre- and post electrospun microbial samples. The amount of ethanol produced by the electrospun samples (immediately and after storage) is slightly lower than that produced by the control (free culture, pre electrospinning). This could be explained via the longer lag phase of growth experienced by the electrospun samples, thereby providing more aeration and leading to lower ethanol production.

Chapter 5. Electrospinning of Poly (ethylene-*co*-vinyl acetate)/Clay Nanocomposite Fibers

5.1. Introduction

Semi-crystalline poly (ethylene-co-vinyl acetate) (PEVA) copolymers, being flexible and corrosion resistant materials, are widely used in many commercial products, such as wire insulation, packaging film, adhesives, foams, and sound barrier sheets [143]. These materials can also be used as drug delivery matrices due to their biocompatibility [144-146]. Recently, it has also been found that nanoclays can be effectively exfoliated in PEVA polymers, leading to improved mechanical and flame retardant properties [147-152]. However, most existing work has focused on bulk and thin-film PEVA, while little has been reported on PEVA fibers, which can have distinct physical properties and crystalline structures due to geometric confinement [153].

Electrospinning is a powerful technique for the continuous production of polymeric fibers. Fibers can be electrospun from solutions or melts, and processing conditions (such as solution concentration and conductivity) can be adjusted to control fiber diameter [154-156]. Previously, it was shown that PEVA polymers can be electrospun into thin fibers, with diameters ranging from hundreds of nanometers up to tens of microns [157-159]. Using the same technique, we fabricated the PEVA polymer fibers and systematically determined how fiber diameter and nanoclays can modify the properties of PEVA copolymers.

In this study, fiber/clay nanocomposite fibers were prepared and their properties were characterized in detail. Specifically, fiber morphologies, crystalline structures and clay orientations were studied by using scanning electron microscopy (SEM), transmission electron microscopy (TEM), small-angle X-ray scattering (SAXS) and X-ray diffraction (XRD). Shear modulation force microscopy (SMFM), described previously by Ge *et al.*

[160], was used to directly measure the local melting point of single fibers, and determine the correlation between fiber diameter and clay concentration.

5.2. Experimental Section

5.2.1. Materials

PEVA260 was purchased from Dupont Co. with the commercial name Elvax 260 (polydispersed random copolymer with 72 wt% ethylene, $T_m = 75\,^{o}C$). Chloroform was purchased from Fisher Science. Cloisite 10A (Southern Clay Products, Gonzales, TX) is a natural montmorillonite modified with a quaternary ammonium salt.

5.2.2. Electrospinning of PEVA/Clay Nanocomposite Fibers

To prepare electrospun PEVA/clay composite fibers, PEVA260 and Cloisite 10A clay with different weight concentrations were dissolved in chloroform. The solutions were left for 24 h on a heated surface to completely dissolve the pure polymer and the nanocomposites. The PEVA/clay solutions were then sonicated for another 3 h to obtain homogenous solutions for electrospinning. 3 mL of the solution was drawn into a 5 mL glass syringe (Hamilton Company, Reno, NV) that was then secured onto the graduated pump (KD Scientific, Holliston, MA), and the flow rate was set to be 50 μL/min. The high voltage power supply (Gamma High Voltage Research, Ormond Beach, FL) was set to be 10 kV and attached to the needle. Electrospun fibers were collected on cleaned aluminum foils or silicon wafers as randomly oriented fiber mats on the aluminum target which was horizontally placed 10 cm away from the tip of the needle. The electrospun fibers were then annealed in a vacuum overnight. The diameter distributions of PEVA fibers, with or without clay, were obtained by analyzing the SEM image with Image Tool (The University of Texas, Health Science Center in San Antonio)

5.2.3. Characterization of PEVA/Clay Nanocomposite Fibers

The morphologies of the fibers were imaged by using a Digital Instruments Dimension 3000 scanning probe microscope (SPM) in the contact mode using a Si_3N_4 tip. More detailed structure was imaged with SEM (LEO 1550, LEO, Germany) at 2.5 kV acceleration voltage and 2-4 mm working distance. All fiber samples were sputter-coated

with gold to improve the surface conductivity. A FEI BioTwinG^2 TEM was employed to investigate the interior structure of electrospun fibers. TEM samples were obtained by directly electrospinning the fibers onto a copper sample grid.

SAXS measurements for the PEVA bulk and fiber materials were carried out at the X10A beamline of the National Synchrotron Light Source (NSLS), Brookhaven National Laboratory (BNL), using a photon energy of 11.3 keV, i.e., X-ray wavelength (λ) of 1.097 Å.

The melting point (T_m) of single fibers was measured by SMFM. Measurements were made using a SPM located in a sealed glovebox purged with dry nitrogen. Samples were mounted on a heating/cooling stage (MMR Technologies) and the same etched silicon cantilever (Digital Instruments) with a spring constant of ~0.1 N/m was used for all measurements. In this method, a sinusoidal drive signal with a frequency of 1400 Hz was applied to the x-piezo controlling the cantilever, inducing a small oscillatory motion of the tip parallel to the sample surface. A normal load force of 25 nN was applied to the tip which produced an indentation, h, into the sample. The lateral deflection amplitude Δx was measured as the output, which has the following relationship with the lateral modulus of the fibers: $\Delta x \propto G^{-2/3}$, where G is the surface shear modulus. Since G decreases by orders of magnitude when the fiber melts at $T = T_m$, the signal has a strong and sharp transition.

X-ray diffraction (XRD) measurements were performed using an Ultima III theta-theta diffractometer (Rigaku, Japan) with copper anode, generator power of 1.6 kW, incident angle of 5º, Bragg Brentano optics and Ni filter. For photon counting, a scintillation counter was used. Step size was 0.02º and scan rate was 0.5º/min. The polymer sample deposited on aluminum foil was placed on the copper plate holder of the low-mid variable temperature attachment of the diffractometer. The heating rate was 0.5º/min and the temperature equilibration time was 5 min.

5.3. Results and Discussion

5.3.1. Fabrication of Electrospun PEVA/Clay Fibers with Controllable Diameter

To study the surface mechanical properties of electrospun fibers as a function of the fiber diameter, we fixed the processing parameters, such as voltage, stock solution feed rate and working distance in the electrospinning process. The fiber diameter was controlled by varying the solution concentration and the relationship between these quantities is shown in Figure 5.1. From the figure we see that the diameter obeys a power law relationship with the solution concentration. The solution concentration in turn can be a function of the viscosity, as shown in Figure 5.1b. We can therefore relate the diameter directly to the solution viscosity, as shown in Figure 5.1c. These results agree with previous report [36]. Figure 5.2 shows SEM images of the fiber morphology where we see that at low concentration, "donut" shaped features have formed (Figure 5.2a). These features are more prominent when the fibers are thinner. With increasing concentration, the features become smaller (Figure 5.2b), till at 14.5wt%, they disappear (Figure 5.2c).

We then fixed the concentration of PEVA in the electrospinning solution to be 7.5wt% and changed the weight percent of the clay from 0.35wt%, 3.5wt%, to 6.6wt%. From the inset to the Figure 5.1 and the SEM images (Figure 5.3) we see that the fiber diameter increases linearly with clay concentration as well, from 2.8 μm, 3.2 μm to 4.3 μm which may be caused by the increased viscosity of the spinning solution due to the clays. Adding larger amounts of clays was not practical since the solutions became too viscous to be electrospun.

5.3.2. Clay Effects on the Structure of PEVA Fibers

In Figure 5.4 we show TEM images of the fibers without and with clay. From the images we can see that in the absence of clay (Figure 5.4a), ordered spherulites are seen on the fiber surfaces (red circle). When clay is added (Figure 5.4b), the spherulite order is disrupted as the number of nucleation sites is increased, which is consistent with the heterogeneous nucleation previously reported for bulk EVA [161, 162]. Higher

magnification images show that the platelets are well exfoliated within the fibers for low concentrations, but large agglomerates are formed when the concentration was increased to 6.6wt% clay. On the other hand, despite the agglomerates, from Figure 5.3 we find that the beads disappear for clay concentration above 3.5wt%. Hence the beads are associated with the viscosity of the spinning solution, rather than being a result of excess clay concentration. Furthermore, we find that the clay platelets are oriented along the fiber axis, where the shear is large.

In order to further characterize the effect of the clay on the structure of the PEVA fibers, we also measured SAXS for the fibers. The results are shown in Figure 5.5 where we plot the data for bulk PEVA and for the fibers with different clay concentrations. For the lowest clay concentration we found a small peak at $q = 0.6\,\mathrm{nm}^{-1}$ in the SAXS profile, indicating the presence of lamellar domains in the fibers with interlamellar spacing of ~9nm. Interestingly, the interlamellar spacing is slightly smaller than that of the bulk (~10nm). On the other hand, in the case of the fibers with the higher concentration of the clay particles, no significant scattering peak was observed. This indicates an increase in the degree of disorder in these samples.

The morphologies of electrospun PEVA fibers were also studied using SPM and the images are shown Figure 5.6. Cross section analysis of typical fibers without and with 3.5wt% clay is shown, where we can see that the fibers are flat ribbons, i.e. the fiber thickness in both cases is approximately 0.7 and 1.5 μm, while their width is 7.5 and 5 μm, respectively. Lateral force microscopy (Figure 5.6, right images) reveals that when clay is added, high friction domains appear on the surface. The difference in friction is due to different interactions of the SPM tip between the matrix and the clay particles. According to the manufacturer, the Cloisite 10A clay platelets are 1nm thick, 75-100 nm in lateral dimensions when completely exfoliated. The higher friction domains have lateral dimensions of 0.4×1 μm, which leads us to conclude that they correspond to the clay tactoids.

5.3.3. Melting Temperature Depression

SMFM was used to measure the melting point of the fibers as a function of fiber

diameter and clay concentration. This technique was chosen since it was possible to simultaneously measure both the fiber diameter and T_m, which means we can select fibers of different diameters to probe the effect on T_m. When the fiber melts, the modulus decreases by three orders of magnitude, causing a large increase in the deflection, and this discontinuity in the trace is indicative of T_m. In contrast to glass transition measurements where this technique has been used [163], melting is a first order transition and hence an abrupt change is observed with temperature. The midpoint of the curve corresponds to T_m of the material. In Figure 5.7a, we plot the deflection amplitude of the cantilever (Δx) *vs* temperature curves for fibers in the absence of clay which were electrospun from a solution of 8.5wt% EVA in chloroform, corresponding to the SEM image in Figure 5.2b. The representative results for PEVA260 fibers electrospun from a solution with clay (6.6wt%) are also shown in Figure 5.7b, where the data is plotted for fibers of different diameters. In Figure 5.7c we plot the T_m values extracted from these data as a function of fiber diameter for samples without and with different clay concentrations. From the figure we can see that in the absence of clay, the T_m becomes depressed relative to the bulk for fibers thinner than 10 microns. This value is still much thicker than either the lamellar thickness, the chain dimension, or even the thickness of the films previously reported where these confinement effects were first observed [164]. For the thinnest fibers containing clay, we find that T_m is depressed even further, relative to the unfilled samples.

In order to determine whether this effect was confined strictly to the surface of the fibers, i.e. the top few nanometers, where the effect was also seen in thin films, we measured XRD of the fibers as a function of temperature on the fibers electrospun from 8.5wt% PEVA solutions. In Figure 5.8 we plot both the frequency distribution of the fiber diameters (red column) for this sample and the sum of the frequency below each diameter (blue column). Using Figure 5.7c, where we plotted T_m vs diameter, we conclude that the crystalline fraction remaining at a given temperature should be a function of fiber diameter. This information can also be obtained by integrating under the crystalline peak at $2\theta \approx 22^\circ$ in Figure 5.9a. The peak position is that expected for the dominant 110

reflection of orthorhombic polyethylene. We set the peak intensity at 45°C as unity, and obtained the ratio for each temperature. The peak intensity loss was defined as the difference between the ratio at 45°C and other temperatures, respectively (Figure 5.9b). From Figure 5. 7c, 5.8 (blue columns) and 5.9b, we can compare the values obtained by the two methods and demonstrate that qualitative agreement is obtained. These results indicate that the melting point depression occurs throughout the fiber rather than a being concentrated at the surface.

The decrease in melting point with smaller fiber diameter is more difficult to understand. Wang *et al.* [164] reported a decrease in T_m for thin polyethylene (PE) semi-crystalline films. Since the decrease occurred only for films thinner than 0.15 μm, it was interpreted as being due to chain confinement. The fiber thicknesses in this case are much larger than the chain dimensions. Zussaman *et al.* [153] have previously suggested that Young's modulus influences chain stretching during the electrospinning process. Hence it is possible that distortion of the chains induced by electrospinning is also producing a reduction of T_m. The orientation was also shown to propagate for large distances relative to the polymer chain radius of gyration, R_g, within the fiber, hence producing a dependence on fiber diameter. This model can be applicable and will be explored. The increased reduction with clay, may be due to the increased number of alignment surfaces within the fiber, as was previously shown to occur for carbon nanotube containing fibers [165].

5.4. Conclusion

PEVA/clay composite fibers with diameters ranging from 1 to 15 μm were fabricated using electrospinning. TEM images demonstrate that clays are distributed homogeneously within fibers up to a concentration of 3.5wt%, but form agglomerates at higher concentrations. SEM data revealed that bead formation was suppressed with increasing clay concentration. The crystallinity was examined using SAXS and TEM. A bread peak was observed at $q = 0.6\,\mathrm{nm}^{-1}$, and this value was insensitive to fiber diameter. On the other hand, the peak was difficult to observe in the clay containing samples. TEM images revealed spherulites on the fiber surfaces. When clay was added, the spherulites were smaller and more numerous, which is consistent with heterogeneous nucleation. SMFM was used to measure T_m of PEVA fibers without and with clay. The results indicated a large reduction with decreasing fiber diameter. The decrease was further enhanced by the presence of clays. XRD was also performed as a function of temperature, which confirmed the SMFM data and indicated that the effect was not an artifact of the surface.

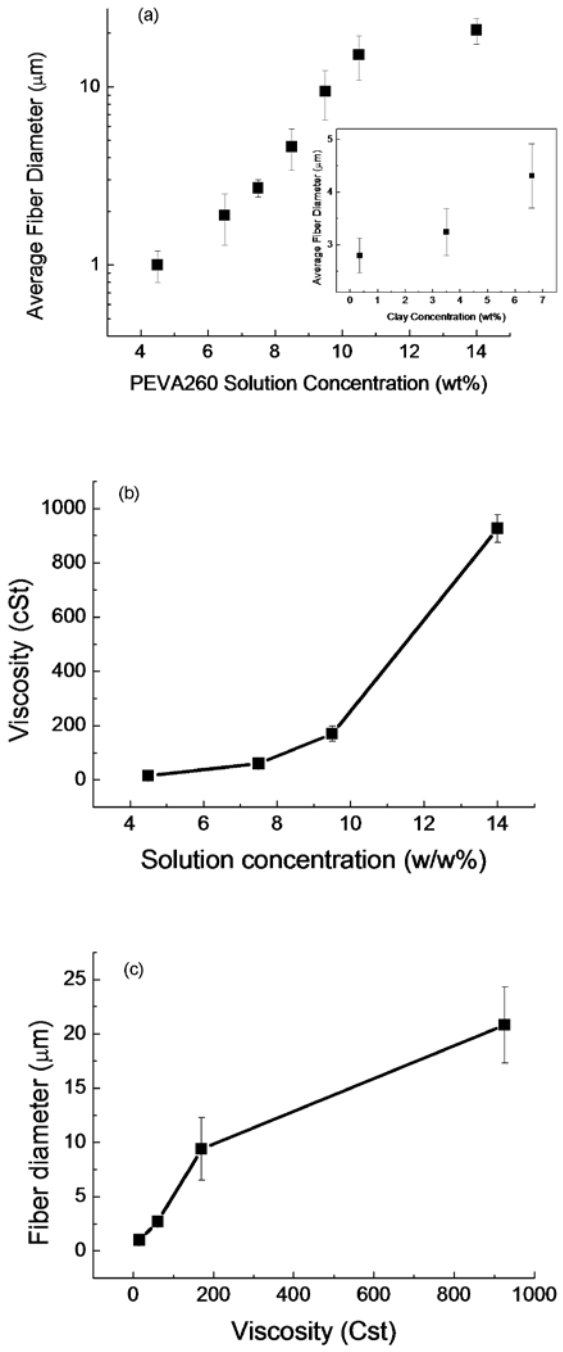

Figure 5.1. (a) Average diameter of electrospun PEVA260 fibers as a function of the solution concentration. Insert: Average fiber diameter as function of clay concentration. Here the fibers were obtained at PEVA260 concentration of 7.5wt%. (b) Solution viscosity as a function of concentration and (c) fiber diameter of PEVA260 fibers as a function of solution viscosity.

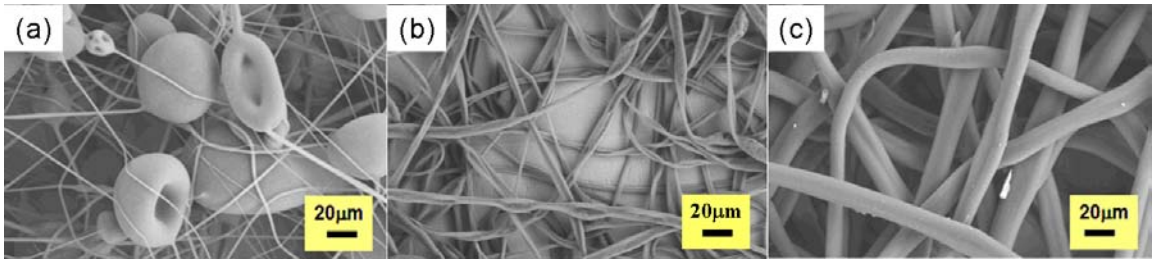

Figure 5.2. SEM images of electrospun PEVA260 fibers at different PEVA260 concentrations: (a) 7.5wt%, (b) 8.5wt%, and (c) 14.5wt%.

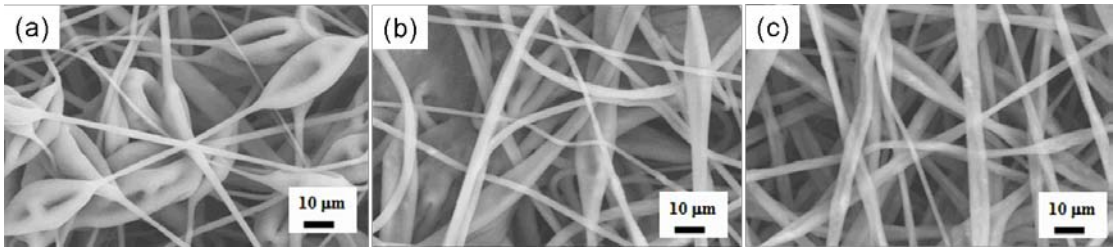

Figure 5.3. SEM images of electrospun 7.5wt% PEVA260 fibers with different concentrations of clay: (a) 0.35wt%, (b) 3.5wt%, and (c) 6.6wt%.

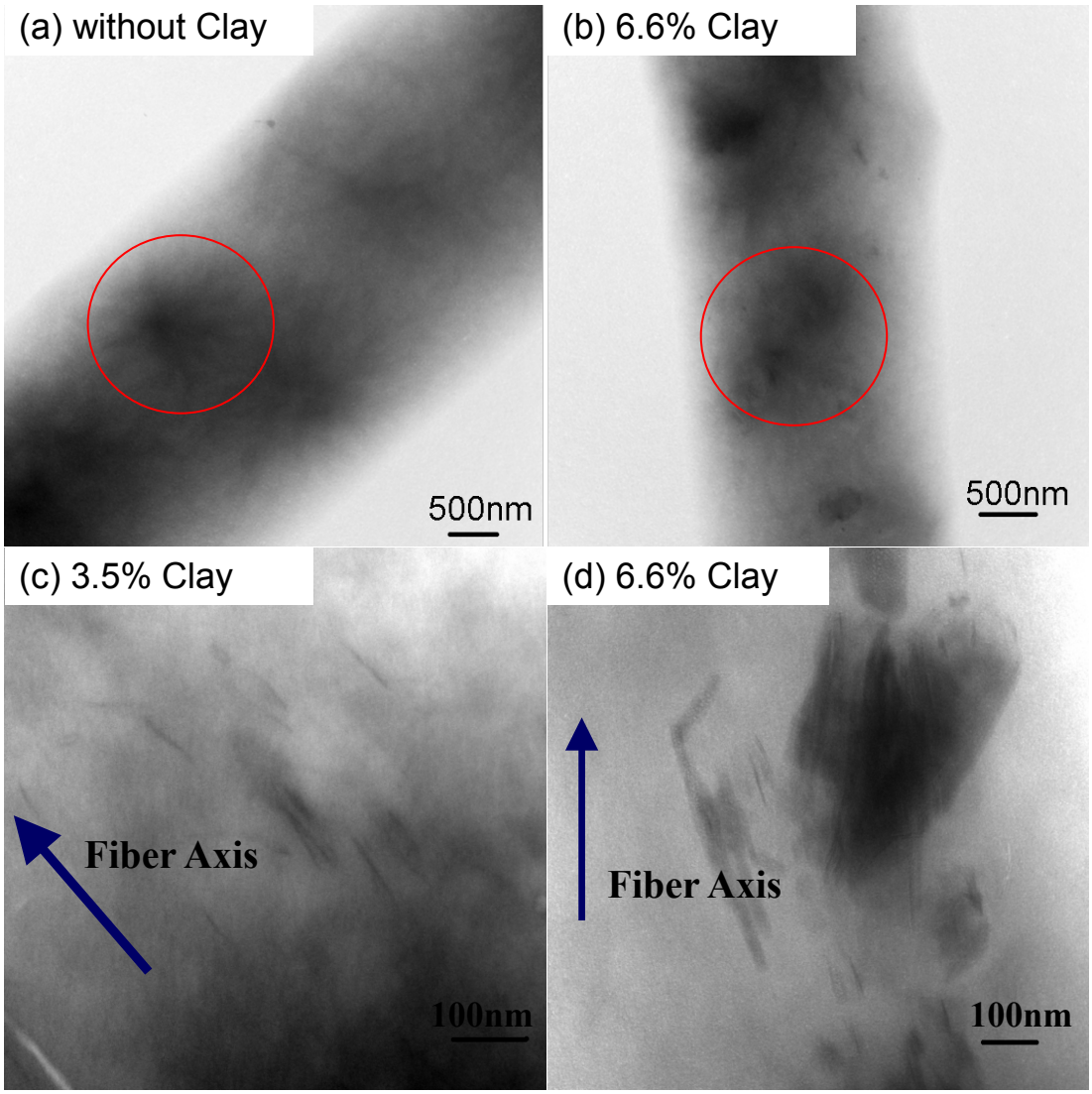

Figure 5.4. TEM images of the electrospun 7.5wt% PEVA260 fibers (a) without and with (b) 6.6wt% clay. TEM micrographs of the nanocomposite based on electrospun 7.5wt% PEVA260 fibers with (c) 3.5wt% and (d) 6.6wt% clay.

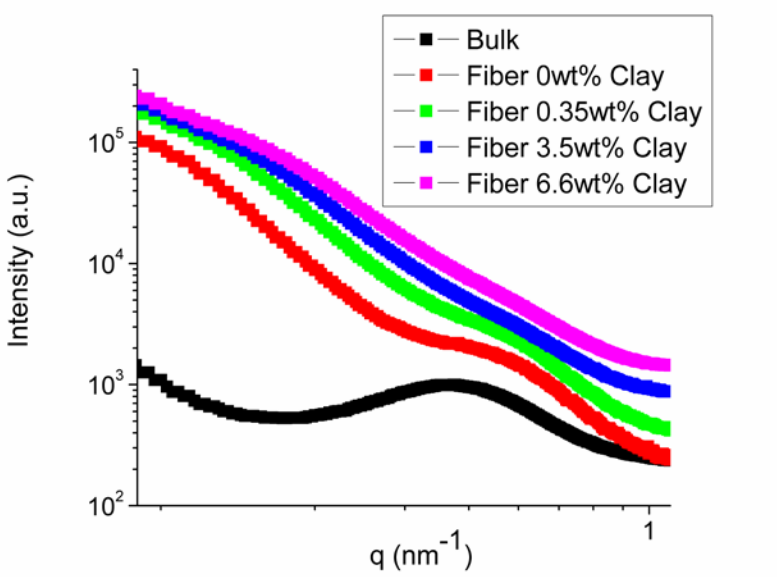

Figure 5.5. Small-angle X-ray scattering profiles of the PEVA260 bulk material and the electrospun fibers with different clay concentrations.

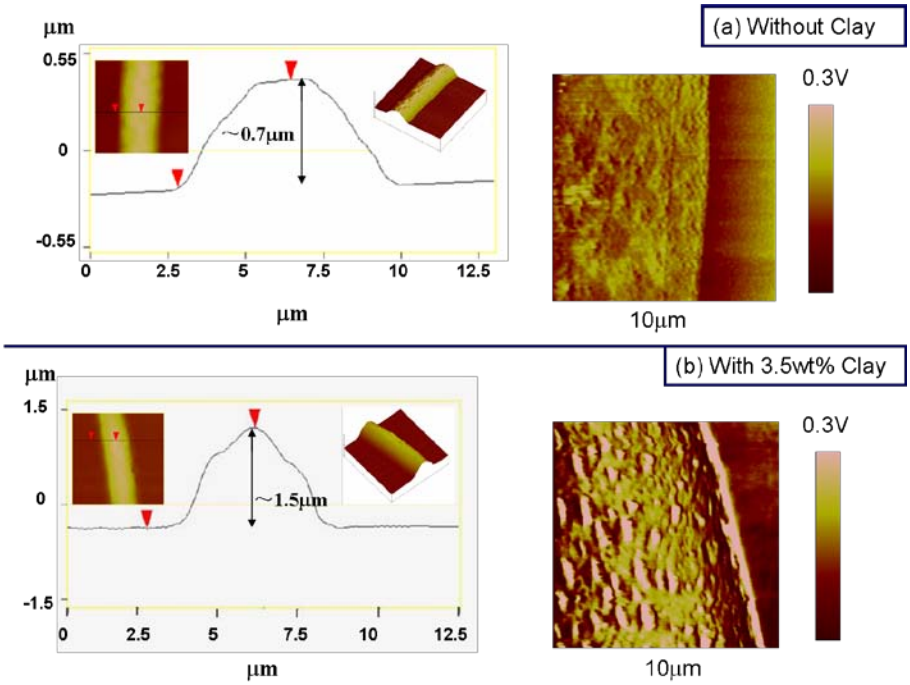

Figure 5.6. (a) Representative height profile of a PEVA260 fiber obtained by SPM along the line indicated (left) and SPM friction image (right) of the fiber. (b) A height profile (left) and SPM friction image (right) of a PEVA260 fiber with 3.5wt% clay.

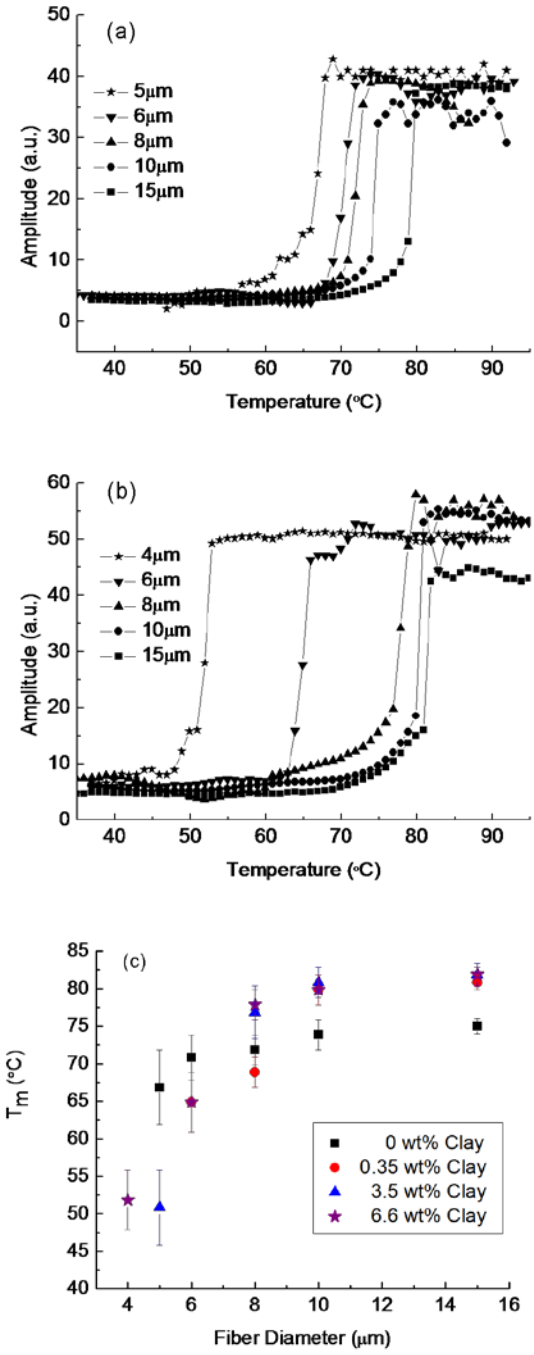

Figure 5.7. T_m dependence on the fiber diameter and clay concentrations. The deflection amplitude of the cantilever (Δx) *vs* temperature curves for fibers (a) in the absence of clay and (b) with 6.6wt% clay. The temperature where the amplitude abruptly increases is the melting point. Note the melting point depression with decreasing fiber diameter. (c) Summary of the T_m as a function of the fiber diameter.

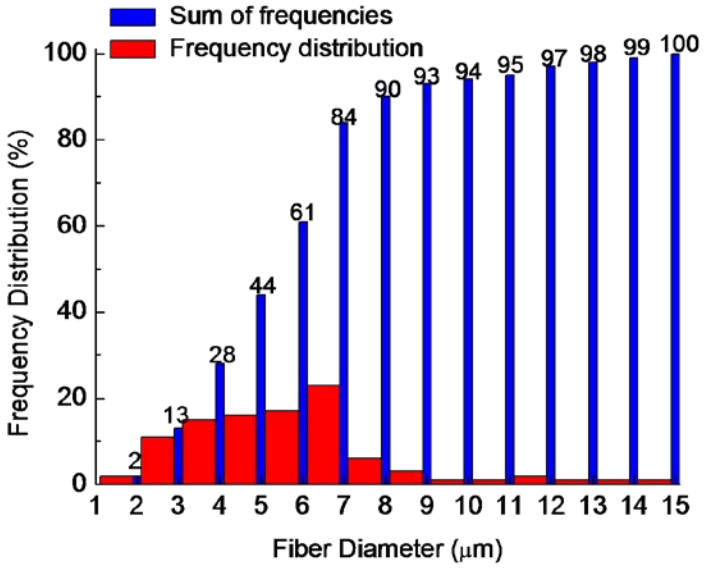

Figure 5.8. Frequency distribution of the fiber diameters (red column) and the sum of the frequency at each diameter (blue column) of electrospun PEVA260 fibers with concentration of 8.5wt%.

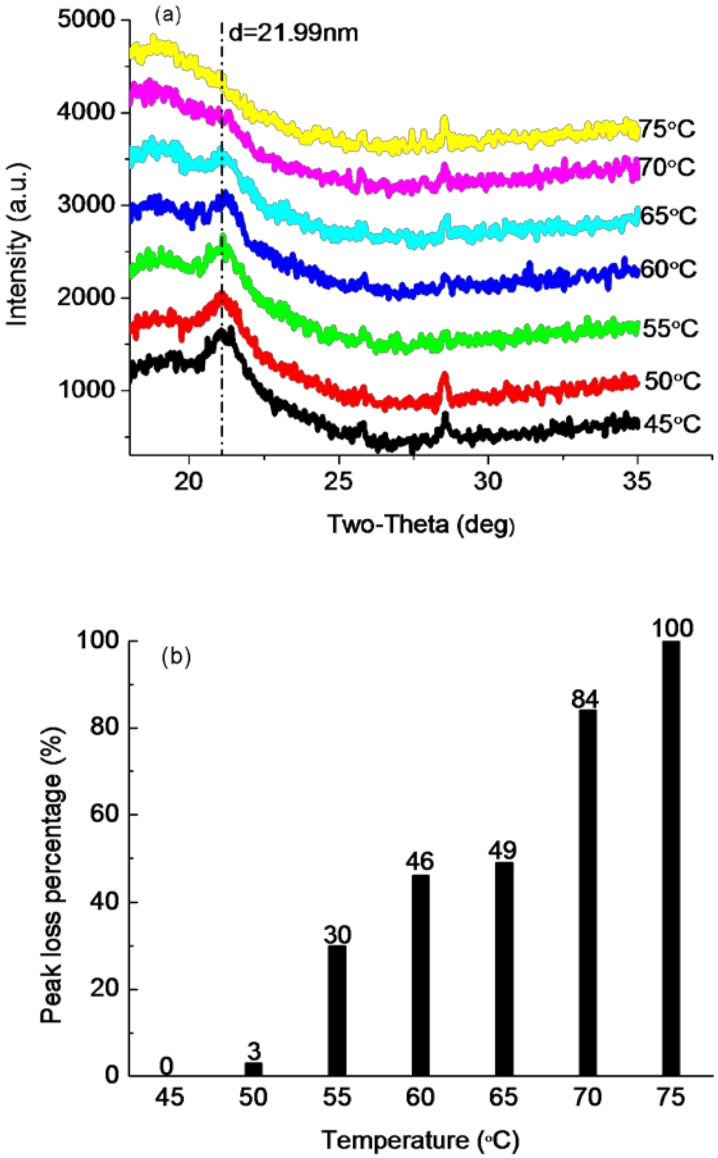

Figure 5.9. (a) X-ray diffraction profiles measured at different temperature for PEVA260 fibers electrospun from a 8.5wt% solution in the absence of clay. (b) The integrated intensity of the diffraction peak at $2\theta \approx 22^{\circ}$ was determined as a function of temperature from 45 to 75˚C. The peak loss was calculated accordi ng to the integrated intensity at 45˚C, which was assumed to be 100%.

Reference

[1] Huang, Z. M.; Zhang, Y. Z.; Kotaki, M.; Ramakrishna S. *Composites Science and Technology* **2003**, 63, 2223-2253.

[2] Shin, Y. M.; Hohman, M. M.; Brenner, M. P.; Rutledge, G. C. *Applied Physics Letters* **2001**, 78, 1149-1151.

[3] Cooke, T. F. *Journal of Polymer Engineering* **1990**, 9, 171-211.

[4] Murugan, R.; Ramakrishna, S. *Tissue Engineering* **2006**, 13, 1845-1866.

[5] Maheshwari, S.; Chang, H. C. *Advanced Materials* **2009**, 21, 349-354.

[6] Doshi, J.; Rneker, D. H. *Journal of Electrostatics* 1995, 35, 151-160.

[7] Li, D.; Xia, Y. N. *Advanced Materials* **2004**, 16, 1151-1170.

[8] Teo, W. E.; Ramakrishna, S. *Nanotechnology* 2006, 17, R89-R106.

[9] Formhals, A. US patent, **1934**, 1, 975, 504.

[10] Reneker, D. H.; Chun, I. *Nanotechnology* **1996**, 7, 216-223.

[11] Sanchez, J. L.; Guy, G.; van Kan, J. A.; Osipowicz, T.; Watt, F. *Nuclear Instrument and Methods in Physics Research Section B* **1999**, 158, 185-189.

[12] Singhvi, R.; Kumar, A.; Lopez, G. P.; Stephanopoulos, G. N.; Wang, D. I.; Whitesides, G. M.; Ingber, D. E. *Science 1994*, 264, 696-698.

[13] Rosenberg, M. D. *Science* **1963**, 139, 411-412.

[14] Hsu, S. H. ; Lu, P. S. ; Ni, H. C. ; Su, C. H. *Biomedical Microdevices* **2007**, 9, 665-674.

[15] Miller, C. A.; Shanks, H.; Witt, A.; Rutkowski, G.; Mallapragada, S. K. *Biomaterials* **2001**, 22, 1263-1269.

[16] Dalby, M. J; Riehle, M. O.; Yarwood, S. J.; Wilkinson, C. D. W.; Curtis, A. S. G. *Experimental Cell Research* **2003**, 284, 274-282.

[17] Recknor, J. B.; Recknor, J. C.; Sakaguchi, D. S.; Mallapragada, S. K. *Biomaterials* **2004**, 25, 2753-2767.

[18] Lenhert, S.; Meier, M. B.; Meyer, U.; Chi, L. F.; Wiesmann, H. P. *Biomaterials* **2005**, 26, 563-570.

[19] Schmalenberg, K. E.; Uhrich, K. E. *Biomaterials* **2005**, 26, 1423-1430.

[20] Charest, J. L.; Eliason, M. T. ; Garcia, A. J. ; King, W. P. ; Talin, A. A ; Simmon, B. A. *J. Vac. Sci. Technol. B* **2005**, 23, 3011-3014.

[21] Lam, M. T.; Sim, S.; Zhu, X. Y.; Takayama, S. *Biomaterials* **2006**, 27, 4340-4347.

[22] Wang, D. Y.; Huang, Y. C.; Chiang, H. S.; Wo, A. M.; Huang, Y. Y. *J. Polym. Sci. Part B: Polym. Phys.* **2007**, 80B, 447-453.

[23] Huang, Z.M.; Zhang, Y. Z.; Kotaki, M.; Ramakrishna, S. *Composites Science and Technology* **2003**, 63, 2223-2253.

[24] Li, D.; Wang, Y. L.; Xia, Y. N. *Adv. Mater.* **2004**, 16, 361-366.

[25] Sundaray, B.; Subramanian, V.; Natarajan, T. S.; Xiang, R. Z.; Chang, C. C.; Fann, W. S. *Appl. Phys. Lett* **2004**, 84, 1222-1224.

[26] McMahon, T. T.; Polse, K. A.; McNamara, N.; Viana, M. A. G. *Optometry and Vision Science* **1996**, 73, 184-188.

[27] Jager, M.; Wilke, A. *J Biomater. Sci. Polym. Ed.* **2003**, 14, 1283-1298.

[28] Patel, S.; Thakar, R. G.; Wong, J.; McLeod, S. D.; Li, S. *Biomaterials* **2006**, 27, 2890-2897.

[29] Ozcan, C.; Hasirci, N. *J Biomater. Sci. Polym. Ed.* **2007**, 18, 758-773.

[30] Alaerts, J. A.; De Cupere, V. M.; Moser, S.; de Aguilar, P. V. B.; Rouxhet, P. G. *Biomaterials* **2001**, 22, 1635-1642.

[31] Risbud, M. V.; Dabhade, R.; Gangal, S.; Bhonde, R. *J. Biomater. Sci. Polym. Ed.* **2002**, 13, 1067-1080.

[32] Schmalenberg, K. E.; Buettner, H. M.; Uhrich, K. E. *Biomaterials* **2004**, 25, 1851-1857.

[33] Yim, E. K. F; Reano, R. M; Pang, S. W; Yee, A. F.; Chen, C. S.; Leong, K. W. *Biomaterials* **2005**, 26, 5405-5413.

[34] Megelski, S.; Stephens, J. S.; Chase, D. B.; Rabolt, J. F. *Macromolecules* **2002**, 35, 8456-8466.

[35] Dong, H.; Nyame, V.; Macdiarmid, A. G.; Jones, W. E. *J. Polym. Sci. Part B: Polym. Phys.* **2004**, 42, 3934-3942.

[36] Deitzel, J. M.; Kleinmeyer, J.; Harris, D.; Tan, N. C. B. *Polymer* **2001**, 42, 261-272.

[37] Ge, S. R.; Pu, Y.; Zhang, W.; Rafailovich, M.; Sokolov, J. *Phys. Rev. Lett.* **2000**, 85, 2340-2343.

[38] Ji, Y.; Li, B. Q.; Ge, S. R.; Sokolov, J. C.; Rafailovich, M. H. *Langmuir* **2006**, 22, 1321-1328.

[39] Ghosh, K.; Pan, Z.; Guan, E.; Ge, S. R.; Liu, Y. J.; Nakamura, T.; Ren, X. D.; Rafailovich, M.; Clark, R. *Biomaterials* **2007**, 28, 671-679.

[40] Varani, J.; Orr, W.; Ward, P. A. *Am. J. Pathol.* **1978**, 90, 159-171.

[41] Planus, E.; Galiacy, S.; Matthay, M.; Laurent, V.; Gavrilovic, J.; Murphy, G.; Clerici, C.; Isabey, D.; Lafuma, C.; d'Ortho, M. P. *Journal of Cell Science* **1999**, 112, 242-252.

[42] Chassagne, C.; Adamy, C.; Ratajczak, P.; Gingras, B.; Teiger, E.; Planus, E.; Oliveiro, P.; Rappaport, L.; Samuel, J. L., Meloche, S. *American Journal of Physiology-Cell Physiology* **2002**, 282, C654-664.

[43] Badami, A. S.; Kreke, M. R.; Thompson, M. S.; Riffle, J. S.; Goldstein, A. S. *Biomaterials* **2006**, 27, 596-606.

[44] den Braber, E. T.; de Ruijter, J. E.; Ginsel, L. A.; von Recum, A. F.; Jansen, J. A. *J. Biomed. Mater. Res.* **1998**, 40, 291-300.

[45] Bashur, C. A.; Dahlgren, L. A.; Goldstein, A. S. *Biomaterials* **2006**; 27, 5681-5688.

[46] Kwon, I. K.; Kidoaki, S.; Matsuda, T. *Biomaterials* **2005**, 16, 3929-3939.

[47] Xu, C. Y.; Inai, R.; Kotaki, M.; Ramakrishna, S. *Biomaterials* **2004**, 25, 877-886.

[48] Yang, F.; Murugan, R.; Wang, S.; Ramakrishna, S. *Biomaterials* **2005**, 26, 2603-2610.

[49] Ziegler, W. H.; Liddington, R. C.; Critchley, D. R. *Trends in Cell Biology* **2006**, 16, 453-460.

[50] Yamamoto, S.; Tanaka, M.; Sunami, H.; Arai, K.; Takayama, A.; Yamashita, S.; Morita, Y.; Shimomura, M. *Surface Science* **2006**, 600, 3785-3791.

[51] Wang, X. H.; Prokert, F.; Reuther, H.; Maitz, M. F.; Zhang, F. *Surface and Coating Technology* **2004**, 185, 12-17.

[52] Baker, S. C.; Atkin, N.; Gunning, P. A.; Granville, N.; Wilson, K.; Wilson, D.; Southgate, J. *Biomaterials* **2006**, 27, 3136-3146.

[53] Vinckier, A.; Semenza, G. *FEBS letters* **1998**, 430, 12-16.

[54] Ghosh, K.; Ingber, D. E. *Adv. Drug Deliv. Rev.* **2007**, 59, 1306-1318.

[55] Ghosh, K.; Ren, X. D.; Shu, X. Z.; Prestwich, G. D.; Clark, R. *Tissue Engineering* **2006**, 12, 601-613.

[56] Martin, P. *Science* **1997**, 276, 75-81.

[57] Lauffenburger, D. A.; Horwitz, A. F. *Cell* **1996**, 84, 359-369.

[58] Mitchison, T. J.; Cramer, L. P. *Cell* **1996**, 84, 371-379.

[59] Curtis, A.; Wilkinson, C. *Biomaterials* **1997**, 18, 1573-1583.

[60] Friedl, P.; Brocker, E. B. *Cellular and Molecular Life Sciences* **2000**, 57, 41-64.

[61] Friedl, P.; Zanker, K. S.; Brocker, E. B. *Microscopy Research and Technique* **1998**, 43, 369-378.

[62] Even-Ram, S.; Yamada, K. M. *Current Opinion in Cell Biology* **2005**, 17, 524-532.

[63] Grinnell, F. *Trends in Cell Biology* **2003**, 13, 264-269.

[64] Grinnell, F.; Ho, C. H.; Tamariz, E.; Lee, D. J.; Skuta, G. *Molecular Biology of the Cell*, **2003**, 14, 384-395.

[65] Grinnell, F.; Rocha, L. B.; Iucu, C.; Rhee, S.; Jiang, H. M. *Experimental Cell Research* **2006**, 312, 86-94.

[66] Rhee, S.; Grinnell, F. *Advanced Drug Delivery Reviews* **2007**, 59, 1299-1305.

[67] Schindler, M.; Nur-E-Kamal, A.; Ahmed, I.; Kamal, J.; Liu, H. Y.; Amor, N.; Ponery, A. S; Crockett, D. P.; Grafe, T. H.; Chung, H. Y.; Weik, T.; Jones, E.; Meiners, S. *Cell Biochemistry and Biophysics* **2006**, 45, 215-227.

[68] Poole, K.; Khairy, K.; Friedrichs, J.; Franz, C.; Cisneros, D. A.; Howard, J.; Mueller, D. *Journal of Molecular Biology* **2005**, 349, 380-386.

[69] Patel, S.; Kurpinski, K.; Quigley, R.; Gao, H. F.; Hsiao, B. S.; Poo, M. M.; Li, S. *Nano Letters* **2007**, 7, 2122-2128.

[70] Nain, A. S.; Phillippi, J. A.; Sitti, M.; MacKrell, J.; Campbell, P. G.; Amon, C. *Small* **2008**, 4, 1153-1159.

[71] Doyle, A. D.; Wang, F. W.; Matsumoto, K.; Yamada, K. M. *Journal of cell biology* **2009**, 184, 481-490.

[72] Ahmed, Z.; Brown, R. A. *Cell Motility and the Cytoskeleton* **1999**, 42, 331-343.

[73] Rorth, P. *Trends in Cell Biology* **2007**, 17, 575-579.

[74] Pelham, R. J.; Wang, Y. L. *Molecular Biology of the Cell* **1999**, 10, 935-945.

[75] Liu, Y.; Ji, Y.; Ghosh, K.; Clark, R.; huang, L.; Rafailovich, M. *Journal of Biomedical Materials Research Part A* **2009**, 90A, 1092-1106 .

[76] Varani, J.; Orr, W.; Ward, P. A. *American Journal of Pathology* **1978**, 90, 159-171.

[77] Pitas, R. E.; Innerarity, T. L.; Weinstein, J. N.; Mahley, R. W. *Arteriosclerosis* **1981**, 1, 177-185.

[78] Chon, J. H.; Vizena, A. D.; Rock, B. M.; Chaikof, E. L. *Analytical Biochemistry* **1997**, 252, 246-254.

[79] Ranheim, T.; Kulseth, M. A.; Berge, K. E.; Leren, T. P. *Clinical Chemistry* **2006** 52, 1469-1479.

[80] Wojciak-Stothard, B.; Denyer, M.; Mishra, M.; Brown, R. A. *In Vitro Cellular & Developmental Biology-Animal* **1997**, 33, 110-117.

[81] Schnell, E.; Klinkhammer, K.; Balzer, S.; Brook, G.; Klee, D.; Dalton, P.; Mey, J. *Biomaterials* **2007**, 28, 3012-3025.

[82] Kim, Y. T.; Haftel, V. K.; Kumar, S.; Bellamkonda, R.V. *Biomaterials* **2008**, 29, 3117-3127.

[83] Lee, J.; Jacobson, K. *Journal of Cell Science* **1997**, 110, 2833-2844.

[84] Cox, E. A.; Huttenlocher, A. *Microscopy Research and Technique* **1998**, 43, 412-419.

[85] Beningo, K. A.; Dembo, M.; Kaverina, I.; Small, J. V.; Wang, Y. L. *Journal of Cell Biology* **2001**, 153, 881-887.

[86] Dalton, B. A.; Walboomers, X. F.; Dziegielewski, M.; Evans, M. D. M.; Taylor, S.; Jansen, J. A.; Steele, J. G. *Journal of Biomedical Materials Research* **2001**, 56, 195-207.

[87] Tan, J.; Shen, H.; Saltzman, W. M. *Biophysical Journal* **2001**, 81, 2569-2579.

[88] Sun, T.; Norton, D.; McKean, R. J.; Haycock, J. W.; Ryan, A. J.; MacNeil, S. *Biotechnology and Bioengineering* **2007**, 97, 1318-1328.

[89] Battin, T. J.; Sloan, W. T.; Kjelleberg, S.; Daims, H.; Head, I. M.; Curtis, T. P.; Eberl, L. *Nature Reviews Microbiology* **2007**, 5, 76-81.

[90] Hall-Stoodley, L.; Costerton, J. W.; Stoodley P. *Nature Review Microbiology* **2004**, 2, 95-108.

[91] Costerton, J. W.; Stewart, P. S.; Greenberg, E. P. *Science* **1999**, 284, 1318-1322.

[92] Jarvis, L. M. *Chemical and Engineering News* **2008**, 86, 18.

[93] Crespo, J. G.; Velizarov, S.; Reis, M. A. *Current Opinion in Biotechnology* **2004**, 15, 463-468.

[94] Singh, R.; Paul, D.; Jain, R. K. *Trends in Microbiology* **2006**, 14, 389-397.

[95] Lovley, D. R. *Current Opinion in Biotechnology* **2008**, 19, 564-571.

[96] Nicolella, C.; van Loosdrecht, M. C. M.; Heijnen, S. J. *Trends in Microbiology* **2000**, 18, 312-320.

[97] Karube, I.; Matsunaga, T.; Tsuru, S.; Suzuki, S. *Biochimica et Biophysica Acta* **1976**, 444, 338-343.

[98] Nassif, N.; Bouvet, O.; Rager, M. N.; Roux, C.; Coradin, T.; Livage, J. *Nature Materials* **2002**, 1, 42-44.

[99] Arcuri, E. J.; Worden, R. M.; Shumate, S. E. *Biotechnology Letters* **1980**, 2, 499-504.

[100] Freeman, A.; Aharonowitz, Y. *Biotechnology and Bioengineering* **1981**, 23, 2747-2759.

[101] Townsend-Nicholson, A.; Jayasinghe, S. N. *Biomacromolecules* **2006**, 7, 3364-3369.

[102] Yarin, A. L.; Zussman, E.; Wendorff, J. H.; Greiner, A. *Journal of Materials Chemistry* **2007**, 17, 2585-2599.

[103] Abdurrahmanoglu, S.; Can, V.; Okay, O. *Journal of Applied Polymer Science* **2008**, 109, 3714-3724.

[104] Dror, Y.; Salalha, W.; Avrahami, R.; Zussman, E.; Yarin, A. L.; Dersch, R.; Greiner, A.; Wendorff, J. H. *Small* **2007**, 3, 1064-1073.

[105] Dror, Y.; Kuhn, J.; Avrahami, R.; Zussman, E. *Macromolecules* **2008**, 41, 4187-4192.

[106] Kiyonaka, S.; Sada, K.; Yoshimura, I.; Shinkai, S., Kato, N.; Hamachi, I. *Nature Materials* **2004**, 3, 58-64.

[107] Hennink, W. E.; van Nostrum, C. F. *Advanced Drug Delivery Reviews* **2002**, 54, 13-36.

[108] Kim, S. H.; Nair, S.; Moore, E. *Macromolecules* **2005**, 38, 3719-3723.

[109] Lee, S. W.; Belcher, A. M. *Nano Letter* **2004**, 4, 387-390.

[110] Salalha, W.; Kuhn, J.; Dror, Y.; Zussman, E. *Nanotechnology* **2006**, 17, 4675-4681.

[111] Gensheimer, M.; Becker, M.; Brandis-Heep, A.; Wendorff, J. H.; Thauer, R. K.; Greiner, A. *Advanced Materials* **2007**, 19, 2480-2482.

[112] Bromberg, L. E.; Ron, E. S. *Advanced Drug Delivery Reviews* **1998**, 31, 197-221.

[113] Lee, K. J.; Tribe, D. E.; Rogers, P. L. *Biotechnology Letters* **1979**, 1, 421-426.

[114] Rogers, P. L.; Lee, K. J.; Tribe, D. E. *Process Biochemistry* **1980**, 15, 7.

[115] Grote, W.; Lee, K. J.; Rogers, P. L. *Biotechnology Letters* **1980**, 2, 481-486.

[116] Sosnik, A.; Cohn, D.; San Roman, J. S.; Abraham, G. A. *Journal of Biomaterials Science-Polymer Edition* **2003**, 14, 227-239.

[117] Ji, Y.; Li, B. Q.; Ge, S. R.; Sokolov, J. C.; Rafailovich, M. H. *Langmuir* **2006**, 22, 1321-1328.

[118] Liang, C. J.; Bruell, C. J.; Marley, M. C.; Sperry, K. L. *Chemosphere* **2004**, 55, 1213-1223.

[119] Boland, E. D.; Wnek, G. E.; Simpson, D. G.; Pawlowski, K. J.; Bowlin, G. L. *Journal of Macromolecular Science-Pure and Applied Chemistry* **2001**, 38, 1231-1243.

[120] Ji, Y.; Ghosh, K.; Shu, X. Z.; Sokolov, J. C.; Prestwich, G. D.; Clark, R. A.; Rafailovich, M. *Biomaterials* **2006**, 27, 3782-3792.

[121] Zhang, Y. Z.; Venugopal, J.; Huang, Z. M.; Lim, C. T.; Ramakrishna, S. *Polymer* **2006**, 47, 2911-2917.

[122] Zhong, S. P.; Teo, W. E.; Zhu, X.; Beuerman, R.; Ramakrishna, S.; Yung, L. Y. L. *Materials Science & Engineering C-Biomimetic and Supramolecular Systems* **2007**, 27, 262-266.

[123] Vondran, J. L.; Sun, W.; Schauer, C. L. *Journal of Applied Polymer Science* **2008**, 109, 968-975.

[124] Ding, B.; Kim, H. Y.; Lee, S. C.; Shao, C. L.; Lee, D. R.; Park, S. J.; Kwag, G. B.; Choi, K. J. *Journal of Polymer Science Part B-Polymer Physics* **2002**, 40, 1261-1268.

[125] Chen, H.; Hsieh, Y. L. *Journal of Polymer Science Part a-Polymer Chemistry* **2004**, 42, 6331-6339.

[126] Li, L.; Hsieh, Y. L. *Nanotechnology* **2005**, 16, 2852-2860.

[127] Jin, X.; Hsieh, Y. L. *Macromolecular Chemistry and Physics* **2005**, 206, 1745-1751.

[128] Li, L.; Hsieh, Y. L. *Polymer* **2005**, 46, 5133-5139.

[129] Zeng, J.; Hou, H. Q.; Wendorff, J. H.; Greiner, A. *Macromolecular Rapid Communications* **2005**, 26, 1557-1562.

[130] Choi, S. S.; Hong, J. P.; Seo, Y. S.; Chung, S. M.; Nah, C. *Journal of Applied Polymer Science* **2006**, 101, 2333-2337.

[131] Ignatova, M.; Starbova, K.; Markova, N.; Manolova, N.; Rashkov, I. *Carbohydrate Research* **2006**, 341, 2098-2107.

[132] Singh, D.; Kuckling, D.; Choudhary, V.; Adler, H. J.; Koul, V. *Polymers for Advanced Technologies* **2006**, 17, 186-192.

[133] Leach, J. B.; Bivens, K. A.; Patrick, C. W.; Schmidt, C. E. *Biotechnology and Bioengineering* **2003**, 82, 578-589.

[134] Kizilel, S.; Perez-Luna, V. H.; Teymour, F. *Macromolecular Theory and Simulations* **2006**, 15, 686-700.

[135] Zhu, W.; Ding, J. D. *Journal of Applied Polymer Science* **2006**, 99, 2375-2383.

[136] Hennink, W. E.; Talsma, H.; Borchert, J. C. H.; DeSmedt, S. C.; Demeester, J. *Journal of Controlled Release* **1996**, 39, 47-55.

[137] Franssen, O.; Vos, O. P.; Hennink, W. E. *Journal of Controlled Release* **1997**, 44, 237-245.

[138] Kayaman, N.; Kazan, D.; Erarslan, A.; Okay, O.; Baysal, B. M. *Journal of Applied Polymer Science* **1998**, 67, 805-814.

[139] Can, V.; Abdurrahmanoglu, S.; Okay, O. *Polymer* **2007**, 48, 5016-5023.

[140] Feng, X. D.; Guo, X. Q.; Qiu, K. Y. *Makromolekulare Chemie-Macromolecular Chemistry and Physics* **1988**, 189, 77-83.

[141] Pomortseva, N. V.; Krasilnikova, T. N. *Khimiko-Farmatsevticheskii Zhurnal* **1983**, 17, 721-725.

[142] Cohn, D.; Sosnik, A.; Garty, S. *Biomacromolecules* **2005**, 6, 1168-1175.

[143] Henderson, A. M. *IEEE Electrical Inulation Magazine* **1993**, 9, 30-38.

[144] Kalachandra, S.; Lin, D. M.; Offenbacher, S. *Journal of Materials Science-Materials in Medicine* **2002**, 13, 53-58.

[145] Lin, D. M.; Kalachandra, S.; Valiyaparambi, J.; Offenbacher, S. *Dental Materials* **2003**, 19, 589-596.

[146] Tallury, P.; Alimohammadi, N.; Kalachandra, S. *Dental Materials* **2007**, 23, 404-409.

[147] Zanetti, M.; Camino, G.; Thomann, R.; Mullhaupt, R. *Polymer* **2001**, 42, 4501-4507.

[148] Pramanik, M.; Srivastava, S. K.; Samantaray, B. K.; Bhowmick, A. K. *Journal of Materials Science Letters* **2001**, 20, 1377-1380.

[149] Alexandre, M.; Beyer, G.; Henrist, C.; Cloots, R.; Rulmont, A.; Jerome, R.; Dubois, P. *Macromolecular Rapid Communications* **2001**, 22, 643-646.

[150] Li, X. C.; Ha, C. S. *Journal of Applied Polymer Science* **2003**, 87, 1901-1909.

[151] Zhang, W.; Chen, D. Z.; Zhao, Q. B.; Fang, Y. *Polymer* **2003**, 44, 7953-7961.

[152] Peeterbroeck, S.; Alexandre, M.; Jerome, R.; Dubois, P. *Polymer Degradation and Stability* **2005**, 90, 288-294.

[153] Arinstein, A.; Burman, M.; Gendelman, O.; Zussman, E. *Nature Nanotechnology* **2007**, 2, 59-62.

[154] Deitzel, J. M.; Kleinmeyer, J.; Harris, D.; Tan, N. C. B. *Polymer* **2001**, 42, 261-272.

[155] Koombhongse, S.; Liu, W. X.; Reneker, D. H. *Journal of Polymer Science Part B: Polymer Physics* **2001**, 39, 2598-2606.

[156] Shin, Y. M.; Hohman, M. M.; Brenner, M. P.; Rutledge, G. C. *Polymer* **2001**, 42, 9955-9967.

[157] Kenawy, E. R.; Bowlin, G. L.; Mansfield, K.; Layman, J.; Simpson, D. G.; Sanders, E. H.; Wnek, G. E. *Journal of Controlled Release* **2002**, 81, 57-64.

[158] Sanders, E. H.; Kloefkorn, R.; Bowlin, G. L.; Simpson, D. G.; Wnek, G. E. *Macromolecules* **2003**, 36, 3803-3805.

[159] Lewkowitz-Shpuntoff, H. M.; Wen, M. C.; Singh, A.; Brenner, N.; Gambino, R.; Pernodet, N.; Isseroff, R.; Rafailovich, M.; Sokolov, J. *Biomaterials* **2009**, 30, 8-18.

[160] Ge, S.; Pu, Y.; Zhang, W.; Rafailovich, M.; Sokolov, J.; Buenviaje, C.; Buckmaster, R.; Overney, R. M. *Physical Review Letters* **2000**, 85, 2340-2343.

[161] Gopakumar, T. G.; Lee, J. A.; Kontopoulou, M.; Parent, J. S. *Polymer* **2002**, 43, 5483-5491.

[162] Chaudhary, D. S.; Prasad, R.; Gupta, R. K.; Bhattacharya, S. N. *Thermochimica Acta* **2005**, 433, 187-195.

[163] Ji, Y.; Li, B. Q.; Ge, S. R.; Sokolov, J. C.; Rafailovich, M. H. *Langmuir* **2006**, 22, 1321-1328.

[164] Wang, Y.; Ge, S.; Rafailovich, M.; Sokolov, J.; Zou, Y.; Ade, H.; Luning, J.; Lustiger, A.; Maron, G. *Macromolecules* **2004**, 37, 3319-3327.

[165] Xie, X. L.; Mai Y. W.; Zhou X. P. *Materials Science& Engineering R-Reports*

2005,49, 89-112.